High-Order Homogenization
Method in Diffusion Theory for Reactor
Core Simulation and Design Calculation

Farzad Rahnema,
Principal Investigator

Georgia Institute of Technology
Nuclear Engineering and Health Physics Programs
George W. Woodruff School of Mechanical Engineering
Atlanta, GA 30332-0405 USA

High-Order Homogenization Method in Diffusion Theory for Reactor Core Simulation and Design Calculation

Phase 2 Final Report

by

Farzad Rahnema, Principal Investigator

Georgia Institute of Technology
Nuclear Engineering and Health Physics Programs
George W. Woodruff School of Mechanical Engineering
Atlanta, GA 30332-0405, USA

Prepared for
Department of Energy under NEER Grant
Contract Number DE-FG0-001D13960; B&R Code AF40

Period of Performance: JULY 1, 2001 – JUNE 30, 2002

Table of Contents

List of Figures

List of Tables

SUMMARY

The high-order homogenization method for improving the accuracy of nodal diffusion calculations for a reactive system was implemented into a two-group model. The method corrects the generalized equivalence theory (GET) homogenized parameters for the effect of the core environment by expanding the homogenized cross sections in terms of the current-to-flux ratio at the node interface. The cross sections are updated (corrected) within the nodal calculation by using precomputed data for each unique assembly type, together with the current-to-flux ratio at the node interface. Two codes in 1-D two-group were developed to perform the precomputation and the nodal calculations: a fine-mesh lattice code and a nodal diffusion code with a bilinear intra-nodal flux shape.

It was shown that the perturbation expansion series for the flux, eigenvalue and the homogenized cross section converge in the multigroup case. This is new in that it has not been shown before in the literature. The benchmark configurations consisting of two types of BWR assemblies in two-group slab geometry were analyzed for various magnitudes of the perturbation in the boundary condition. The perturbation method achieves an excellent accuracy: the flux RMS error is less than 0.5% in both groups and the reference homogenized cross sections are almost exactly reproduced.

The testing of the nodal code was done for five benchmark configurations typical of a BWR, from mildly to highly heterogeneous. Three of these configurations were developed in this phase. It was concluded that for testing the applicability and the accuracy of the homogenization method these new benchmark problems that are more realistic are needed. Each assembly in the new benchmark configuration is of the GE-9 bundle design. The two-group cross sections for the assemblies used in the new benchmark problems were generated from the infinite-medium solution of a fine-mesh two-dimensional model of the 8×8 GE-9 fuel assembly with eight burnable gadolinium absorber rods, by using the generalized geometry collision-probability code HELIOS. A technical paper containing the detailed description of the benchmark problems as well as both diffusion and transport theory results will be published during the phase 3 period.

In summary, it was shown that the homogenization method provides excellent results in the two-group theory. For all of the analyzed configurations, the node-integrated flux is within 1.16% of the assembly reference (fine-mesh) flux in all nodes for each group. There is a significant improvement from the zeroth order case (standard GET), in which the node-averaged flux has a large error (e.g., up to 8% in group 1 and up to 14% in group 2 for configuration 2). It was also shown that the reconstructed fine-mesh flux (or equivalently the power distribution) in the core approximates the reference value very well. The reference flux distribution is almost reproduced by the third order perturbation approximation.

The works performed in phase 1 period were published in two technical papers; one in Annals of Nuclear Energy and one as an ANS Transaction summary (1. Scott M. McKinley and F. Rahnema, "High-Order Cross Section Homogenization Method," *Ann. Nucl. Energy*, **29**, 875-899(2002); 2. F. Rahnema and Scott M. McKinley, "Coarse-Mesh Nodal Methods Corrected by Boundary Condition Perturbation Theory", *Trans. Am. Nucl. Soc.,* **84**, 93 (June 2001)). The phase 2 works will be summarized in two technical papers to be submitted in summer 2002; one on the benchmark problems and one on the multigroup numerical developments. Additionally, an ANS summary has been accepted for presentation at the ANS summer 2002 meeting (Germina Ilas and F. Rahnema, "Applicaton of High-Order Boundary Condition Perturbation Theory to Two-Group Diffusion Problems", *Trans. Am. Nucl. Soc.,* accepted (June 2002)).

Chapter I

Introduction

1.1. Background

A high-order cross section homogenization method [9] based on the boundary condition perturbation theory has been recently developed to improve the accuracy of nodal diffusion methods within the context of the generalized equivalence theory (GET) [1]. The method corrects the homogenized parameters and discontinuity factors for the effect of the core environment. The homogenized parameters, which are expanded in terms of the node surface current-to-flux ratios, could be corrected to an arbitrary order of accuracy for the effect of the core heterogeneity. The reconstructed fine-mesh flux and power distributions are a natural byproduct of this method. For completeness, the basic formalism of the high-order cross-section homogenization method is described below. More details can be found in references 8 and 9.

The perturbation method developed by McKinley and Rahnema [8] estimates the change in the solution of a reactive system due to a change in the boundary condition to an arbitrary order, in the diffusion approximation. The formalism is derived starting from the steady-state diffusion eigenvalue equation for an initial (unperturbed) state of the system:

$$H\overline{\varphi}_0(\vec{x}, E) = \lambda_0 F\overline{\varphi}_0(\vec{x}, E), \qquad \vec{x} \in V \tag{1-1}$$

where H is the diffusion operator (accounting for leakage, absorption and in-scattering), F is the production operator, λ_0 is the eigenvalue, and $\overline{\varphi}_0$ is the initial flux. The unperturbed flux is normalized such that its integral over the phase-space ($\vec{x}, E$) is unity. The boundary condition associated to Eq. (1-1) is:

1

$$a_0(\vec{x}, E)\hat{n} \cdot \nabla \overline{\varphi}_0(\vec{x}, E) + b_0(\vec{x}, E)\overline{\varphi}_0(\vec{x}, E) = 0, \qquad \vec{x} \in \partial V \tag{1-2}$$

with $\vec{x}$ and E the spatial and energy variables, and $\hat{n}$ the outward unit normal. The parameter b_0 becomes the current-to-flux ratio at the boundary when a_0 is taken as the diffusion coefficient. For a perturbation in the boundary condition of the form:

$$a_0(\vec{x}, E)\hat{n} \cdot \nabla \overline{\varphi}_0(\vec{x}, E) + (b_0(\vec{x}, E) + \varepsilon b_1(\vec{x}, E))\overline{\varphi}_0(\vec{x}, E) = 0, \qquad \vec{x} \in \partial V \tag{1-3}$$

the eigenvalue equation (1-1) is written as:

$$H\overline{\varphi}(\vec{x}, E) = \lambda\ F\overline{\varphi}(\vec{x}, E), \qquad \vec{x} \in V \tag{1-4}$$

where λ is the perturbed eigenvalue and $\overline{\varphi}$ is the perturbed flux normalized to unity. It is assumed that the perturbed flux and eigenvalue can be expanded in terms of a smallness parameter ε as:

$$\lambda = \lambda_0 + \varepsilon\lambda_1 + \varepsilon^2\lambda_2 \cdots + \varepsilon^n\lambda_n + o(\varepsilon^{n+1}) \tag{1-5}$$

$$\overline{\varphi} = \overline{\varphi}_0 + \varepsilon\overline{\varphi}_1 + \varepsilon^2\overline{\varphi}_2 \cdots \varepsilon^n\overline{\varphi}_n + o(\varepsilon^{n+1}) \tag{1-6}$$

These expansions are used in equation (1-4) and the expansion coefficients are obtained, by equating the terms with the same power of ε, as functionals of the flux. The high-order corrections for eigenvalue and flux in Eqs. (1-5) and (1-6) are calculated based on the solutions for the forward and adjoint flux of the initial (unperturbed) state, and a Green's function defined by the equation:

$$\left(H^* - \lambda_0 F^*\right)\Psi(\vec{x}, \vec{x}_0, E) = \delta(\vec{x} - \vec{x}_0)\delta(E - E_0) - \overline{\varphi}_0(\vec{x}_0, E_0), \qquad \vec{x}, \vec{x}_0 \in V \tag{1-7}$$

$$a_0(\vec{x}, E)\hat{n} \cdot \nabla\Psi(\vec{x}, \vec{x}_0, E) + b_0(\vec{x}, E)\Psi(\vec{x}, \vec{x}_0, E) = 0, \qquad \vec{x}, \vec{x}_0 \in \partial V$$

2

Green's function $\Psi(\vec{x}, \vec{x}_0, E)$ is required to satisfy the following uniqueness condition:

$$\left\langle \Psi(\vec{x}, \vec{x}_0, E) F\varphi_0(\vec{x}, E) \right\rangle = 0, \qquad \vec{x}, \vec{x}_0 \in V \tag{1-8}$$

In (1-7), H^* and F^* are the adjoints of the operators H and F from Eq. (1-1). The brackets in Eq. (1-8) stand for scalar product over the phase-space ($\vec{x}, E$).

The expressions of the high-order corrections for flux and eigenvalue are:

$$\lambda_1 = \frac{\left\langle \overline{\varphi}_0^* \varepsilon \overline{\varphi}_0 \right\rangle_s}{\left\langle \overline{\varphi}_0^* F \overline{\varphi}_0 \right\rangle} \tag{1-9-a}$$

$$\lambda_2 = \frac{\left\langle \overline{\varphi}_0^* \varepsilon \overline{\varphi}_1 \right\rangle_s - \lambda_1 \left\langle \overline{\varphi}_0^* F \overline{\varphi}_1 \right\rangle}{\left\langle \overline{\varphi}_0^* F \overline{\varphi}_0 \right\rangle} \tag{1-9-b}$$

$$\lambda_n = \frac{\left\langle \overline{\varphi}_0^* \varepsilon \overline{\varphi}_{n-1} \right\rangle_s - \lambda_1 \left\langle \overline{\varphi}_0^* F \overline{\varphi}_{n-1} \right\rangle - \lambda_2 \left\langle \overline{\varphi}_0^* F \overline{\varphi}_{n-2} \right\rangle \cdots - \lambda_{n-1} \left\langle \overline{\varphi}_0^* F \overline{\varphi}_1 \right\rangle}{\left\langle \overline{\varphi}_0^* F \overline{\varphi}_0 \right\rangle}, \qquad n > 2 \tag{1-9-c}$$

$$\overline{\varphi}_1(\vec{x}_0) = -\left\langle \Psi(\vec{x}, \vec{x}_0) \varepsilon \overline{\varphi}_0(\vec{x}) \right\rangle_s \tag{1-10-a}$$

$$\overline{\varphi}_2(\vec{x}_0) = \lambda_1 \left\langle \Psi(\vec{x}, \vec{x}_0) F \overline{\varphi}_1(\vec{x}) \right\rangle - \left\langle \Psi(\vec{x}, \vec{x}_0) \varepsilon \overline{\varphi}_1(\vec{x}) \right\rangle_s \tag{1-10-b}$$

$$\overline{\varphi}_n(\vec{x}_0) = \lambda_1 \left\langle \Psi(\vec{x}, \vec{x}_0) F \overline{\varphi}_{n-1}(\vec{x}) \right\rangle + \lambda_2 \left\langle \Psi(\vec{x}, \vec{x}_0) F \overline{\varphi}_{n-2}(\vec{x}) \right\rangle \cdots + \lambda_{n-1} \left\langle \Psi(\vec{x}, \vec{x}_0) F \overline{\varphi}_1(\vec{x}) \right\rangle$$
$$- \left\langle \Psi(\vec{x}, \vec{x}_0) \varepsilon \overline{\varphi}_{n-1}(\vec{x}) \right\rangle_s \tag{1-10-c}$$

In reference 8 it is shown that ratios of arbitrary functionals of the flux solution can be expanded in terms of the smallness parameter, similar to the expansions for the eigenvalue and flux (Eqs. (1-5) and (1-6), respectively). It is shown that this result can be

used to homogenize phase-space parameters such as cross section, which can be defined as:

$$\sigma_g = \sigma_{0,g} + \varepsilon\sigma_{1,g} + \varepsilon^2\sigma_{2,g} \cdots + \varepsilon^n\sigma_{n,g} + o\left(\varepsilon^{n+1}\right) \qquad (1\text{-}11)$$

with the expansion coefficients given by:

$$\sigma_{0,g} = \frac{\left\langle \sigma(\vec{x},E)\overline{\varphi}_0(\vec{x},E)\right\rangle_{\vec{x},g}}{\left\langle \overline{\varphi}_0(\vec{x},E)\right\rangle_{\vec{x},g}} \qquad (1\text{-}12\text{-a})$$

$$\sigma_{1,g} = \frac{\left\langle \sigma(\vec{x},E)\overline{\varphi}_1(\vec{x},E)\right\rangle_{\vec{x},g} - \sigma_{0,g}\left\langle \overline{\varphi}_1(\vec{x},E)\right\rangle_{\vec{x},g}}{\left\langle \overline{\varphi}_0(\vec{x},E)\right\rangle_{\vec{x},g}} \qquad (1\text{-}12\text{-b})$$

$$\sigma_{2,g} = \frac{\left\langle \sigma(\vec{x},E)\overline{\varphi}_2(\vec{x},E)\right\rangle_{\vec{x},g} - \sigma_{0,g}\left\langle \overline{\varphi}_2(\vec{x},E)\right\rangle_{\vec{x},g} - \sigma_{1,g}\left\langle \overline{\varphi}_1(\vec{x},E)\right\rangle_{\vec{x},g}}{\left\langle \overline{\varphi}_0(\vec{x},E)\right\rangle_{\vec{x},g}} \qquad (1\text{-}12\text{-c})$$

$$\sigma_{n,g} = \frac{\left\langle \sigma(\vec{x},E)\overline{\varphi}_n(\vec{x},E)\right\rangle_{\vec{x},g} - \sigma_{0,g}\left\langle \overline{\varphi}_n(\vec{x},E)\right\rangle_{\vec{x},g} - \cdots\sigma_{n-1,g}\left\langle \overline{\varphi}_1(\vec{x},E)\right\rangle_{\vec{x},g}}{\left\langle \overline{\varphi}_0(\vec{x},E)\right\rangle_{\vec{x},g}} \qquad (1\text{-}12\text{-d})$$

The subscript $\vec{x}$ outside the brackets in the above equations stands for integration over all space, and the subscript g means integration over energy from E_{g-1} to E_g.

Based on this high-order boundary condition perturbation theory, the high-order cross section homogenization method developed by Rahnema and McKinley [9] expands the nodal parameters in terms of the node surface current-to flux ratio. The procedure is as follows:

- The nodal calculation is performed by using the infinite medium homogenized parameters (zero current boundary condition), and the solution is used to calculate the current-to-flux ratio (γ) at each node interface

4

- This ratio is used as a perturbation of the boundary condition in the high-order boundary condition formalism that evaluates the high-order correction for the homogenized parameters in each node

- The nodal calculation is redone with the corrected homogenized parameters, and new γ's are determined

- The iteration continues until convergence is achieved

1.2. Summary of Phase 1 Work

The equations for correcting the homogenization parameters (see Eqs. (1-12)) for the core environmental (assembly surface leakage) effect were developed using the high-order boundary condition perturbation method [8]. A coarse-mesh code with a bilinear flux shape was written for one-speed, 1-D geometry to test the correctness and the accuracy of the high-order homogenization method. The method was benchmarked using two one-dimensional configurations (see Figure 3-1) typical of mildly to highly heterogeneous BWR cores. Each core is made up of two unique alternating assemblies lined up in a one-dimensional array with a zero-current external boundary condition.

The first test was to take each assembly from configuration 2 (the more restrictive example) and use the boundary condition perturbation theory to determine the homogenization parameters for the exact albedos given from the reference case. A fine-mesh solution of the full core case was taken as the exact (reference) solution for the flux and eigenvalue. By using the exact flux distribution, the right and left face albedos for each assembly were determined. The results [9] for assembly 1 in core 2 are shown here in Tables 1-1 and 1-2 as an example. Table 1-1 shows the values of the corrected eigenvalue and homogenized cross sections as well as the flux RMS. Table 1-2 shows the values of the heterogeneous discontinuity factors χ (see Eq. 2-40) for the left and right boundary of the assembly. As seen from the tables, the accuracy improves with increasing the order of the expansion terms. The fourth order expansion seems sufficient to significantly reduce the errors in the homogenized cross sections. The error in the heterogeneous discontinuity factor χ becomes insignificantly small when seventh order

5

perturbation theory is used. The fourth order corrected flux models very well the reference flux distribution in comparison to the unperturbed (zeroth order) flux: 0.2% flux RMS in the first case versus 20.2% flux RMS in the latter case.

Table 1-1. Analysis of Assembly 1[*] in Core 2 for One-Group 1-D

	Unperturbed (Infinite-Medium)	1st Order	2nd Order	3rd Order	Exact
λ	0.7248 (19)	1.0006 (-12)	0.8414 (6.2)	0.9230 (-2.9)	0.8969
Flux %RMS	20.2	9.7	3.9	1.2[a]	-
D	1.2616 (-0.22)	1.2570 (0.14)	1.2594 (-0.05)	1.2583 (0.03)	1.2588
σ_a	0.02249 (1.5)	0.02303 (-0.84)	0.02275 (0.42)	0.02288 (-0.16)	0.02284
$\nu\sigma_f$	0.03103 (1.8)	0.03192 (-0.99)	0.03145 (0.49)	0.03166 (-0.18)	0.03161

[*] Type 1 fuel assembly with left and right albedo of 0 and 0.13321 respectively and 1200 meshes

[a] 4th order = 0.2

Table 1-2. Heterogeneous Discontinuity Factor χ for Assembly 1[*] for One-Group 1-D

Perturbation Order	Boundary		%Error	
	Left	Right	Left	Right
Exact	1.1575	0.6297	-	-
0th (∞-medium)	0.9907	0.9907	-14.4	57.3
1st	1.2312	0.4475	6.4	-28.9
2nd	1.1311	0.7090	-2.3	12.6
3rd	1.1629	0.6023	0.5	-4.4
4th	1.1584	0.6357	0.1	0.9
5th	1.1552	0.6309	-0.2	0.2
6th	1.1586	0.6278	0.1	-0.3
7th	1.1567	0.6311	-0.1	0.2

[*] Type 1 fuel assembly in core 2, with left and right albedo of 0 and 0.13321 respectively and 1200 meshes

Table 1-3. Assembly Integrated Flux for Configuration 2

Order of Perturbation	Assembly Position	Reference	Nodal	Error[a] (%)	Reconstructed	Error (%)
0	1	2.370	1.082	-54	2.872	21
	2	0.658	0.913	39	0.250	-62
	3	0.357	1.057	196	0.310	-13
	4	0.173	0.898	418	0.105	-39
1	1	2.370	2.827	19	2.823	19
	2	0.658	0.453	-31	0.454	-31
	3	0.357	0.188	-47	0.188	-47
	4	0.173	0.068	-61	0.068	-61
2	1	2.370	2.281	-3.8	2.281	-3.7
	2	0.658	0.722	9.8	0.720	9.5
	3	0.357	0.381	6.8	0.374	5.0
	4	0.173	0.200	15	0.196	13
3	1	2.370	2.465	4.0	2.487	4.9
	2	0.658	0.641	-2.6	0.650	-1.2
	3	0.357	0.304	-15	0.311	-13
	4	0.173	0.144	-17	0.146	-16
4	1	2.370	2.382	0.5	2.386	0.6
	2	0.658	0.666	1.2	0.671	1.9
	3	0.357	0.360	0.9	0.366	2.7
	4	0.173	0.175	0.9	0.177	2.2

[a]Defined as 100*(calculated-reference)/reference

It was found that the new homogenization method is very accurate as compared to the standard homogenization technique based on the generalized equivalence theory. The results of the nodal calculations [9] for configuration 2 with the homogenized parameters corrected up to the 4th orders are shown here in Table 1-3. Only the first four assemblies were shown due to symmetry. It can be seen that there is a large improvement compared to the zeroth order (standard GET) both for the assembly nodal flux as well as for the assembly reconstructed flux. The large difference (of up to 418%) between the assembly nodal flux and the assembly reference flux is reduced to less than 1.2% at the fourth order. The results are similar for the assembly reconstructed flux, where the large zeroth order difference (up to 62%) is reduced to less than 2.7% at the fourth order.

A paper describing the method and the one-group 1-D benchmark results was published in the May 2002 issue of *Annals of Nuclear Energy*. Also, a summary of the work was presented at the ANS meeting in June 2001.

1.2. Description of Phase 2 Work

The accomplishment of the second phase work is the implementation of the high-order cross section homogenization method in the two-group methodology and, in particular, showing that the perturbation expansion series converge for the multigroup case. When going from one-group to two-group, the forms of the equations to be solved and of the expressions to be evaluated become more complex, due to the coupling between groups. There are also complications that arise regarding the numerical methods used to solve these equations. The most difficult task is the computation of the Green's function. The methods used to obtain the two-group solutions of the specific equations, in particular the one for the Green's function, are presented in chapter II.

Here it is shown that the perturbation expansion series for the flux, eigenvalue and homogenized cross-section converge for the two-group problems, by using as a benchmark configuration an assembly typical of a BWR in slab geometry. A two-group nodal diffusion code with a bilinear intra-nodal flux shape is developed for the implementation of the high-order homogenization method in the context of the

generalized equivalence theory. The code is tested by using as a benchmark a configuration typical of a BWR in slab geometry. The two types of configurations discussed in the previous year report for one-group are also analyzed here in a two-group approach. One of these configurations (core 1) is very simple, with not much variation of the flux across the core. The other one (core 2) is more complex, with large flux gradients at the nodal interface and large variations in the flux distribution. In order to assess the applicability of the new homogenization method on more realistic cores, with many different types of assemblies, three new benchmarks typical of a BWR in slab geometry were developed. These newly developed benchmark configurations, as well as the other two configuration mentioned before are described in chapter III. The results obtained are presented in chapter IV, and concluding remarks are presented in chapter V.

Chapter II

Method

In the multigroup case, the three equations (for the forward flux, the adjoint flux, and Green's function of the unperturbed state of the system) whose solutions are required to evaluate the expansion coefficients for flux, eigenvalue, and homogenized cross-section have a more complicated form than for the one-group case, due to energy group coupling. The numerical solution method for the multigroup Green's function becomes substantially more complicated in the two-group case and as a result it consumed a large portion of the effort spent in phase 2 of the contract work.

2.1. Equations in the multigroup case

The equation for the forward flux, Eq. (1-1) of the unperturbed state becomes a system of G coupled equations, where G is the total number of energy groups.

$$H_g \overline{\varphi}_{0,g}(\vec{x}) = \lambda_0 F_g \overline{\varphi}_{0,g}(\vec{x}), \quad \vec{x} \in V, \quad g = 1...,G \tag{2-1}$$

with the boundary condition expressed as:

$$a_{0,g}(\vec{x}) \hat{n} \cdot \nabla \overline{\varphi}_{0,g}(\vec{x}) + b_{0,g}(\vec{x}) \overline{\varphi}_{0,g}(\vec{x}) = 0, \quad \vec{x} \in \partial V \quad g = 1...,G \tag{2-2}$$

The index g stands for the energy group, and the operators H_g and F_g are defined by:

$$H_g = -\nabla D_g(\vec{x}) \nabla + \sigma_g(\vec{x}) - \sum_{g'=1}^{2} \sigma_{sg'g}(\vec{x}) \tag{2-3}$$

$$F_g = \chi_g(\vec{x})\sum_{g'=1}^{2} \nu\sigma_{fg'}(\vec{x}) \tag{2-4}$$

where D_g, σ_g, and χ_g are the diffusion coefficient, the total cross section, and the fission spectrum in group g; $\sigma_{sg'g}$ is the scattering cross section from group g' to group g, and $\nu\sigma_{fg}$ is the product of the number of neutrons per fission and the fission cross section in group g.

The adjoint flux for the unperturbed state is given by:

$$H_g^* \overline{\varphi}_{0,g}^*(\vec{x}) = \lambda_0^* F_g^* \overline{\varphi}_{0,g}^*(\vec{x}), \qquad \vec{x} \in V \qquad g = 1...,G \tag{2-5}$$

with the corresponding boundary condition expressed as:

$$a_{0,g}(\vec{x})\hat{n}\cdot\nabla\overline{\varphi}_{0,g}^*(\vec{x}) + b_{0,g}(\vec{x})\overline{\varphi}_{0,g}^*(\vec{x}) = 0, \qquad \vec{x} \in \partial V \qquad g = 1...,G \tag{2-6}$$

The adjoint operators H_g^* and F_g^* are defined by:

$$H_g^* = -\nabla D_g(\vec{x})\nabla + \sigma_g(\vec{x}) - \sum_{g'=1}^{2}\sigma_{sgg'}(\vec{x}) \tag{2-7}$$

$$F_g^* = \nu\sigma_{fg}(\vec{x})\sum_{g'=1}^{2}\chi_{g'}(\vec{x}) \tag{2-8}$$

In a two-group case, Green's function equation (1-7) becomes:

$$\left(H_g^* - \lambda_0 F_g^*\right)\Psi_{gh}(\vec{x},\vec{x}_0) = \delta(\vec{x}-\vec{x}_0)\delta_{gh} - \overline{\varphi}_{0,h}(\vec{x}_0), \qquad \vec{x} \in V \qquad g,h = 1,2 \tag{2-9}$$

with the boundary condition

11

$$a_{0,g}(\vec{x})\hat{n}\cdot\nabla\Psi_{gh}(\vec{x},\vec{x}_0)+b_{0,g}(\vec{x})\Psi_{gh}(\vec{x},\vec{x}_0)=0, \quad \vec{x}\in\partial V \quad g,h=1,2 \tag{2-10}$$

The symbol δ_{gh} in (2-9) is the Kronecker function defined by:

$$\delta_{gh}=\begin{cases}1, h=g\\0, h\neq g\end{cases} \tag{2-11}$$

The expressions for the expansion coefficients in the eigenvalue and flux expansions that have the energy as a continuous variable (see 1-9 and 1-10) are particularized to two-group as shown below:

$$\lambda_1 = \frac{\sum_{g=1}^{2}\left\langle\overline{\varphi}_{0,g}^*\gamma_g\overline{\varphi}_{0,g}\right\rangle_s}{\sum_{g=1}^{2}\left\langle\overline{\varphi}_{0,g}^*F_g\overline{\varphi}_{0,g}\right\rangle} \tag{2-12-a}$$

$$\lambda_2 = \frac{\sum_{g=1}^{2}\left(\left\langle\overline{\varphi}_{0,g}^*\gamma_g\overline{\varphi}_{1,g}\right\rangle_s-\lambda_1\left\langle\overline{\varphi}_{0,g}^*F_g\overline{\varphi}_{1,g}\right\rangle\right)}{\sum_{g=1}^{2}\left\langle\overline{\varphi}_{0,g}^*F_g\overline{\varphi}_{0,g}\right\rangle} \tag{2-12-b}$$

$$\lambda_n = \frac{\sum_{g=1}^{2}\left(\left\langle\overline{\varphi}_{0,g}^*\gamma_g\overline{\varphi}_{n-1,g}\right\rangle_s-\lambda_1\left\langle\overline{\varphi}_{0,g}^*F_g\overline{\varphi}_{n-1,g}\right\rangle-\lambda_2\left\langle\overline{\varphi}_{0,g}^*F_g\overline{\varphi}_{n-2,g}\right\rangle\cdots-\lambda_{n-1}\left\langle\overline{\varphi}_{0,g}^*F_g\overline{\varphi}_{1,g}\right\rangle\right)}{\sum_{g=1}^{2}\left\langle\overline{\varphi}_{0,g}^*F_g\overline{\varphi}_{0,g}\right\rangle}, \quad n>2$$

$$\tag{2-12-c}$$

$$\overline{\varphi}_{1,h}(\vec{x}_0)=-\sum_{g=1}^{2}\left\langle\Psi_{gh}(\vec{x},\vec{x}_0)\gamma_g\overline{\varphi}_{0,h}(\vec{x})\right\rangle_s, \quad h=1,2 \tag{2-13-a}$$

$$\overline{\varphi}_{2,h}(\vec{x}_0)=\lambda_1\sum_{g=1}^{2}\left\langle\Psi_{gh}(\vec{x},\vec{x}_0)F_g\overline{\varphi}_{1,h}(\vec{x})\right\rangle-\sum_{g=1}^{2}\left\langle\Psi_{gh}(\vec{x},\vec{x}_0)\gamma_g\overline{\varphi}_{1,h}(\vec{x})\right\rangle_s, \quad h=1,2 \tag{2-13-b}$$

$$\overline{\varphi}_{n,h}(\vec{x}_0) = \lambda_1 \sum_{g=1}^{2} \left\langle \Psi_{gh}(\vec{x},\vec{x}_0) F_g \overline{\varphi}_{n-1,h}(\vec{x}) \right\rangle + \lambda_2 \sum_{g=1}^{2} \left\langle \Psi_{gh}(\vec{x},\vec{x}_0) F_g \overline{\varphi}_{n-2,h}(\vec{x}) \right\rangle \cdots$$

$$+ \lambda_{n-1} \sum_{g=1}^{2} \left\langle \Psi_{gh}(\vec{x},\vec{x}_0) F_g \overline{\varphi}_{1,h}(\vec{x}) \right\rangle - \sum_{g=1}^{2} \left\langle \Psi_{gh}(\vec{x},\vec{x}_0) \gamma_g \overline{\varphi}_{n-1,h}(\vec{x}) \right\rangle_s, \qquad h=1,2$$

(2-13-c)

The brackets in the above expressions stand for scalar products over the volume, the subscript s outside the brackets indicating that the integration is over the boundary region of the volume. The parameter γ_g is the perturbation of the boundary current-to-flux ratio for group g, $\overline{\varphi}_{0,g}^{*}(x)$ is the adjoint flux in group g for the initial state, and $\overline{\varphi}_{k,g}(x)$ is the kth-order flux in group g.

2.2. Method for the Green's Function in Two-Group

The main difficulty when extending the method to two-group is in obtaining the solution for the Green's function, which in two-group 1-D becomes a vectorial function (there are four components of $\Psi_{gh}(\vec{x},\vec{x}_0)$), whereas in one-group 1-D is a scalar function. For fixed values of the spatial variables $\vec{x}$ and $\vec{x}_0$, there are four components (equal to the square of the number of groups) of the function $\Psi_{gh}(\vec{x},\vec{x}_0)$ which need to be determined, and therefore four coupled equations, compared to only one equation in the one-group case. By writing Eq. (2-9) for values of the indices g and h over all range (g,h=1,2), one gets the following four, two by two coupled, equations:

$$\left[-\nabla D_1(\vec{x})\nabla + \sigma_{r1}(\vec{x}) - \lambda_0 \nu\sigma_{f1}(\vec{x})\chi_1(\vec{x})\right]\Psi_{11}(\vec{x},\vec{x}_0) -$$
$$\left[\sigma_{s12}(\vec{x}) + \lambda_0 \nu\sigma_{f1}(\vec{x})\chi_2(\vec{x})\right]\Psi_{21}(\vec{x},\vec{x}_0) = \delta(\vec{x}-\vec{x}_0) - \overline{\varphi}_{0,1}(\vec{x}_0)$$

(2-14-a)

$$\left[-\nabla D_2(\vec{x})\nabla + \sigma_{r2}(\vec{x}) - \lambda_0 \nu\sigma_{f2}(\vec{x})\chi_2(\vec{x})\right]\Psi_{21}(\vec{x},\vec{x}_0) -$$
$$\left[\sigma_{s21}(\vec{x}) + \lambda_0 \nu\sigma_{f2}(\vec{x})\chi_1(\vec{x})\right]\Psi_{11}(\vec{x},\vec{x}_0) = -\overline{\varphi}_{0,1}(\vec{x}_0)$$

(2-14-b)

13

$$\left[-\nabla D_1(\vec{x})\nabla + \sigma_{r1}(\vec{x}) - \lambda_0 \nu \sigma_{f1}(\vec{x})\chi_1(\vec{x})\right]\Psi_{12}(\vec{x},\vec{x}_0) -$$
$$\left[\sigma_{s12}(\vec{x}) + \lambda_0 \nu \sigma_{f1}(\vec{x})\chi_2(\vec{x})\right]\Psi_{22}(\vec{x},\vec{x}_0) = -\overline{\varphi}_{0,2}(\vec{x}_0) \qquad \text{(2-14-c)}$$

$$\left[-\nabla D_2(\vec{x})\nabla + \sigma_{r2}(\vec{x}) - \lambda_0 \nu \sigma_{f2}(\vec{x})\chi_2(\vec{x})\right]\Psi_{22}(\vec{x},\vec{x}_0) -$$
$$\left[\sigma_{s21}(\vec{x}) + \lambda_0 \nu \sigma_{f2}(\vec{x})\chi_1(\vec{x})\right]\Psi_{12}(\vec{x},\vec{x}_0) = \delta(\vec{x}-\vec{x}_0) - \overline{\varphi}_{0,2}(\vec{x}_0) \qquad \text{(2-14-d)}$$

where σ_r is the removal cross section. Equations (2-14-a) and (2-14-b) constitute a linear system for the unknowns $\Psi_{11}(\vec{x},\vec{x}_0)$ and $\Psi_{21}(\vec{x},\vec{x}_0)$, whereas Eqs. (2-14-c) and (2-14-d) constitute a similar system for $\Psi_{12}(\vec{x},\vec{x}_0)$ and $\Psi_{22}(\vec{x},\vec{x}_0)$. By discretizing the equations in slab geometry (integrating over the x variable), one gets two systems of matrix equations with unknowns X_1, X_2, Y_1, and Y_2, as shown below:

$$\begin{cases} A_1 X_1(j) - B_1 X_2(j) = D(j) - c_1(j)C \\ A_2 X_2(j) - B_2 X_1(j) = -c_1(j)C \end{cases} \qquad \text{(2-15)}$$

$$\begin{cases} A_1 Y_1(j) - B_1 Y_2(j) = D(j) - c_2(j)C \\ A_2 Y_2(j) - B_2 Y_1(j) = c_2(j)C \end{cases} \qquad \text{(2-16)}$$

The system (2-15) corresponds to Eqs. (2-14-a) and (2-14-b), whereas the system (2-16) corresponds to Eqs. (2-14-c) and (2-14-d). A_1 and A_2 are NxN tridiagonal matrices, B_1 and B_2 are NxN diagonal matrices, D, C, X_1, X_2, Y_1, and Y_2 are N- component vectors, and $c_1(j)$ and $c_2(j)$ are constants, with j as a mesh index for x_0 (j=1,..,N).

$$X_1^T(j) = \left[\Psi_{11}(1,j), \Psi_{11}(2,j)\cdots\Psi_{11}(i,j)\cdots\Psi_{11}(N,j)\right] \qquad \text{(2-17)}$$

$$X_2^T(j) = \left[\Psi_{21}(1,j), \Psi_{21}(2,j)\cdots\Psi_{21}(i,j)\cdots\Psi_{21}(N,j)\right] \qquad \text{(2-18)}$$

$$Y_1^T(j) = \left[\Psi_{12}(1,j), \Psi_{12}(2,j)\cdots\Psi_{12}(i,j)\cdots\Psi_{12}(N,j)\right] \qquad \text{(2-19)}$$

14

$$Y_2^T(j) = [\Psi_{22}(1,j), \Psi_{22}(2,j) \cdots \Psi_{22}(i,j) \cdots \Psi_{22}(N,j)] \tag{2-20}$$

$$D^T(j) = [\delta_{1j}, \delta_{2j} \cdots \delta_{ij} \cdots \delta_{Nj}] \tag{2-21}$$

$$C^T(j) = [\Delta x_1, \Delta x_2 \cdots \Delta x_i \cdots \Delta x_N] \tag{2-22}$$

The components of the vector C are the mesh lengths, and those of the vector D are Kronecker functions (see Eqs. (2-11)). The diagonal coefficients for matrices B_1 and B_2 are given by:

$$\begin{aligned}
b_{ii}^1 &= \lambda_0 v \sigma_{f1}^i \chi_2^i + \sigma_{s12}^i &,i = 1, \cdots N \\
b_{ii}^2 &= \lambda_0 v \sigma_{f2}^i \chi_1^i + \sigma_{s21}^i &,i = 1, \cdots N
\end{aligned} \tag{2-23}$$

The nonzero coefficients of matrices A_1 and A_2 are defined by:

$$a_{i-1,i}^1 = -\frac{2(D_1^i / \Delta_i)(D_1^{i-1} / \Delta_{i-1})}{(D_1^i / \Delta_i) + (D_1^{i-1} / \Delta_{i-1})} \qquad ,i = 2 \cdots N$$

$$a_{i,i+1}^1 = -\frac{2(D_1^i / \Delta_i)(D_1^{i+1} / \Delta_{i+1})}{(D_1^i / \Delta_i) + (D_1^{i+1} / \Delta_{i+1})} \qquad ,i = 1 \cdots N-1 \tag{2-24}$$

$$a_{i,i}^1 = a_{i-1,i}^1 + a_{i,i+1}^1 + \Delta_i(\sigma_{r1}^i - \lambda_0 v \sigma_{f1}^i \chi_1) \qquad ,i = 2 \cdots N-1$$

$$a_{i-1,i}^2 = -\frac{2(D_2^i / \Delta_i)(D_2^{i-1} / \Delta_{i-1})}{(D_2^i / \Delta_i) + (D_2^{i-1} / \Delta_{i-1})} \qquad ,i = 2 \cdots N$$

$$a_{i,i+1}^2 = -\frac{2(D_2^i / \Delta_i)(D_2^{i+1} / \Delta_{i+1})}{(D_2^i / \Delta_i) + (D_2^{i+1} / \Delta_{i+1})} \qquad ,i = 1 \cdots N-1 \tag{2-25}$$

$$a_{i,i}^2 = a_{i-1,i}^2 + a_{i,i+1}^2 + \Delta_i(\sigma_{r2}^i - \lambda_0 v \sigma_{f2}^i \chi_2) \qquad ,i = 2 \cdots N-1$$

The constants c_1 and c_2 are given by:

15

$$c_1(j) = \overline{\varphi}_{0,1}(j) \tag{2-26}$$

$$c_2(j) = \overline{\varphi}_{0,2}(j)$$

The coefficients for which the expressions are not shown in the above equations are those that correspond to boundary meshes (i=1,N). These expressions cannot be written for a general case unless the boundary condition is specified. The discretization of Eqs. (2-14) is presented in more detail in Appendix B.

The systems (2-15) and (2-16) need to be solved for each j=1,2,...N. In order to do this, they are written in a compact form, as shown below:

$$\begin{bmatrix} A_1 & -B_1 \\ -B_2 & A_2 \end{bmatrix} \begin{pmatrix} X_1(j) \\ X_2(j) \end{pmatrix} = \begin{pmatrix} D(j) \\ 0 \end{pmatrix} - c_1(j) \begin{pmatrix} C \\ C \end{pmatrix} \tag{2-27}$$

$$\begin{bmatrix} A_1 & -B_1 \\ -B_2 & A_2 \end{bmatrix} \begin{pmatrix} Y_1(j) \\ Y_2(j) \end{pmatrix} = \begin{pmatrix} D(j) \\ 0 \end{pmatrix} - c_2(j) \begin{pmatrix} C \\ C \end{pmatrix} \tag{2-28}$$

or equivalently as:

$$AX(j) = V_1(j) - c_1(j)V_2 \tag{2-29}$$

$$AY(j) = V_1(j) - c_2(j)V_2 \tag{2-30}$$

with A a 2N x 2N band matrix, X,Y,V$_1$ and V$_2$ 2N-component vectors. In solving Eqs. (2-29) and (2-30) one must account for the uniqueness condition (1-8), which in two-group is expressed by the two following equations:

$$\left\langle \Psi_{11}(\vec{x},\vec{x}_0)\chi_1(\vec{x})\sum_{g'=1}^{2} v\sigma_{fg'}(\vec{x})\wp_{0,g'}(\vec{x}) + \Psi_{21}(\vec{x},\vec{x}_0)\chi_2(\vec{x})\sum_{g'=1}^{2} v\sigma_{fg'}(\vec{x})\wp_{0,g'}(\vec{x}) \right\rangle_{\vec{x}} = 0 \tag{2-31}$$

$$\left\langle \Psi_{12}(\vec{x},\vec{x}_0)\chi_1(\vec{x})\sum_{g'=1}^{2} v\sigma_{fg'}(\vec{x})\wp_{0,g'}(\vec{x}) + \Psi_{22}(\vec{x},\vec{x}_0)\chi_2(\vec{x})\sum_{g'=1}^{2} v\sigma_{fg'}(\vec{x})\wp_{0,g'}(\vec{x}) \right\rangle_{\vec{x}} = 0 \tag{2-32}$$

By discretizing the Eqs. (2-31) and (2-32) in slab geometry one gets:

$$\sum_{i=1}^{N}\left(\Psi_{11}(i,j)\chi_1(i)\sum_{g'=1}^{2}v\sigma_{fg'}(i)\wp_{0,g'}(i)+\Psi_{21}(i,j)\chi_2(i)\sum_{g'=1}^{2}v\sigma_{fg'}(i)\wp_{0,g'}(i)\right)\Delta_i=0, j=1,...N \qquad (2\text{-}33)$$

$$\sum_{i=1}^{N}\left(\Psi_{21}(i,j)\chi_1(i)\sum_{g'=1}^{2}v\sigma_{fg'}(i)\wp_{0,g'}(i)+\Psi_{22}(i,j)\chi_2(i)\sum_{g'=1}^{2}v\sigma_{fg'}(i)\wp_{0,g'}(i)\right)\Delta_i=0, j=1,...N \qquad (2\text{-}34)$$

where i and j are mesh indices for x and x_0, Δ_i is the length of mesh i, and N is the total number of meshes. Equation (2-33) and the system (2-29) have as unknowns the components of the adjoint Green's function $\Psi_{gh}(i,j)$ for which g=1,2 and h=1. Equation (2-34) and the system (2-30) have as unknowns the components of the adjoint Green's function $\Psi_{gh}(i,j)$ for which g=1,2 and h=2.

Two approaches have been followed to solve for Green's function. Let's consider the system (2-29) with the corresponding Eq. (2-34) expressing the uniqueness condition. The first approach was to consider Eq. (2-34) as an additional equation of the system (2-29). The resulting system is overdetermined:

$$A_3 x_3 = b_3 \qquad (2\text{-}35)$$

where A_3 is a (2N+1) by 2N matrix, and x_3 and b_3 are (2N+1)-length vectors. The system (2-35) can be solved by using a least square method, which consists of minimizing the square Euclidian norm:

$$\|r\|_2^2 = r^T r, \qquad r = b_3 - A_3 x_3 \qquad (2\text{-}36)$$

with 2N+1 equations and 2N unknowns. The procedures used to minimize (2-36) involve the reduction of the matrix A_3 to various canonical forms via orthogonal

transformations [4]. Here a QR factorization of A_3 method was used, which consists of seeking a (2N+1) by (2N+1) orthogonal matrix Q such that

$$A_3 = Q \begin{bmatrix} R \\ 0 \end{bmatrix}$$
(2-37)

where R is a 2N by 2N upper triangular matrix. The factorization was performed by using a routine from the IMSL MATH/LIBRARY [6]. The solution obtained for Eq. (2-35) was not accurate enough for the purpose of the present work. The residuals (components of $r = b_3 - A_3 x_3$) were not very small compared to the components of the right term b_3.

The second approach used to solve for Green's function is the following: for each x_0 (j from 1 to N), the system (2-29) is solved by replacing the jth line with Eq. (2-33) for the same j (expressing the uniqueness condition for that particular x_0). The system (2-30) is solved in a similar manner, but in conjunction with Eq. (2-34). Since the resulting systems of equations are ill-conditioned, standard methods cannot be used for solving them. The condition number is of the order 10^3 – 10^4. Here a singular value decomposition method (SVD) [4] is used for obtaining the solution. The SVD method for solving a linear system ($Ax = b$), with A a 2N by 2N real nonsingular matrix, is based on the decomposition:

$$A = U \Sigma V^T$$
(2-38)

where U and V are orthogonal matrices, and Σ is a diagonal matrix. The elements on the diagonal of Σ are called singular values of the matrix A:

$$\sigma_1 \geq \sigma_2 \geq ... \geq \sigma_{2N} \geq 0$$
(2-39)

They can be used to get an estimation of the condition number, as a ratio of the largest to the smallest of the σ components.

18

2.3. High-Order Cross Section Homogenization for Two-Group Nodal Diffusion

A two-group nodal diffusion code with a bilinear intra-nodal flux shape and discontinuous flux across the node interface was developed in conjunction with the high-order cross section homogenization method discussed in chapter I. It allows the correction of the cross sections and discontinuity factors up to an arbitrary order based on precomputed data (forward and adjoint flux distributions, and the Green's function, as discussed in sections 2.1 and 2.2) for each unique assembly type, by using the current-to-flux ratios at the node interface determined from the nodal calculation. An infinite medium (zero net current boundary condition) is taken as the initial (unperturbed state) of the assembly. The nodal discretization of the nodal equations is presented in Appendix B.

The initial (zeroth order) nodal parameters are the standard GET homogenized cross sections and discontinuity factors, determined from infinite medium single node calculations. The standard discontinuity factor on each side of a nodal interface is defined as the ratio of the heterogeneous flux (that is continuous at the interface) to the homogeneous flux on each side of the interface. It is calculated as [1]:

$$f^k = \frac{\overline{\varphi}_{im}^k}{\overline{\varphi}_{im}} \tag{2-40}$$

where χ^k is the standard discontinuity factor for face k of the node, $\overline{\varphi}_{im}^k$ and $\overline{\varphi}_{im}$ are the surface-averaged flux on face k and the node-averaged flux from infinite medium calculations, respectively.

For the nodal calculations, the discontinuity factor in group g on face k of the node can be written in terms of its infinite medium approximation χ_g^k as [5]:

$$f_g^k = \chi_g^k \frac{\overline{\phi}_g}{\overline{\phi}_g^k} \tag{2-41}$$

where $\overline{\phi}_g$ and $\overline{\phi}_g^k$ represent the node-averaged flux in group g and the average flux on face k in group g from the nodal calculations, respectively. The so-called heterogeneous discontinuity factor χ_g^k is calculated as:

$$\chi_g^k = \frac{\int_{S_k} d^2 x \overline{\varphi}_g(\vec{x})}{\int_V d^3 x \overline{\varphi}_g(\vec{x})} = \frac{\left\langle \overline{\varphi}_{0,g} \right\rangle_s + \gamma_g \left\langle \overline{\varphi}_{1,g} \right\rangle_s + \gamma_g^2 \left\langle \overline{\varphi}_{2,g} \right\rangle_s + \cdots + \gamma_g^n \left\langle \overline{\varphi}_{n,g} \right\rangle_s + o\left(\varepsilon^{n+1}\right)}{\left\langle \overline{\varphi}_{0,g} \right\rangle + \gamma_g \left\langle \overline{\varphi}_{1,g} \right\rangle + \gamma_g^2 \left\langle \overline{\varphi}_{2,g} \right\rangle + \cdots + \gamma_g^2 \left\langle \overline{\varphi}_{n,g} \right\rangle + o\left(\varepsilon^{n+1}\right)} \qquad (2\text{-}42)$$

where γ_g is the current-to-flux ratio in group g for interface k of the node. γ_g is calculated as [5]:

$$\gamma_g^k = \frac{\overline{J}_g^k}{f_g^k \overline{\varphi}_g^k} \qquad (2\text{-}43)$$

where $\overline{J}_g^k$ is the average current for group g on face k, determined from the nodal calculation.

The convergence criteria used for the iterative nodal cross sections updating, as described in chapter I, are given below:

- The change in the average flux in each node (mesh) and for each group in two consecutive cross sections updating iterations is less than 1%

$$\frac{\left| \varphi_{g,i}^{avg}(k) - \varphi_{g,i}^{avg}(k-1) \right|}{\varphi_{g,i}^{avg}(k)} \leq 1\% \qquad i = 1,..N, \qquad g = 1,2 \qquad (2\text{-}44)$$

- The change in the eigenvalue in two consecutive cross section updating iterations is less than 10^{-3}

$$\left| \lambda(k) - \lambda(k-1) \right| \leq 10^{-3} \qquad (2\text{-}45)$$

20

The reconstructed fine-mesh flux is a byproduct of the method. For each node, it is obtained by modulating the detailed flux distribution, which is obtained at each updating of the cross section through the high-order perturbation formalism (see Eqs. (2-13)), with the nodal flux:

$$\varphi_{r,g}^{n}(i) = \varphi_{p,g}^{n}(i) \frac{\int_{node} dx \sum_{g'=1}^{2} \varphi_{g'}^{node}(x)}{\sum_{i=1}^{N} \sum_{g'=1}^{2} \Delta_i \varphi_{p,g'}^{n}(i)}$$

(2-46)

where $\varphi_{r,g}^{n}(i)$ is the reconstructed flux for group g and mesh i in node n, and $\varphi_{p,g}^{n}(i)$ is the fine-mesh flux for group g and mesh i in node n obtained using the perturbation formalism. The denominator of the ratio in Eq. (2-46) represents the integral of the nodal flux over the node n, and the numerator is the integral of the fine-mesh flux, obtained from the perturbation formalism, over the assembly corresponding to node n.

The reconstructed flux at different orders of the correction is compared to the zeroth order (standard GET) reconstructed flux. The reconstruction of the zeroth order flux here is performed by modulating the infinite-medium assembly flux with the nodal flux obtained by using the standard (uncorrected) cross sections in the nodal calculations. The form of the zeroth order reconstructed flux in a node is expressed as:

$$\varphi_{r}^{i}(x) = c_i \varphi_{n}^{i}(x) \varphi_{im}^{i}(x), \qquad i = 1, N$$

(2-47)

where N is the number of nodes, i is the node index, φ_r is the zeroth order reconstructed flux, φ_n is the nodal flux, φ_{im} is the infinite-medium flux, and c_i is a constant. The constant c_i is determined by requiring the zeroth order reconstructed flux to be continuous at the node interface:

$$c_i \varphi_{n}^{i}(x_{i,i+1}) \varphi_{im}^{i}(x_{i,i+1}) = c_{i+1} \varphi_{n}^{i+1}(x_{i,i+1}) \varphi_{im}^{i+1}(x_{i,i+1}), \qquad i = 1, N-1$$

(2-48)

where $x_{i,i+1}$ is the coordinate corresponding to the interface between nodes i and i+1. If c_1 is fixed ($c_1 = c$), all the others constants c_i (i=2,…N-1) are determined from (2-48). c is determined by equating the core-integrated nodal flux with the core-integrated zeroth order reconstructed flux.

Chapter III

Description of the Benchmark Configurations

  The benchmark configurations (called 1 and 2) discussed in the last year report for the one group case are also analyzed here for two-group [5]. Each configuration is a core typical of a BWR in slab geometry, with a total length of 106.68 cm, consisting of seven assemblies of three types. The layouts for these two configurations and for the component assemblies are shown in Figure 3-1.

  The three types of assemblies have the same geometry, but a different fuel composition. Each assembly consists of four fuel regions each 3.231cm thick surrounded by water. The water gap is 1.158 cm thick, and the assembly length is 15.24 cm. The two-group cross sections [5] for each material are shown in Table 3-1, and the infinite medium multiplication constant for each assembly type is given in Table 3-2. Assembly 3, which is the least reactive one ($k_\infty = 0.6677$), has two fuel regions that contain gadolinium.

  The fine-mesh flux distributions of the two configurations, for a zero net current boundary condition, are presented in Figure 3-2 and Figure 3-3 (for configuration 1 and configuration 2, respectively) to highlight the flux gradient across the core and the shape of the flux that needs to be approximated. Configuration 1 is a simple core with small gradients of the flux at the assemblies' interface. Core 2 is a more restrictive configuration, with large flux gradients at the interfaces and a significant change of the flux across the core.

Assembly 1   Assembly 2   Assembly 3

Water   Fuel I   Fuel II   Fuel III
(with Gd)

Configuration 1

1	2	1	2	1	2	1

Configuration 2

1	3	1	3	1	3	1

Figure 3-1. Assemblies and Configurations Layouts for Cores 1 and 2

Table 3-1. Material Properties for Assemblies in Configurations 1 and 2

Cross Section[*]	Water	Fuel I	Fuel II	Fuel III (with Gd)
D_1	1.7639	1.4730	1.4804	1.5432
σ_{a1}	0.0003	0.0096	0.0101	0.0135
$\gamma\sigma_{f1}$	0	0.0067	0.0078	0.0056
σ_{s12}	0.0380	0.0161	0.0156	0.0136
D_2	0.2278	0.3294	0.3362	0.3143
σ_{a2}	0.0097	0.0764	0.0901	0.4873
$\gamma\sigma_{f2}$	0	0.1241	0.1542	0.0187
σ_{s21}	0	0	0	0

* The diffusion coefficients are in cm, and the cross sections in cm^{-1}

Table 3-2. K_∞[*] for Assemblies in Configurations 1 and 2

Assembly Type	K_∞
1	1.33267
2	1.30188
3	0.66768

[*]Calculated with 6 meshes/each material region
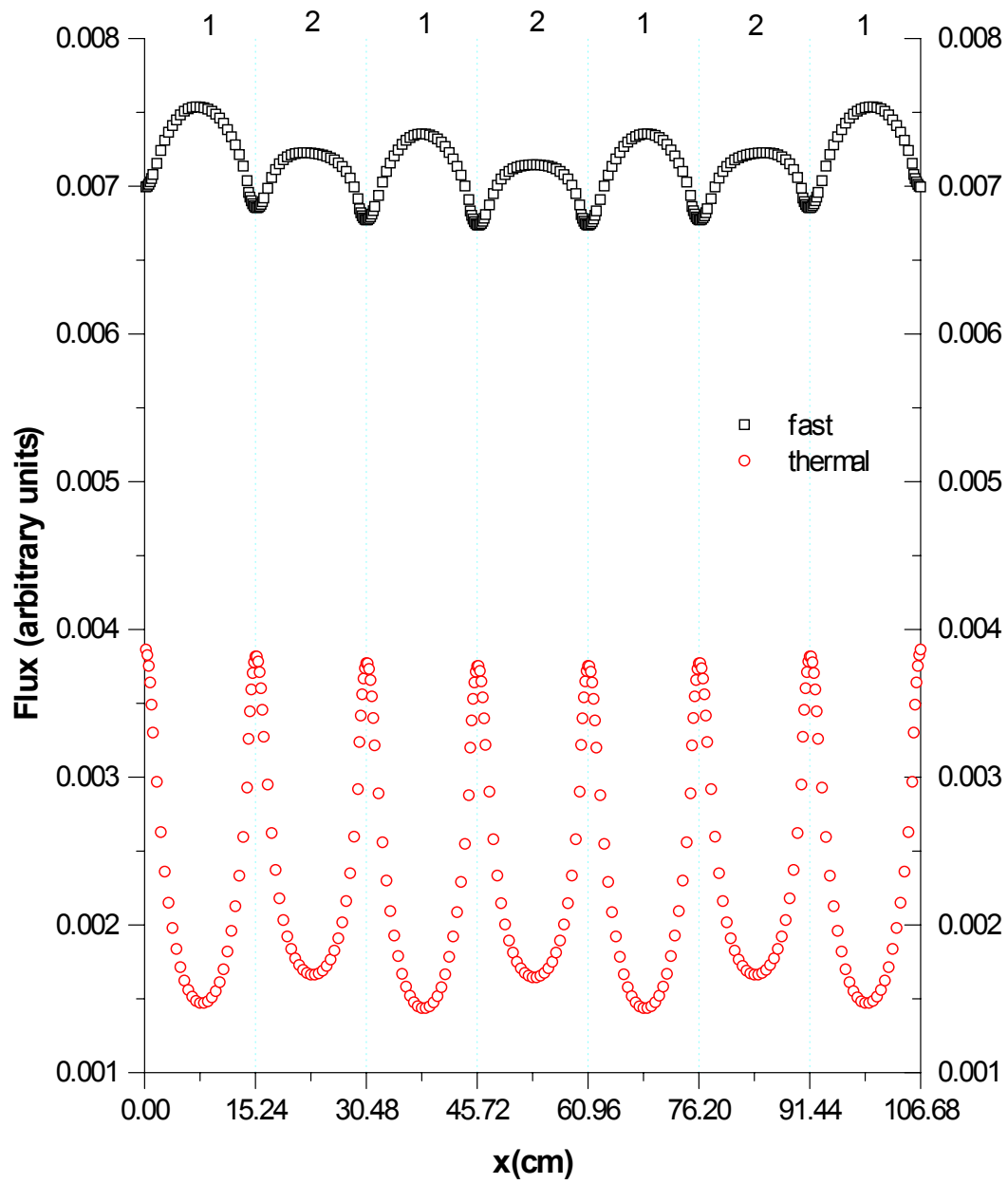
Figure 3-2. Flux Distribution in Configuration 1
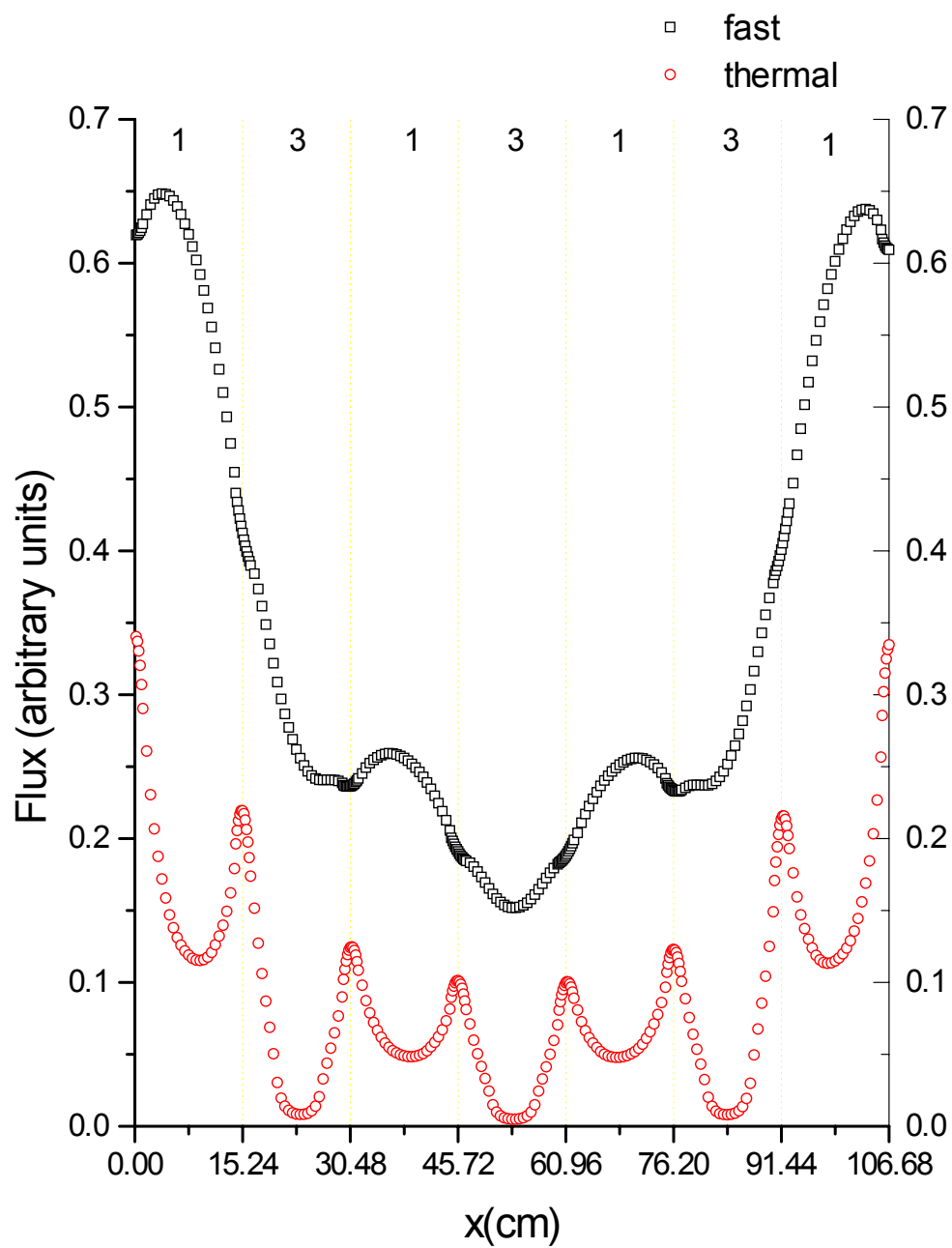
Figure 3-3. Flux Distribution in Configuration 2

3.1. Development of New Benchmark Configurations

Three new more realistic benchmark configurations typical of a BWR in slab geometry were developed. Each core configuration has 16 fuel assemblies, and a total length of 243.84 cm. There are six different assembly types. Each assembly, of the GE-9 bundle design, consists of eight fuel regions with water gaps at each side. The assembly and core layouts are shown in Figures 3-4 and 3-5, respectively. The assembly types are labeled from 1 to 6, and the core types are labeled A, B, and C. The cross sections for each assembly type are given in Tables 3-3 to 3-8, and the infinite-medium multiplication constant is given in Table 3-9. The fine-mesh flux distributions from in core configurations A, B and C are shown in Figures 3-6, 3-7 and 3-8, respectively. Because of the symmetry, only the distribution for the left half of the configuration is shown. It can be observed that core C is the most heterogeneous one, with large variations of the flux across the core.

The two-group cross sections for the one-dimensional assemblies in Figure 3-4 were generated from the infinite-medium solution of a fine-mesh two-dimensional model of the 8×8 GE-9 fuel assembly [3] with eight burnable gadolinium absorber rods. The infinite-medium solution was computed using the collision-probability code HELIOS [2] version 1.6 [7] with a 45-group neutron cross section library. A plot of the HELIOS computational mesh is shown in Figure 3-9. Note that only half of the assembly was modeled due to the diagonal symmetry of the system. The fuel was depleted to a burnup of 50,000 MWd/tU through 52 time steps. Six burnup levels were selected for use in the 1-D slab problem: fresh fuel with equilibrium Xenon and Samarium concentrations; 12,000; 27,500; 30,000; 35,000; and 50,000 MWd/tU. The fine-group cross sections for these assembly states were then homogenized in ten regions and collapsed to the classic two-group structure (0.625 eV fast/thermal boundary). The regions correspond to vertical slices of the assembly. With the assembly oriented with the wide gap on the left (as in Figure 3-9), the first region includes everything to the left of the first column of pin cells. The next eight regions correspond to the eight columns of pin cells. Note that the central two columns do not have straight vertical boundaries in the HELIOS model. Consequently, the average width of each of these two regions was used in the 1-D slab

model. The tenth and final region corresponds to everything to right of the last column of pin cells. Finally, assemblies were arranged in the 1-D core so that the wide and narrow gaps of neighboring assemblies were adjacent, as in actual BWR cores.

0.88 1.63 1.63 1.61 1.64 1.64 1.61 1.63 1.63 1.36 (cm)
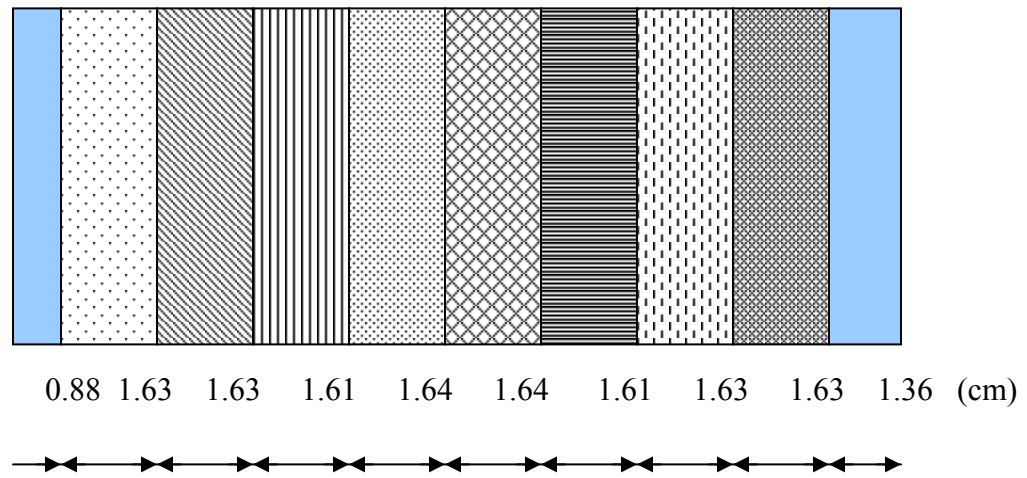
Geometry for assembly type 1, 3 and 5

1.36 1.63 1.63 1.61 1.64 1.64 1.61 1.63 1.63 0.88 (cm)
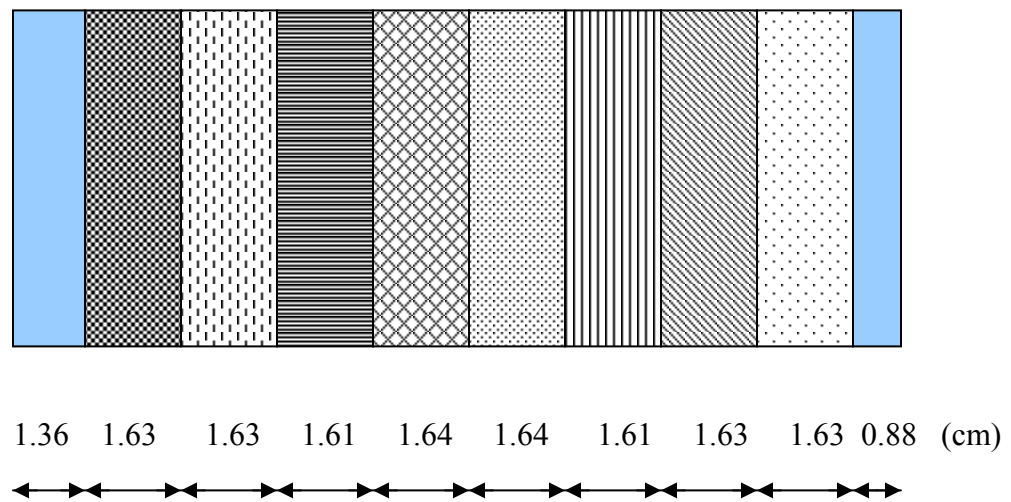
Geometry for assembly type 2, 4 and 6

Figure 3-4. Layouts for Assemblies in Configurations A, B, and C

Core A

| 5 | 6 | 1 | 2 | 1 | 2 | 1 | 2 | 2 | 1 | 2 | 1 | 2 | 1 | 6 | 5 |

Core B

| 5 | 6 | 3 | 4 | 3 | 4 | 3 | 2 | 2 | 3 | 4 | 3 | 4 | 3 | 6 | 5 |

Core C

| 5 | 6 | 5 | 6 | 5 | 6 | 5 | 4 | 4 | 5 | 6 | 5 | 6 | 5 | 6 | 5 |
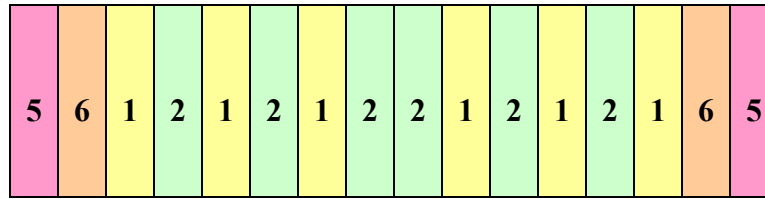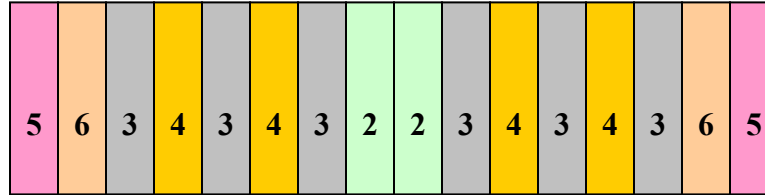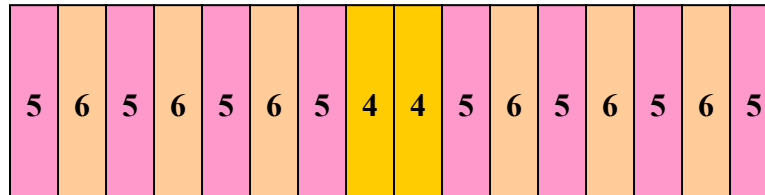
Figure 3-5. Layouts for Configurations A, B and C

Table 3-3. K_∞^* for Assemblies in Cores A, B and C

Assembly	Burnup (MWd/tU)	K_∞^*
1	30,000	0.99787
2	27,500	1.02104
3	35,000	0.95309
4	0 + Xe/Sm	1.05206
5	50,000	0.83781
6	12,000	1.16238

[*] Fine-mesh calculations with 6 meshes per material region

31

Table 3-4. Cross Section[*] Data for Assembly 1

Material #[**]	D_1	$\nu\sigma_{f1}$	σ_{a1}	σ_{12}	D_2	$\nu\sigma_{f2}$	σ_{a2}
1	.123606E+01	.000000E+00	.502126E-03	.294667E-01	.275967E+00	.000000E+00	.824310E-02
2	.132711E+01	.357186E-02	.912890E-02	.134793E-01	.418860E+00	.673313E-01	.575315E-01
3	.134518E+01	.418529E-02	.871413E-02	.122726E-01	.414601E+00	.845764E-01	.659061E-01
4	.134056E+01	.450485E-02	.904711E-02	.116912E-01	.414376E+00	.959859E-01	.721948E-01
5	.133044E+01	.339868E-02	.686882E-02	.149655E-01	.363271E+00	.683769E-01	.534524E-01
6	.133026E+01	.348024E-02	.677523E-02	.152843E-01	.363114E+00	.701716E-01	.539338E-01
7	.133903E+01	.477865E-02	.911480E-02	.111977E-01	.413490E+00	.104183E+00	.760959E-01
8	.134394E+01	.467405E-02	.894015E-02	.113039E-01	.412236E+00	.994829E-01	.733380E-01
9	.132979E+01	.436352E-02	.927441E-02	.120595E-01	.413988E+00	.908413E-01	.692121E-01
10	.128959E+01	.000000E+00	.594152E-03	.230344E-01	.315804E+00	.000000E+00	.739186E-02

[*] Diffusion coefficients are in cm and cross sections are in cm^{-1} ; no upscattering.

[**] From left to right of the assembly

Table 3-5. Cross Section[*] Data for Assembly 2

Material #[**]	D_1	$\nu\sigma_{f1}$	σ_{a1}	σ_{12}	D_2	$\nu\sigma_{f2}$	σ_{a2}
1	.129066E+01	.000000E+00	.593008E-03	.229587E-01	.316129E+00	.000000E+00	.738181E-02
2	.133083E+01	.448700E-02	.921768E-02	.120335E-01	.413772E+00	.937679E-01	.700652E-01
3	.134491E+01	.480552E-02	.889558E-02	.112858E-01	.412123E+00	.102478E+00	.741872E-01
4	.133999E+01	.491485E-02	.906971E-02	.111782E-01	.413368E+00	.107359E+00	.770120E-01
5	.133130E+01	.358057E-02	.674298E-02	.152424E-01	.363115E+00	.723637E-01	.545548E-01
6	.133157E+01	.350162E-02	.683371E-02	.149244E-01	.363234E+00	.706760E-01	.541394E-01
7	.134169E+01	.464404E-02	.900012E-02	.116669E-01	.414063E+00	.994246E-01	.732746E-01
8	.134633E+01	.431137E-02	.866630E-02	.122512E-01	.414260E+00	.877441E-01	.669033E-01
9	.132837E+01	.365292E-02	.904741E-02	.134504E-01	.418656E+00	.695389E-01	.581468E-01
10	.123725E+01	.000000E+00	.501013E-03	.293568E-01	.276130E+00	.000000E+00	.823674E-02

[*] Diffusion coefficients are in cm and cross sections are in cm^{-1} ; no upscattering.

[**] From left to right of the assembly

Table 3-6. Cross Section[*] Data for Assembly 3

Material #[**]	D_1	$\nu\sigma_{f1}$	σ_{a1}	σ_{12}	D_2	$\nu\sigma_{f2}$	σ_{a2}
1	.123391E+01	.000000E+00	.504241E-03	.296708E-01	.275660E+00	.000000E+00	.825518E-02
2	.132492E+01	.343357E-02	.929063E-02	.135307E-01	.419244E+00	.634313E-01	.564453E-01
3	.134308E+01	.395448E-02	.880972E-02	.123112E-01	.415354E+00	.785511E-01	.639516E-01
4	.133846E+01	.424347E-02	.914015E-02	.117385E-01	.415143E+00	.892341E-01	.699840E-01
5	.132830E+01	.320441E-02	.693837E-02	.150491E-01	.363420E+00	.638225E-01	.520241E-01
6	.132827E+01	.328983E-02	.683864E-02	.153671E-01	.363197E+00	.657869E-01	.526174E-01
7	.133723E+01	.451778E-02	.920275E-02	.112397E-01	.413921E+00	.977767E-01	.741315E-01
8	.134214E+01	.442286E-02	.902725E-02	.113430E-01	.412638E+00	.934750E-01	.715297E-01
9	.132786E+01	.413453E-02	.938686E-02	.121126E-01	.414507E+00	.851878E-01	.674935E-01
10	.128756E+01	.000000E+00	.596386E-03	.231822E-01	.315162E+00	.000000E+00	.741177E-02

[*] Diffusion coefficients are in cm and cross sections are in cm^{-1} ; no upscattering.

[**] From left to right of the assembly

Table 3-7. Cross Section[*] Data for Assembly 4

Material #[**]	D_1	$\nu\sigma_{f1}$	σ_{a1}	σ_{12}	D_2	$\nu\sigma_{f2}$	σ_{a2}
1	.128965E+01	.000000E+00	.589990E-03	.232679E-01	.319333E+00	.000000E+00	.728288E-02
2	.133315E+01	.624849E-02	.841321E-02	.125178E-01	.419496E+00	.108700E+00	.660741E-01
3	.133930E+01	.633130E-02	.887330E-02	.119167E-01	.400060E+00	.972496E-01	.963494E-01
4	.133295E+01	.646164E-02	.905883E-02	.117938E-01	.399344E+00	.991401E-01	.101514E+00
5	.132750E+01	.487744E-02	.631206E-02	.157675E-01	.371781E+00	.805383E-01	.504019E-01
6	.132481E+01	.470393E-02	.696659E-02	.154214E-01	.353952E+00	.653003E-01	.818175E-01
7	.133896E+01	.631830E-02	.893711E-02	.123118E-01	.397431E+00	.978842E-01	.101481E+00
8	.135244E+01	.614404E-02	.795681E-02	.127463E-01	.419030E+00	.107776E+00	.657387E-01
9	.133924E+01	.517189E-02	.784389E-02	.137731E-01	.423202E+00	.870540E-01	.562101E-01
10	.124152E+01	.000000E+00	.494303E-03	.291780E-01	.277557E+00	.000000E+00	.818209E-02

[*] Diffusion coefficients are in cm and cross sections are in cm^{-1} ; no upscattering.

[**] From left to right of the assembly

Table 3-8. Cross Section[*] Data for Assembly 5

Material #[**]	D_1	$\nu\sigma_{f1}$	σ_{a1}	σ_{12}	D_2	$\nu\sigma_{f2}$	σ_{a2}
1	.122965E+01	.000000E+00	.509310E-03	.300991E-01	.274934E+00	.000000E+00	.828368E-02
2	.132110E+01	.318544E-02	.974767E-02	.136133E-01	.419990E+00	.558469E-01	.545154E-01
3	.133902E+01	.345481E-02	.909815E-02	.123717E-01	.417492E+00	.645840E-01	.593034E-01
4	.133386E+01	.363393E-02	.942208E-02	.118380E-01	.417709E+00	.722484E-01	.641240E-01
5	.132318E+01	.274190E-02	.715081E-02	.152664E-01	.364127E+00	.520350E-01	.480830E-01
6	.132341E+01	.282721E-02	.703014E-02	.155714E-01	.363790E+00	.541166E-01	.488156E-01
7	.133293E+01	.386514E-02	.946561E-02	.113599E-01	.416041E+00	.802240E-01	.682536E-01
8	.133796E+01	.379774E-02	.928761E-02	.114561E-01	.414607E+00	.771718E-01	.661796E-01
9	.132366E+01	.361035E-02	.972077E-02	.122524E-01	.416248E+00	.712566E-01	.630325E-01
10	.128269E+01	.000000E+00	.602301E-03	.235516E-01	.313506E+00	.000000E+00	.746432E-02

[*] Diffusion coefficients are in cm and cross sections are in cm^{-1} ; no upscattering.

[**] From left to right of the assembly

Table 3-9. Cross Section[*] Data for Assembly 6

Material #[**]	D_1	$\nu\sigma_{f1}$	σ_{a1}	σ_{12}	D_2	$\nu\sigma_{f2}$	σ_{a2}
1	.129676E+01	.000000E+00	.586354E-03	.225763E-01	.318163E+00	.000000E+00	.732088E-02
2	.133757E+01	.537239E-02	.880688E-02	.119636E-01	.414007E+00	.110721E+00	.737301E-01
3	.135063E+01	.568988E-02	.857664E-02	.112871E-01	.412227E+00	.116708E+00	.794471E-01
4	.134570E+01	.582692E-02	.873877E-02	.111657E-01	.413776E+00	.122522E+00	.820451E-01
5	.133753E+01	.426455E-02	.649957E-02	.150814E-01	.364382E+00	.839712E-01	.567871E-01
6	.133846E+01	.420883E-02	.657689E-02	.147676E-01	.363679E+00	.826763E-01	.578628E-01
7	.134912E+01	.560637E-02	.864986E-02	.115892E-01	.413849E+00	.118378E+00	.785372E-01
8	.135434E+01	.522557E-02	.832292E-02	.121641E-01	.413774E+00	.106964E+00	.718649E-01
9	.133755E+01	.433802E-02	.848741E-02	.132915E-01	.418015E+00	.853734E-01	.619111E-01
10	.124513E+01	.000000E+00	.493887E-03	.286684E-01	.277157E+00	.000000E+00	.819725E-02

[*] Diffusion coefficients are in cm and cross sections are in cm^{-1} ; no upscattering.

[**] From left to right of the assembly
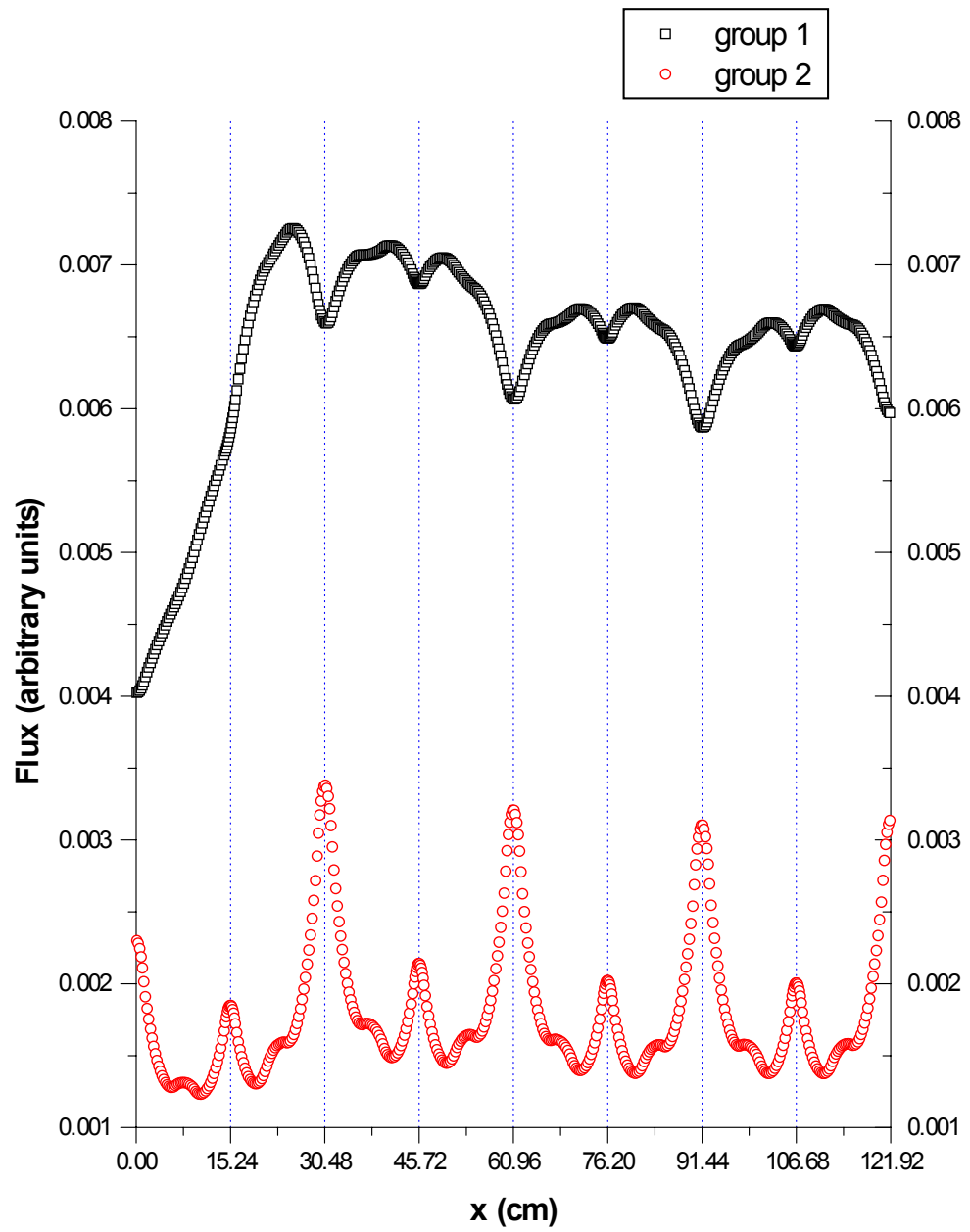
Figure 3-6. Flux Distribution in Configuration A
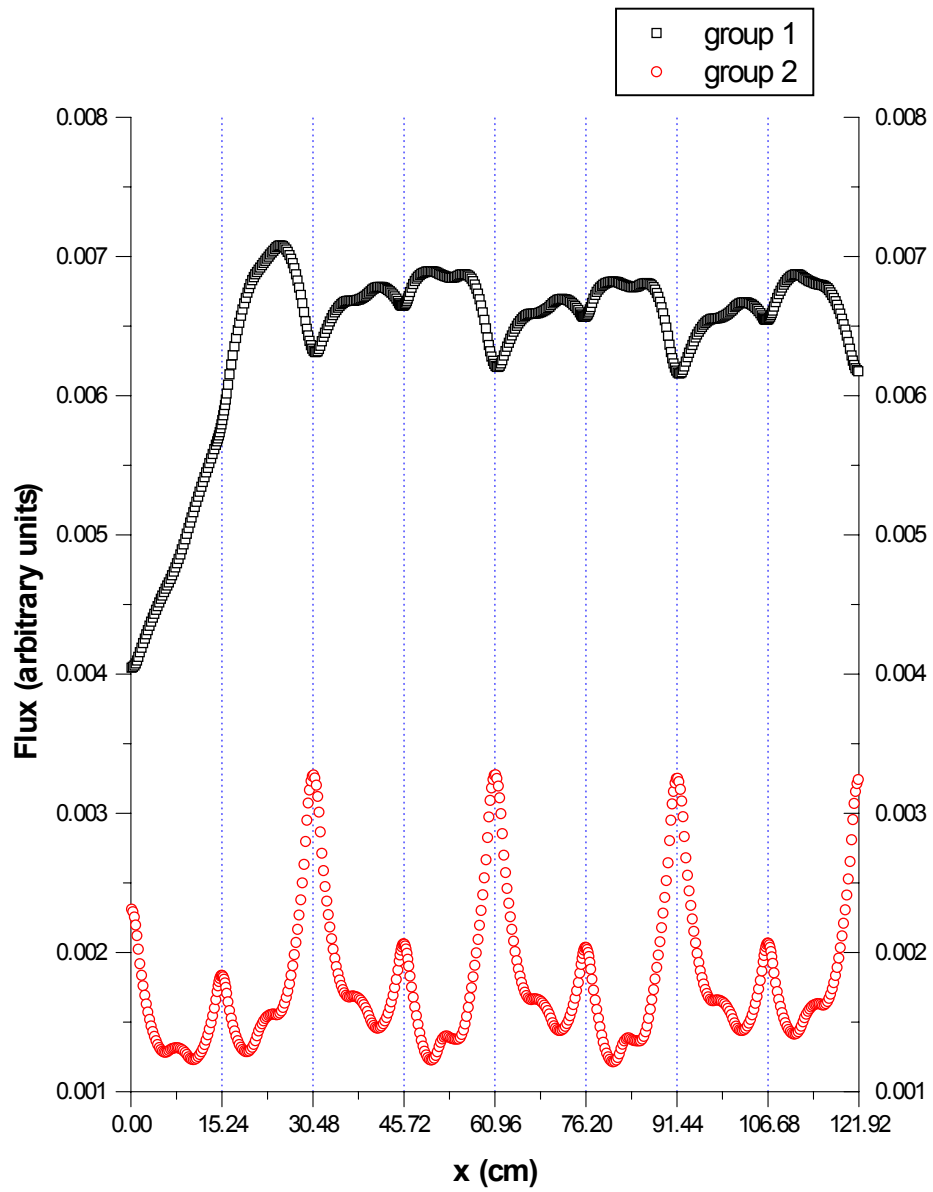
F

igure 3-7. Flux Distribution in Configuration B
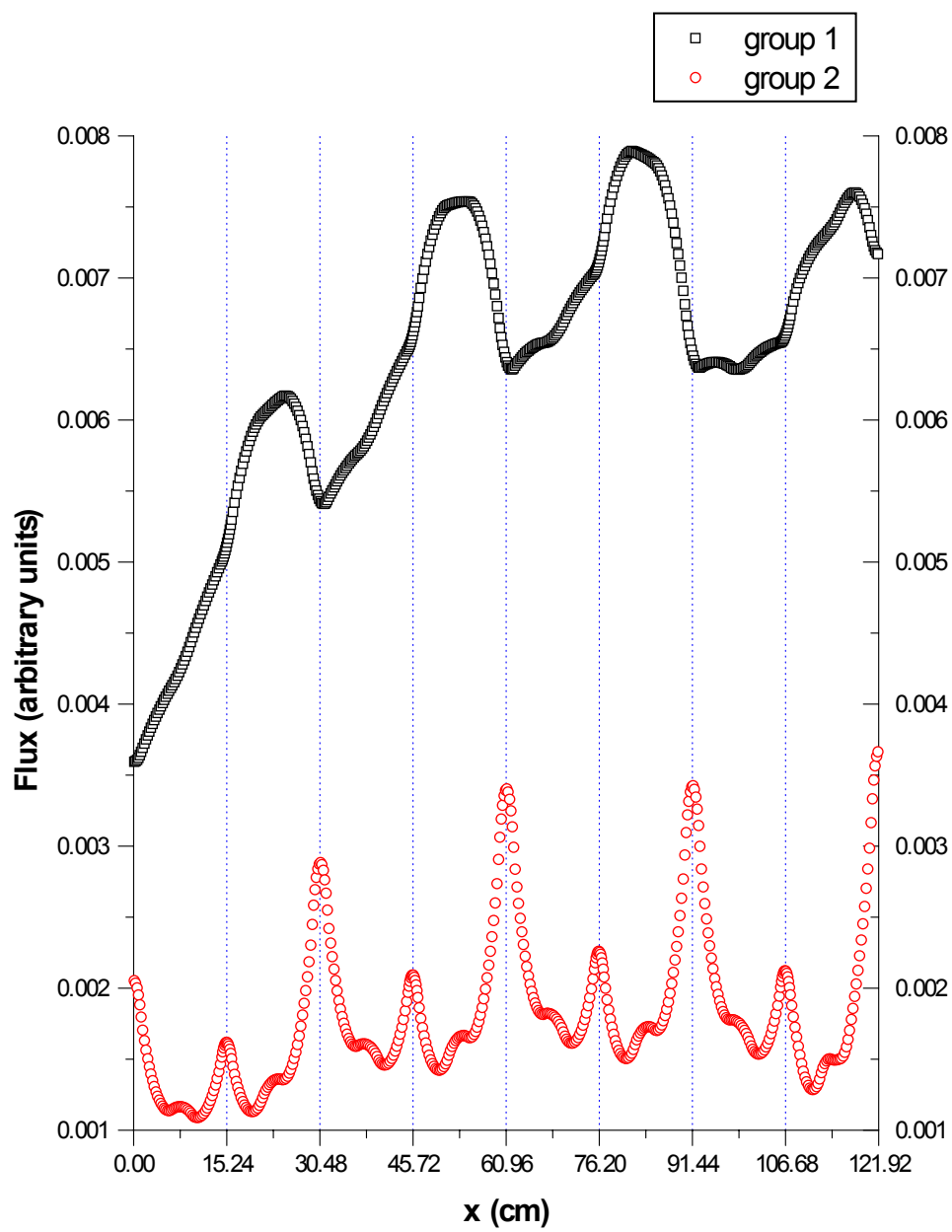
Figure 3-8. Flux Distribution in Configuration C
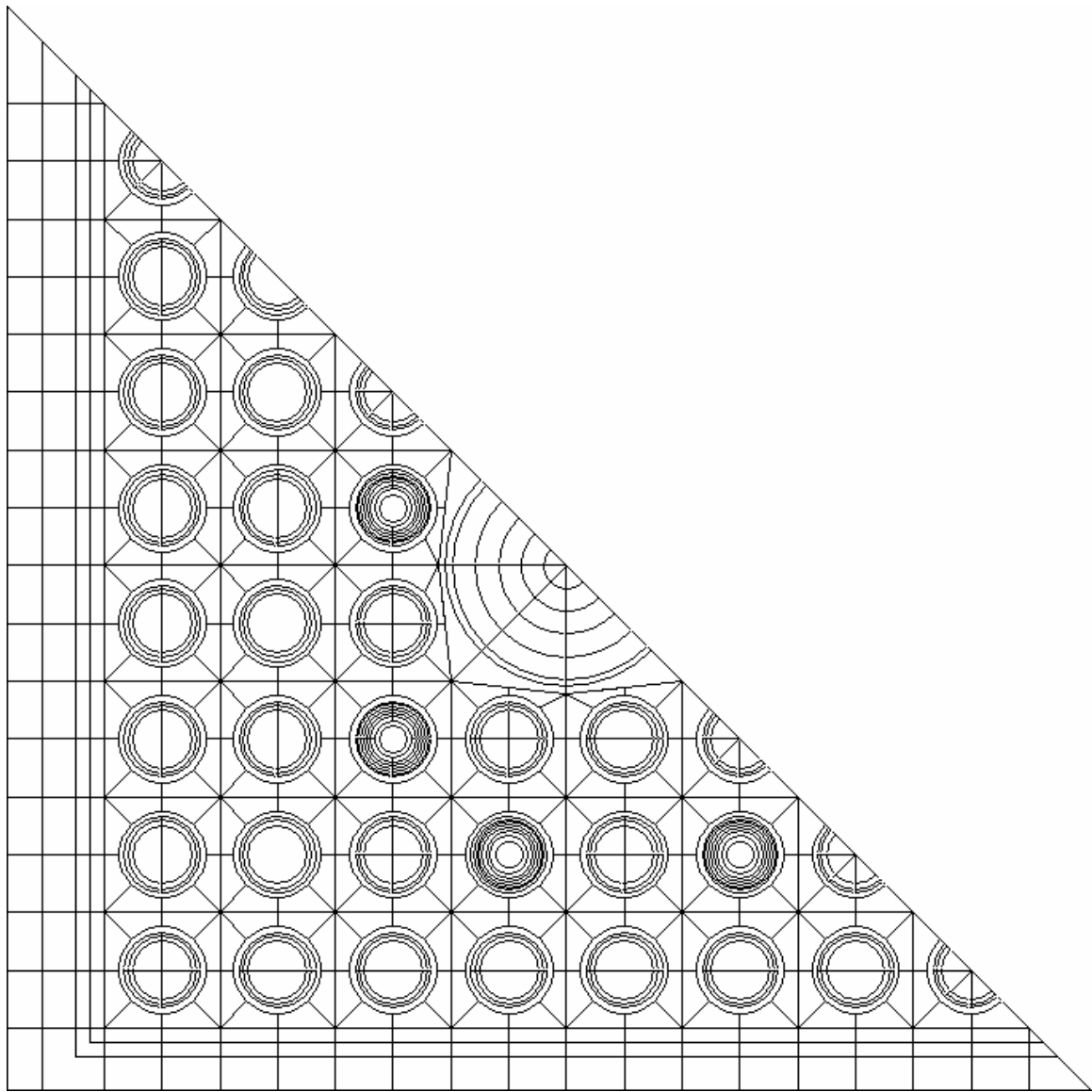
Figure 3-9. HELIOS Model of the GE-9 Fuel Assembly

Chapter IV

Results

4.1. The Convergence of the Expansion Series in the Multigroup Case

The convergence of the expansion series (see Eqs. 1-5, 1-6, 1-11) in the multigroup case is tested using as a benchmark configuration an assembly typical of a BWR in slab geometry (see Figure 3-1).

A two-group fine-mesh diffusion code was developed to precompute the data (forward and ajoint fluxes, and Green's function) required for calculating the expansion coefficients. The fine-mesh calculations are performed with six meshes per each material region, leading to a total of thirty-six meshes per assembly. An infinite-medium (net zero current) boundary condition is used as the initial state of the assembly. Then different perturbations of the boundary condition (current-to-flux ratio) are considered: those subjected to when the assembly is located in core configurations 1 and 2 as shown in Figure 3-1.

These current-to-flux ratios are determined for each assembly by performing fine-mesh diffusion calculations for the full core (configuration 2). For each perturbation, the expansion coefficients for the flux and the eigenvalue are calculated, and the corrected values are compared to the "exact" values. The "exact" value here means the flux and eigenvalue obtained from fine-mesh assembly calculation, using for the boundary condition the corresponding current-to-flux ratio obtained from the fine-mesh core calculations.

4.1.1. Results for Assembly #1

The flux and eigenvalue results for assembly 1 (see Figure 3-1) are shown in Table 4-1 for different magnitudes of the perturbation, corresponding to four different

positions of the assembly in configurations 1 and 2. The first two cases correspond to assembly 1 in the first and the third position from left to right in configuration 1, and the other two cases correspond to the same positions in configuration 2. The results corresponding to the assembly in the seventh and fifth position from left to right in the same configuration are not shown in the table, but they are similar. The similarity of the results corresponding to symmetric positions of the assembly (e.g. first with seventh, third with fifth) in a configuration constituted one of the tests for assessing the correctness of the numerical implementation. Another test consisted of verifying if the integral over the phase-space of any high-order coefficient in the flux expansion is zero, as it should be according to the theoretical model (see Eq. 2-6). In one case for example (see case 1 in Table 3-3), with $\left|\varphi_{1,g}(i)\right| > 10^{-4}, i = 1,..N$, $g = 1,2$, where i is a mesh index and g is a group index, a value of the order 10^{-8} was obtained for the integral of the first-order flux.

The comparison of the reference and the calculated flux distributions is made by means of the flux RMS, which is defined as:

$$RMS = 100\left[\frac{1}{N-1}\sum_{i=1}^{N}\left(\frac{\phi_{reference,i} - \phi_{calculated,i}}{\phi_{reference,i}}\right)^2\right]^{1/2} \qquad (4\text{-}1)$$

where N is the total number of meshes.

The method produces very good results. The flux RMS is less than 0.1% and the corrected eigenvalue is within 0.6% of the reference value for all four cases. For small perturbations (cases 1 and 2) an expansion up to the second order is sufficient to obtain a very good agreement, whereas for larger perturbations (cases 3 and 4) four or five orders need to be considered. To illustrate the change in the flux distribution with the order of the perturbation, the flux distribution for case 3 is shown in Figure 4-1 up to the fourth order. It can be seen that there is a large shape difference between the infinite medium flux and the exact (reference) flux, especially for the fast group; the corrected solutions oscillate around the reference, until at the fourth-order most of the difference is

accounted for by the perturbation method. For the other three cases the flux distributions are shown in Figures 4-2 to 4-4.

The high-order corrected assembly-homogenized cross sections and discontinuity factors, for the same sets of perturbations as considered in Table 4-1, are presented in Table 4-2 for the fast group, and in Table 4-4 for the thermal group. For small perturbations, one or two terms in the expansion of the homogenized cross sections are sufficient to reproduce the reference values, whereas for larger perturbations five terms are needed to obtain a similar agreement.

The agreement is also very good for the discontinuity factors, even though the magnitude of the initial perturbation is larger compared to that for the cross sections (e.g., the error for the heterogeneous discontinuity factor on the right boundary is -34% in case 3 and -20% in case 4). The second order correction of the discontinuity factors reproduce the reference values in cases 1 and 2. In cases 3 and 4, the corrected values at the fifth order are within 0.15% of the reference results.

It needs to be mentioned that the two configurations in which assembly 1 is considered are quite different. Core 1 (corresponding to cases 1 and 2) is a very simple configuration, with small gradients of the flux at the node interface. Core 2 is a more restrictive configuration, with large flux gradients at the interfaces and a significant change of the flux across the core. The other type of assembly (type 3) in core 2 has gadolinium in two of its four fuel regions.

Table 4-1. Flux and Eigenvalue Results for Assembly #1[*]

Case #[a]	$(J/\Phi)_{left}$ fast/ thermal	$(J/\Phi)_{right}$ fast/ thermal	Reference Eigenvalue λ_{ref}	Ord. of Pert.	Calculated Eigenvalue λ_{calc}	Error[b]	Fast Flux RMS (%)	Thermal Flux RMS (%)
1	0. 0.	0.4556E-02 -0.3652E-03	0.75766	0 1 2 3	0.75037 0.75764 0.75754 0.75754	-0.96 0.00 -0.02 -0.02	0.71 0.01 0.01 0.01	0.53 0.01 0.01 0.01
2	-0.1988E-02 0.5822E-03	0.3129E-02 -0.4851E-03	0.75794	0 1 2 3	0.75037 0.75762 0.75756 0.75756	-1.00 -0.04 -0.05 -0.05	0.31 0.00 0.00 0.00	0.24 0.00 0.00 0.00
3	0. 0.	0.1026 0.1178E-01	0.89167	0 1 2 3 4 5	0.75037 0.94218 0.88328 0.89731 0.89515 0.89512	-15.85 5.66 -0.94 0.63 0.39 0.39	15.75 4.03 0.60 0.11 0.13 0.07	18.75 5.31 0.98 0.21 0.12 0.08
4	-0.1382E-01 -0.5439E-02	0.7057E-01 0.9505E-02	0.89170	0 1 2 3 4 5	0.75037 0.91549 0.89365 0.89714 0.89670 0.89672	-15.85 2.67 0.22 0.61 0.56 0.56	8.97 1.72 0.17 0.06 0.05 0.05	11.01 2.42 0.33 0.10 0.05 0.05

*As shown in Figure 3-1
[a] Cases 1 and 2 refer to two different positions in configuration 1, cases 3 and 4 refer to two different positions in configuration 2
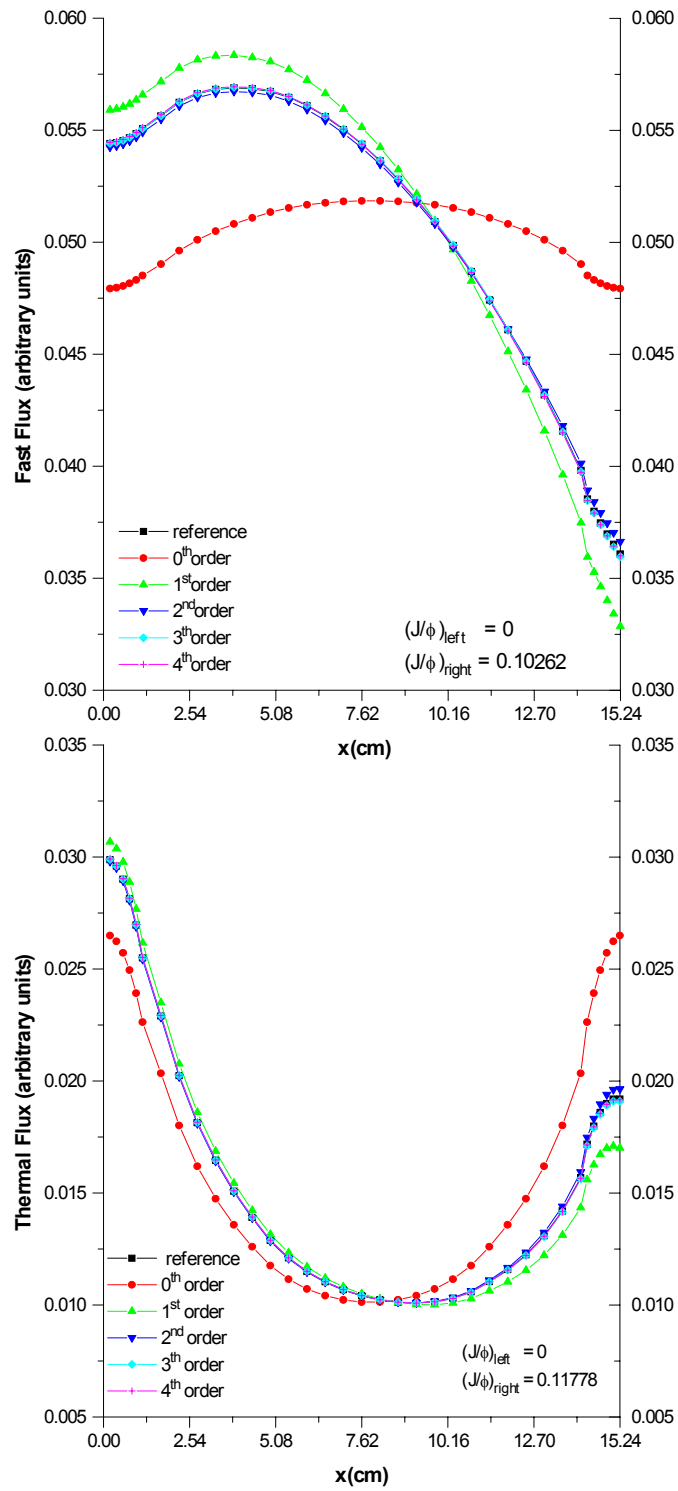[b] Calculated as $100*(\lambda_{calc} - \lambda_{ref})/ \lambda_{ref}$

Figure 4-1. Flux Distribution in Case 3

46

Table 4-2. Fast Group Cross Sections[*] for Assembly #1

Case #[**]	Order of Pert.	D (err)[e]	$\nu\sigma_f$ (err)	σ_r (err)	σ_{12} (err)	χ_{left}[f] (err)	χ_{right} (err)
1[a]	reference	1.5182	6.2100E-3	8.4738E-3	1.9046E-2	0.9548	0.9362
	0	1.5184 (-0.01)	6.2063E-3 (0.06)	8.4793E-3 (0.05)	1.9056E-2 (-0.05)	0.9490 (0.61)	0.9490 (-1.37)
	1	1.5182 (0.00)	6.2100E-3 (0.00)	8.4738E-3 (0.00)	1.9046E-2 (0.00)	0.9549 (-0.01)	0.9360 (0.02)
	2	1.5182 (0.00)	6.2100E-3 (0.00)	8.4738E-3 (0.00)	1.9046E-2 (0.00)	0.9548 (0.00)	0.9362 (0.00)
2[b]	reference	1.5182	6.2104E-3	8.4743E-3	1.9045E-2	0.9476	0.9476
	0	1.5184 (-0.01)	6.2063E-3 (0.07)	8.4793E-3 (0.06)	1.9056E-2 (-0.06)	0.9490 (-0.15)	0.9490 (-0.67)
	1	1.5182 (0.00)	6.2004E-3 (0. 00)	8.4743E-3 (0. 00)	1.9045E-2 (0. 00)	0.9476 (0. 00)	0.9426 (0. 01)
3[c]	reference	1.5162	6.2713E-3	8.5476E-3	1.8880E-2	1.0769	0.7083
	0	1.5184 (-0.14)	6.2063E-3 (1.04)	8.4793E-3 (0.92)	1.9056E-2 (-0.93)	0.9490 (11.14)	0.9490 (-33.97)
	1	1.5155 (0.05)	6.2929E-3 (-0.34)	8.5737E-3 (-0.31)	1.8821E-2 (0.31)	1.0942 (-2.46)	0.6430 (9.22)
	2	1.5164 (-0.01)	6.2660E-3 (0.08)	8.5411E-3 (0.08)	1.8895E-2 (-0.08)	1.0658 (0.20)	0.7197 (-1.61)
	3	1.5161 (0.00)	6.2726E-3 (-0.02)	8.5492E-3 (-0.02)	1.8876E-2 (0.02)	1.0681 (-0.01)	0.7060 (0.33)
	4	1.5162 (0.00)	6.2715E-3 (0.00)	8.5478E-3 (0.00)	1.8880E-2 (0.00)	1.0691 (-0.11)	0.7067 (0.22)
	5	1.5162 (0.00)	6.2715E-3 (0.00)	8.5478E-3 (0.00)	1.8880E-2 (0.00)	1.0691 (-0.06)	0.7067 (0.15)
4[d]	reference	1.5163	6.2693E-3	8.5451E-3	1.8886E-2	0.9915	0.7890
	0	1.5184 (-0.14)	6.2063E-3 (1.00)	8.4793E-3 (0.89)	1.9056E-2 (-0.90)	0.9490 (4.29)	0.9490 (-20.28)
	1	1.5159 (0.02)	6.2782E-3 (-0.14)	8.5559E-3 (-0.13)	1.8861E-2 (0.13)	1.0052 (-1.39)	0.7597 (3.71)
	2	1.5163 (0.00)	6.2680E-3 (0.02)	8.5434E-3 (0.02)	1.8889E-2 (-0.02)	0.9903 (0.12)	0.7924 (-0.43)
	3	1.5162 (0.00)	6.2697E-3 (-0.01)	8.5456E-3 (-0.01)	1.8885E-2 (0.01)	0.9919 (-0.04)	0.7878 (0.14)
	4	1.5162 (0.00)	6.2695E-3 (0.00)	8.5453E-3 (0.00)	1.8885E-2 (0.00)	0.9919 (-0.04)	0.7882 (0.10)

[*] The diffusion coefficient is in cm, and the cross sections are in cm^{-1}

[**] Cases 1 and 2 - two different positions in config. 1; cases 3 and 4 - two different positions in config. 2

[a] $(J/\phi)_{left}$=0; $(J/\phi)_{right}$= 0.4556E-02

[b] $(J/\phi)_{left}$=-0.1988E-02 ; $(J/\phi)_{right}$= 0.3129E-02

[c] $(J/\phi)_{left}$=0; $(J/\phi)_{right}$= 0.1026

[d] $(J/\phi)_{left}$=-0.1382E-01 ; $(J/\phi)_{right}$= 0.7057E-01

[e] Calculated as 100*(reference-calculated)/reference

[f] Heterogeneous discontinuity factor calculated as the ratio of the surface flux to the assembly average flux

Table 4-3. Thermal Group Cross Sections[*] for Assembly #1

Case #[**]	Order of Pert.	D (err)[e]	$\nu\sigma_f$ (err)	σ_r (err)	χ_{left}[f] (err)	χ_{right} (err)
1[a]	reference	3.0591E-1	1.0198E-1	6.3763E-2	1.7649	1.7431
	0	3.0589E-1 (0.00)	1.0196E-1 (0.02)	6.3752E-2 (0.02)	1.7545 (0.59)	1.7545 (-0.65)
	1	3.0591E-1 (0.00)	1.0198E-1 (0.00)	6.3763E-2 (0.00)	1.7650 (-0.01)	1.7430 (0.01)
	2	3.0591E-1 (0.00)	1.0198E-1 (0.00)	6.3763E-2 (0.00)	1.7649 (0.00)	1.7431 (0.00)
2[b]	reference	3.0587E-1	1.0193E-1	6.3739E-2	1.7617	1.7524
	0	3.0589E-1 (-0.01)	1.0196E-1 (-0.02)	6.3752E-2 (-0.02)	1.7545 (0.41)	1.7545 (-0.12)
	1	3.0587E-1 (0.00)	1.0193E-1 (0.00)	6.3739E-2 (0.00)	1.7617 (0.00)	1.7524 (0.00)
3[c]	reference	3.0695E-1	1.0351E-1	6.4558E-2	2.0371	1.3086
	0	3.0589E-1 (0.35)	1.0196E-1 (1.50)	6.3752E-2 (1.25)	1.7545 (13.87)	1.7545 (-34.08)
	1	3.0728E-1 (-0.01)	1.0399E-1 (-0.47)	6.4808E-2 (-0.39)	2.1134 (-3.75)	1.1720 (10.44)
	2	3.0688E-1 (0.02)	1.0341E-1 (0.10)	6.4507E-2 (0.08)	2.0259 (0.55)	1.3352 (-2.03)
	3	3.0696E-1 (0.00)	1.0353E-1 (-0.02)	6.4568E-2 (-0.01)	2.0392 (-0.10)	1.3027 (0.45)
	4	3.0696E-1 (0.00)	1.0352E-1 (-0.01)	6.4562E-2 (-0.01)	2.0393 (-0.11)	1.3061 (0.19)
	5	3.0696E-1 (0.00)	1.0352E-1 (0.00)	6.4560E-2 (0.00)	2.0384 (-0.07)	1.3061 (0.15)
4[d]	reference	3.0719E-1	1.0385E-1	6.4736E-2	1.8335	1.4682
	0	3.0589E-1 (0.42)	1.0196E-1 (1.83)	6.3752E-2 (1.52)	1.7545 (4.31)	1.7545 (-19.50)
	1	3.0731E-1 (-0.04)	1.0403E-1 (-0.17)	6.4828E-2 (-0.14)	1.8712 (-2.05)	1.4010 (4.58)
	2	3.0718E-1 (0.00)	1.0384E-1 (0.02)	6.4727E-2 (0.01)	1.8280 (0.30)	1.4779 (-0.66)
	3	3.0720E-1 (0.00)	1.0386E-1 (-0.01)	6.4740E-2 (-0.01)	1.8349 (-0. 07)	1.4655 (0.18)
	4	3.0720E-1 (0.00)	1.0386E-1 (-0.01)	6.4739E-2 (0.00)	1.8343 (-0. 04)	1.4669 (0.09)

[*] The diffusion coefficient is in cm, and the cross sections are in cm^{-1}

[**] Cases 1 and 2 - two different positions in config. 1; cases 3 and 4 - two different positions in config. 2

[a] $(J/\phi)_{left}$= 0; $(J/\phi)_{right}$= -0.3652E-3

[b] $(J/\phi)_{left}$= 0.5822E-03 ; $(J/\phi)_{right}$= -0.4851E-03

[c] $(J/\phi)_{left}$= 0; $(J/\phi)_{right}$= 0.1178E-01

[d] $(J/\phi)_{left}$=-0.5439E-02 ; $(J/\phi)_{right}$= 0.9505E-02

[e] Calculated as 100*(reference-calculated)/reference

[f] Heterogeneous discontinuity factor calculated as the ratio of the surface flux to the assembly average flux
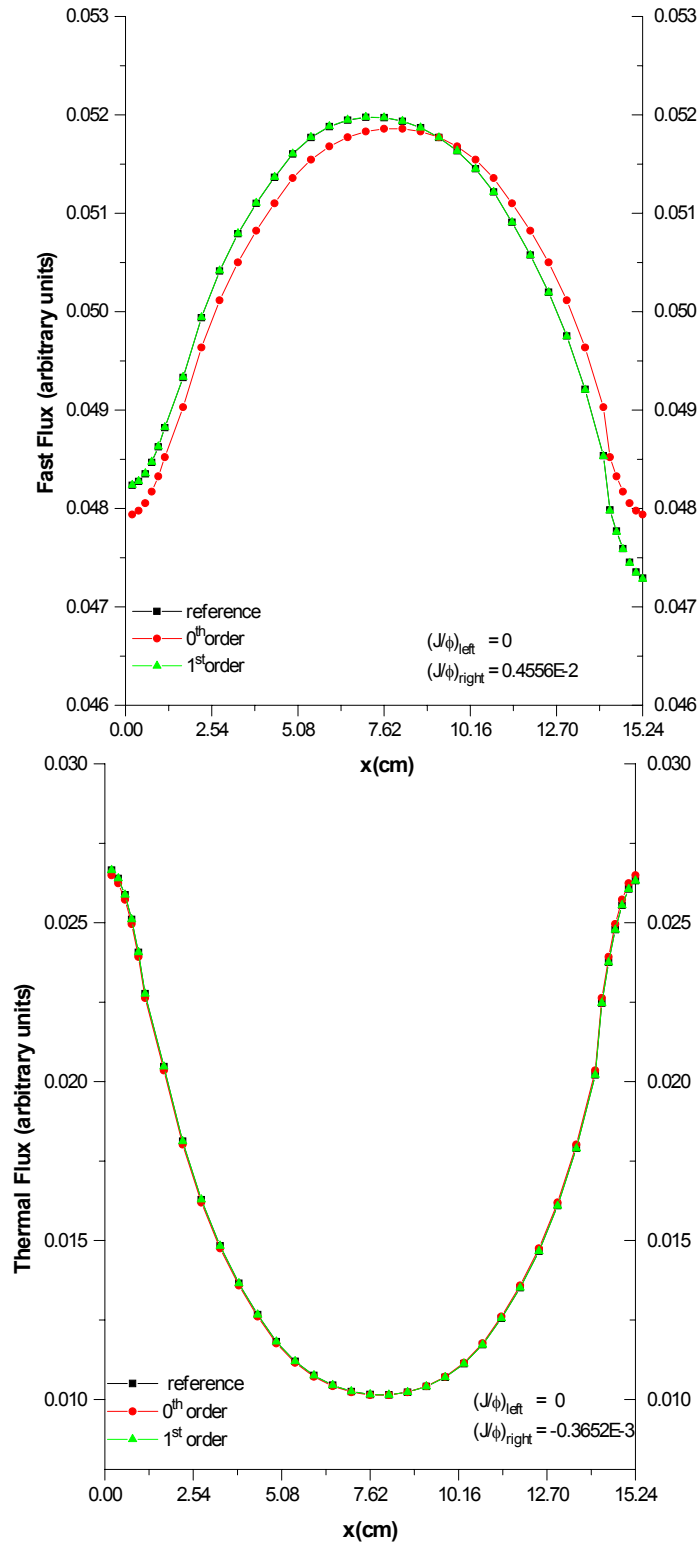
Figure 4-2. Flux Distribution in Case 1
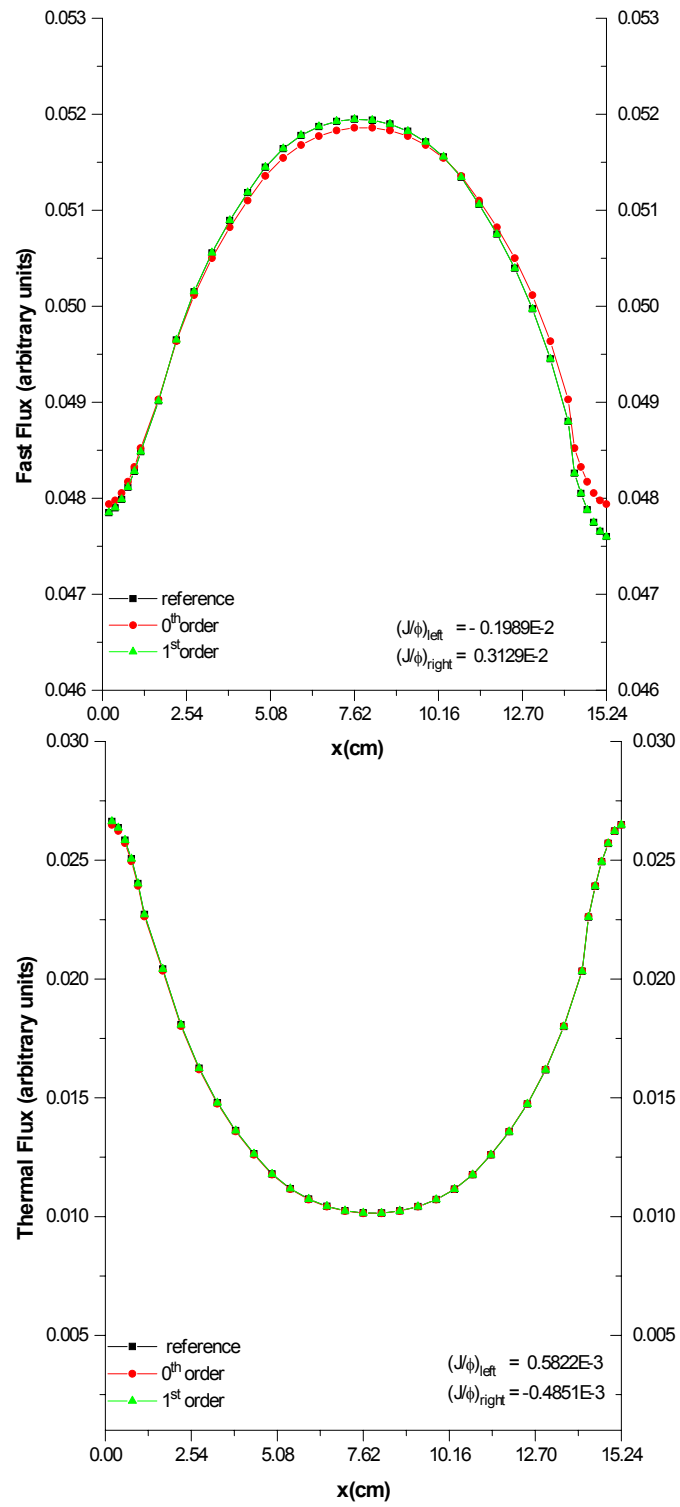
Figure 4-3. Flux Distribution in Case 2

50
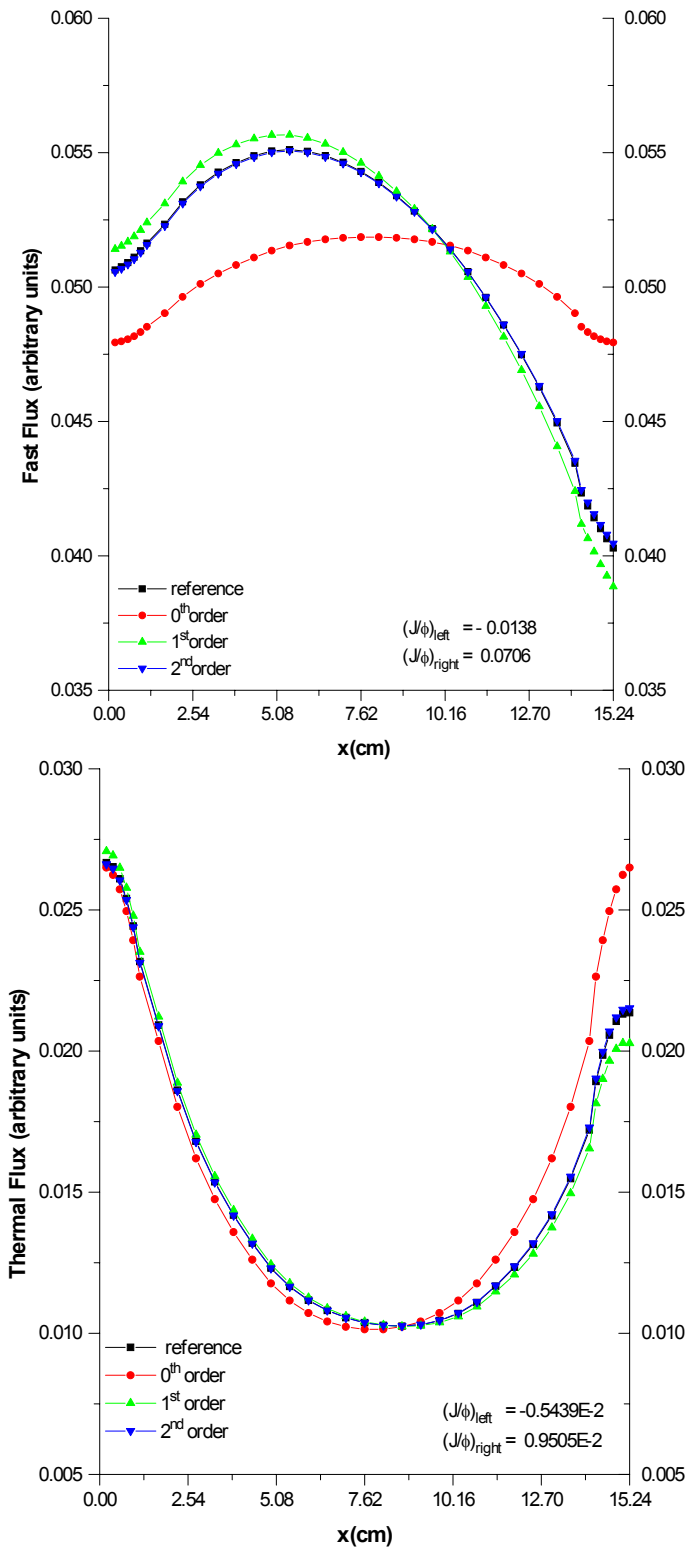
Figure 4-4. Flux Distribution in Case 4

4.1.2. Results for Assembly #3

The flux and eigenvalue results for assembly 3 (see Figure 3-1) are shown in Table 4-4, for two values of the perturbation of the boundary condition, corresponding to the following position of the assembly in configuration 2: second from left to right, and at the center. The magnitude of the perturbation is quite large, compared to the perturbation of the boundary condition for assembly 1 in the same configuration.   In case 5 for example, the initial eigenvalue is 68% off from the reference value, whereas the initial flux RMS error is 21% for the fast flux and 23% for the thermal flux. A plot of the flux distribution for this last case is shown in Figure 4-5. This figure gives a good indication of how large the perturbations are and that the method improves the results substantially. Flux distribution for case 6 is shown in Figure 4-6.

The high-order homogenized cross sections and discontinuity factors corresponding to assembly 3 are shown in Table 4-5 and 4-6 for the fast group and for the thermal group, respectively.   The corrected values agree very well with the reference results. If the initial perturbation is larger, as it is the case for the discontinuity factors, higher orders corrections are needed to obtain a very good agreement. For example, five orders are required to reduce an initial error of –32% in the thermal discontinuity factor on the right boundary down to 0.05%.

Table 4-4. Flux and Eigenvalue Results for Assembly #3[*]

Case #[a]	$(J/\Phi)_{left}$ fast/ thermal	$(J/\Phi)_{right}$ fast/ thermal	Reference Eigenvalue λ_{ref}	Ord. of Pert.	Calculated Eigenvalue λ_{calc}	Error[b]	Fast Flux RMS (%)	Thermal Flux RMS (%)
5	0.1026 0.1178E-01	-0.1382E-1 -0.5439E-2	0.89168	0	1.49772	67.97	21.24	22.68
				1	1.03008	15.52	3.15	4.54
				2	0.93150	4.47	0.51	0.42
				3	0.91292	2.38	0.37	0.35
				4	0.91289	2.38	0.11	0.11
				5	0.91421	2.53	0.05	0.05
6	0.7057E-1 0.9505E-2	-0.7057E-1 -0.9505E-2	0.89170	0	1.49772	67.96	5.00	8.21
				1	0.93438	4.79	0.31	0.85
				2	0.91297	2.39	0.03	0.11
				3	0.91365	2.46	0.02	0.04
				4	0.91385	2.48	0.02	0.03
				5	0.91386	2.49	0.02	0.03

[*] As shown in Figure 3-1

[a] Cases 1 and 2 refer to two different positions in configuration 2

[b] Calculated as $100*(\lambda_{calc} - \lambda_{ref})/ \lambda_{ref}$

The upper plot shows Fast Flux (arbitrary units) on the y-axis (ranging from 0.040 to 0.080) versus x(cm) from 0.00 to 15.24. Legend: reference, 0th order, 1st order, 2nd order, 3th order, 4th order. Annotations: $(J/\phi)_{left} = 0.10262$, $(J/\phi)_{right} = -0.01382$.

The lower plot shows Thermal Flux (arbitrary units) on the y-axis (ranging from 0.000 to 0.045) versus x(cm) from 0.00 to 15.24. Legend: reference, 0th order, 1st order, 2nd order, 3th order, 4th order. Annotations: $(J/\phi)_{left} = 0.01178$, $(J/\phi)_{right} = -0.00544$.
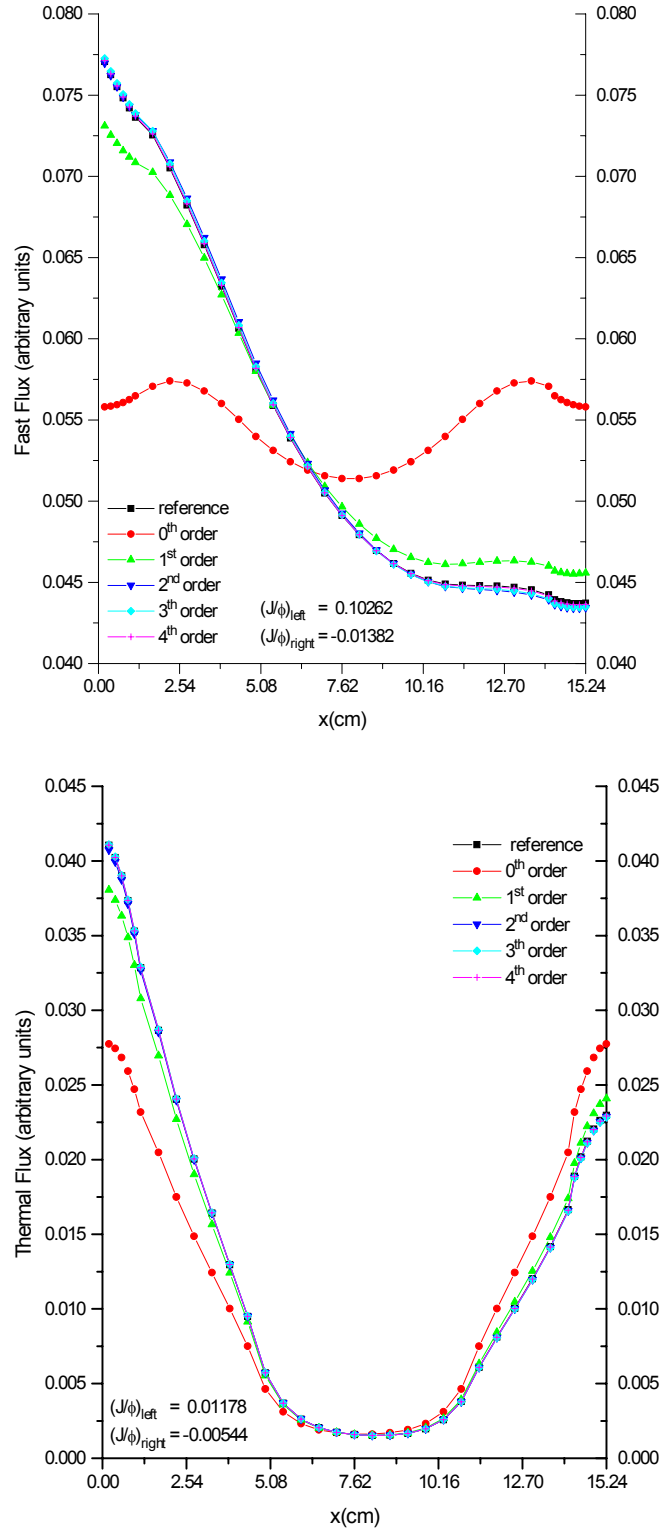
Figure 4-5. Flux Distribution in Case 5

Table 4-5. Fast Group Cross Sections[*] for Assembly #3

Case #[**]	Order of Pert.	D (err)[d]	$\nu\sigma_f$ (err)	σ_r (err)	σ_{12} (err)	χ_{left}[e] (err)	χ_{right} (err)
5[a]	reference	1.54594	5.14140E-3	9.56391E-3	1.88051E-2	1.43396	0.81358
	0	1.54312 (0.18)	5.21060E-3 (-1.35)	9.73547E-3 (-1.79)	1.84941E-2 (1.65)	1.01945 (28.91)	0.8136 (-25.30)
	1	1.54526 (0.04)	5.15810E-3 (-0.32)	9.60378E-3 (-0.42)	1.87318E-2 (0.39)	1.35486 (5.52)	0.84464 (-3.82)
	2	1.54580 (0.01)	5.14489E-3 (-0.07)	9.57187E-3 (-0.08)	1.87902E-2 (0.08)	1.43080 (0.22)	0.80743 (0.76)
	3	1.54592 (0.00)	5.14189E-3 (-0.01)	9.56487E-3 (-0.01)	1.88032E-2 (0.01)	1.43750 (-0.25)	0.80901 (0.56)
	4	1.54593 (0.00)	5.14160E-3 (0.00)	9.56431E-3 (0.00)	1.88043E-2 (0.00)	1.43484 (-0.06)	0.81219 (0.17)
	5	1.54593 (0.00)	5.14169E-3 (-0.01)	9.56457E-3 (-0.01)	1.88038E-2 (0.01)	1.43373 (0.02)	0.81293 (0.08)
6[b]	reference	1.54594	5.14140E-3	9.56392E-3	1.88051E-2	1.12377	1.12377
	0	1.54312 (0.18)	5.21060E-3 (-1.35)	9.73547E-3 (-1.79)	1.84941E-2 (1.65)	1.01945 (9.28)	0.8136 (9.28)
	1	1.54571 (0.02)	5.14706E-3 (-0.11)	9.57627E-3 (-0.13)	1.87815E-2 (0.13)	1.11683 (0.62)	1.11683 (0.62)
	2	1.54591 (0.00)	5.14202E-3 (-0.01)	9.56517E-3 (-0.01)	1.88026E-2 (0.01)	1.12314 (0.06)	1.12314 (0.06)
	3	1.54593 (0.00)	5.14167E-3 (-0.01)	9.56450E-3 (-0.01)	1.88040E-2 (0.01)	1.12340 (0.03)	1.12340 (0.03)

[*] The diffusion coefficient is in cm, and the cross sections are in cm^{-1}
[**] Cases 5 and 6 refer to two different positions in configuration 2
[a] $(J/\phi)_{left}$= 0.1026; $(J/\phi)_{right}$= -0.1382E-1
[b] $(J/\phi)_{left}$= 0.7057E-1; $(J/\phi)_{right}$= -0.7057E-1
[d] Calculated as 100*(reference-calculated)/reference
[e] Heterogeneous discontinuity factor calculated as the ratio of the surface flux to the assembly average flux

Table 4-6. Thermal Group Cross Sections* for Assembly #3

Case #**	Order of Pert.	D (err)^d	$\nu\sigma_f$ (err)	σ_r (err)	χ_{left}^{e} (err)	χ_{right} (err)
5^a	reference	2.89695E-1	6.77120E-2	8.85175E-2	3.45807	1.93438
	0	2.91040E-1 (-0.46)	6.86045E-2 (-1.32)	9.30339E-2 (-5.10)	2.55019 (26.25)	2.55019 (-31.84)
	1	2.89897E-1 (-0.07)	6.78493E-2 (-0.20)	8.91802E-2 (-0.75)	3.26539 (5.57)	2.06684 (-6.85)
	2	2.89725E-1 (-0.01)	6.77346E-2 (-0.03)	8.86076E-2 (-0.10)	3.44447 (0.39)	1.93466 (-0.01)
	3	2.89698E-1 (0.00)	6.77143E-2 (0.00)	8.85184E-2 (0.00)	3.46451 (-0.19)	1.92541 (0.46)
	4	2.89697E-1 (0.00)	6.77144E-2 (0.00)	8.85262E-2 (-0.01)	3.46011 (-0.06)	1.93128 (0.16)
	5	2.89701E-1 (0.00)	6.77159E-2 (-0.01)	8.85354E-2 (-0.02)	3.45788 (0.01)	1.93337 (0.05)
6^b	reference	2.89695E-1	6.77122E-2	8.85182E-2	2.69620	2.69620
	0	2.91040E-1 (-0.46)	6.86045E-2 (-1.32)	9.30339E-2 (-5.10)	2.55019 (5.42)	2.55019 (5.42)
	1	2.89732E-1 (-0.01)	6.77486E-2 (-0.05)	8.85844E-2 (-0.07)	2.68075 (0.57)	2.68075 (0.57)
	2	2.89699E-1 (0.00)	6.77158E-2 (-0.01)	8.85264E-2 (-0.01)	2.69425 (0.07)	2. 69425 (0.07)
	3	2.89700E-1 (0.00)	6.77157E-2 (-0.01)	8.85334E-2 (-0.02)	2.69551 (0.03)	2. 69551 (0.03)

* The diffusion coefficient is in cm, and the cross sections are in cm^{-1}
** Cases 5 and 6 refer to two different positions in configuration 2
^{a} $(J/\phi)_{left}$= 0.1178E-1; $(J/\phi)_{right}$= -0.5439E-2
^{b} $(J/\phi)_{left}$= 0.9505E-2; $(J/\phi)_{right}$= -0.9505E-2
^{d} Calculated as 100*(reference-calculated)/reference
^{e} Heterogeneous discontinuity factor calculated as the ratio of the surface flux to the assembly average flux

The upper graph shows Fast Flux (arbitrary units) vs x(cm), with curves for reference, 0th order, 1st order, and 2nd order. Values annotated: $(J/\phi)_{left} = 0.7057E-1$ and $(J/\phi)_{right} = -0.7057E-1$.

The lower graph shows Thermal Flux (arbitrary units) vs x(cm), with curves for reference, 0th order, and 1st order. Values annotated: $(J/\phi)_{left} = 0.9505E-2$ and $(J/\phi)_{right} = -0.9505E-2$.
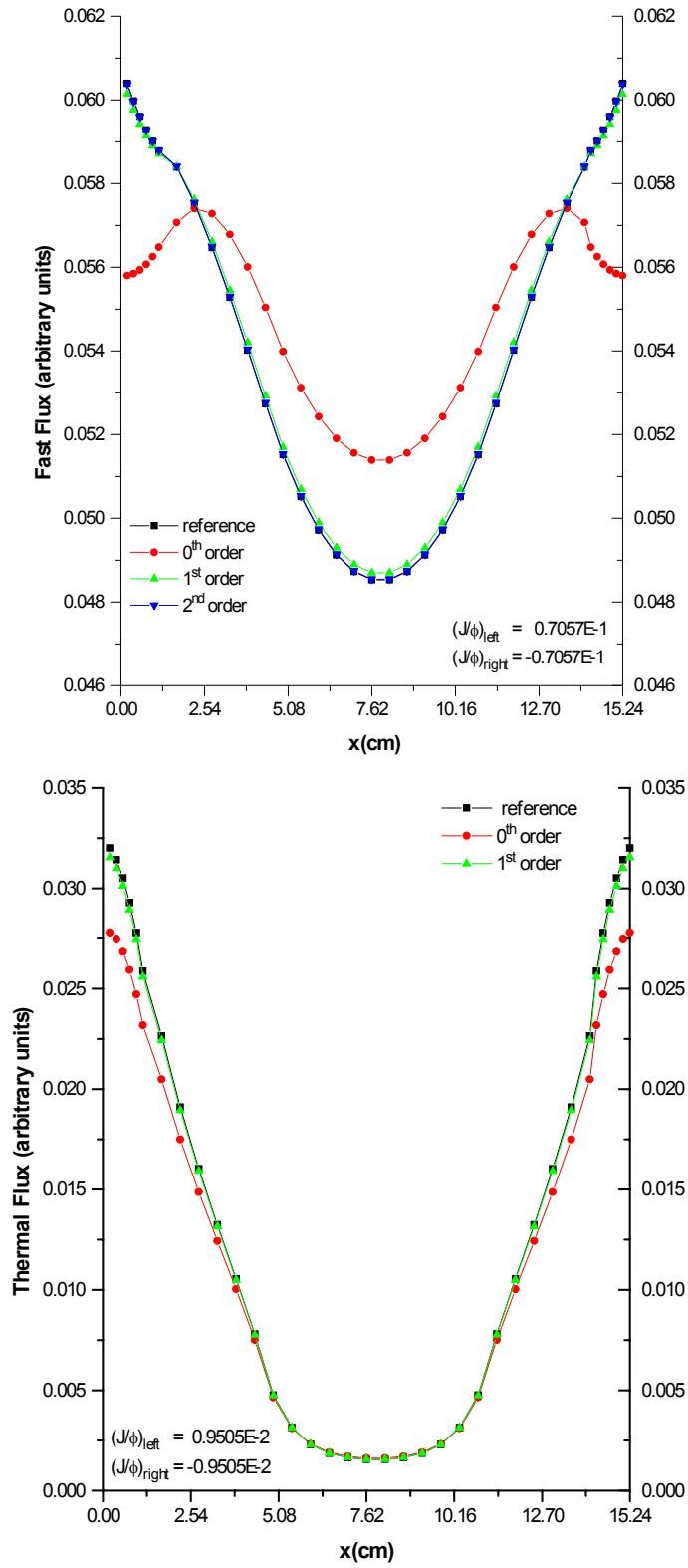
Figure 4-6. Flux Distribution in Case 6

4.2. High-Order Cross Section Homogenization for Two-Group Nodal Diffusion

4.2.1. Results for Configurations 1 and 2

Configuration 1 is a very simple configuration, with small gradients of the flux at the node interface (see Figure 3-2). For this configuration, the use of the standard GET nodal parameters leads to a good agreement of the nodal calculations with the fine-mesh core calculations. That is, there is no need to correct the nodal parameters in this case. Therefore, only results for configurations 2 are shown in this section.

The distribution of the nodal flux at different orders of corrections for the nodal parameters is compared to the reference distribution in Figures 4-7 and 4-8 for the fast flux and for the thermal flux, respectively. The full core fine-mesh calculation is taken as the reference. The node-integrated flux, as well as the assembly reconstructed fine-mesh flux is compared to the assembly reference flux, for different orders of the correction of the nodal cross sections, in Tables 4-7 and 4-8 for the fast and thermal flux, respectively. Only results for nodes 1 through 4 are shown, given the symmetry.

It can be seen from the above tables that the zeroth order node-integrated fast flux overestimates the reference value in those nodes where assembly 1 is positioned (3.2% and 2.3%), but underestimates the reference value in the nodes where assembly 3 is present (-7.1% and –7.7%). The errors corresponding to the zeroth order thermal flux in each node (up to 14% in absolute value) are about twice as large as the fast flux errors. The difference is reduced to less than 1% at the third order, for both groups, and becomes less than 0.5% at the fourth order.

The error of the assembly reconstructed flux, at a high order of the correction, has the same order of magnitude as that of the node-integrated flux in the corresponding node. The first and second order corrected reconstructed fine-mesh flux is compared to the reference fine-mesh flux distribution in Figure 4-9 for group 1 and in Figure 4-10 for group 2. It can be seen that even the reconstructed flux shape corresponding to the second order approximates the shape of the reference flux in both groups very well. At

the fourth order, not shown in the figures, the corrected and the reference flux shapes are practically identical.

The distribution of the zeroth order reconstructed flux is shown in Figure 4-11 for the fast flux and in Figure 4-12 for the thermal flux. The difference between the distributions is more pronounced in the center of the core for both the thermal and the fast fluxes.
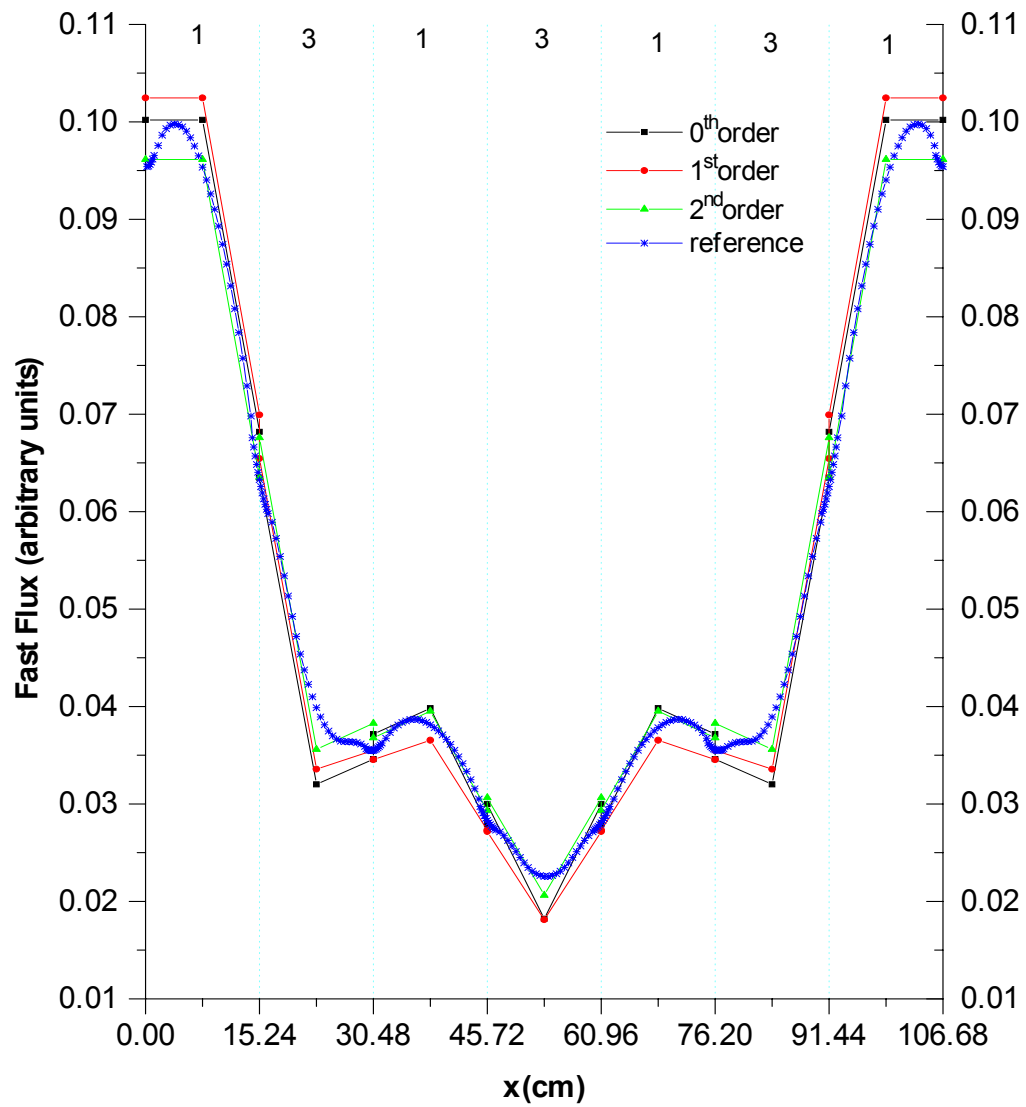
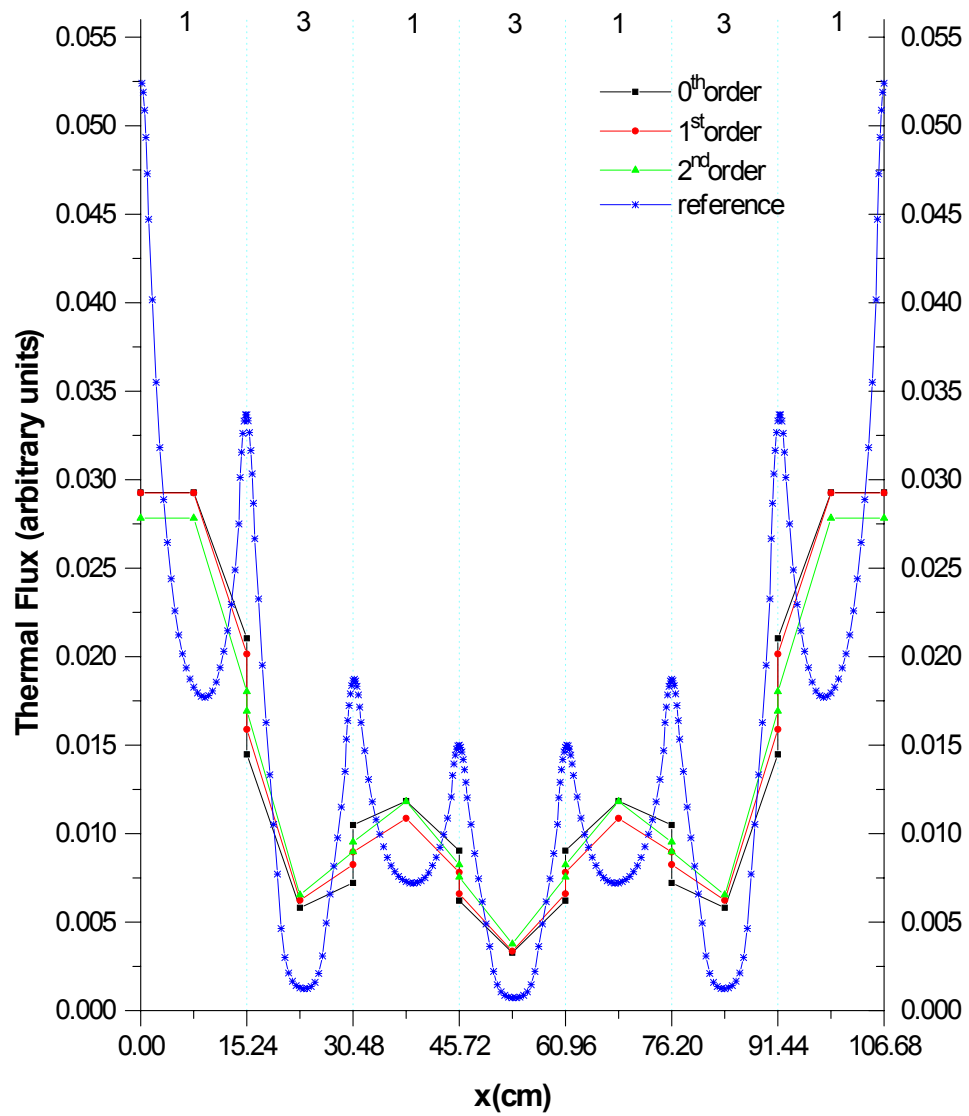**Figure 4-7. Nodal Fast Flux Distribution in Core 2**

Figure 4-8. Nodal Thermal Flux Distribution in Core 2

Table 4-7. Assembly Fast Flux in Core 2

Order of Perturbation	Assembly Position	Reference	Nodal	Error[a]	Reconstructed	Error[a]
0	1	1.3614	1.4051	3.20	1.3901	2.10
	2	0.6650	0.6176	-7.14	0.6536	-1.72
	3	0.5465	0.5593	2.33	0.5456	-0.17
	4	0.3807	0.3514	-7.70	0.3366	-11.60
1	1	1.3614	1.4376	5.59	1.4404	5.80
	2	0.6650	0.6404	-3.69	0.6416	-3.51
	3	0.5465	0.5142	-5.91	0.5146	-5.83
	4	0.3807	0.3450	-9.39	0.3455	-9.25
2	1	1.3614	1.3409	-1.51	1.3402	-1.56
	2	0.6650	0.6748	1.47	0.6752	1.53
	3	0.5465	0.5530	1.18	0.5528	1.15
	4	0.3807	0.3907	2.62	0.3909	2.66
3	1	1.3614	1.3648	0.25	1.3650	0.26
	2	0.6650	0.6674	0.37	0.6676	0.39
	3	0.5465	0.5416	-0.89	0.5416	-0.90
	4	0.3807	0.3793	-0.38	0.3794	-0.36
4	1	1.3614	1.3611	-0.02	1.3611	-0.03
	2	0.6650	0.6676	0.39	0.6677	0.40
	3	0.5465	0.5442	-0.43	0.5441	-0.44
	4	0.3807	0.3814	0.16	0.3814	0.18
5	1	1.3614	1.3595	-0.14	1.3595	-0.14
	2	0.6650	0.6678	0.42	0.6679	0.43
	3	0.5465	0.5452	-0.24	0.5451	-0.25
	4	0.3807	0.3822	0.38	0.3822	0.39
6	1	1.3614	1.3599	-0.11	1.3599	-0.11
	2	0.6650	0.6677	0.41	0.6678	0.42
	3	0.5465	0.5450	-0.29	0.5449	-0.30
	4	0.3807	0.3820	0.32	0.3820	0.34
7	1	1.3614	1.3600	-0.11	1.3599	-0.11
	2	0.6650	0.6678	0.42	0.6678	0.43
	3	0.5465	0.5449	-0.29	0.5448	-0.31
	4	0.3807	0.3819	0.32	0.3820	0.33
8	1	1.3614	1.3600	-0.11	1.3600	-0.11
	2	0.6650	0.6678	0.42	0.6678	0.43
	3	0.5465	0.5449	-0.30	0.5448	-0.31
	4	0.3807	0.3819	0.31	0.3820	0.33
9	1	1.3614	1.3600	-0.11	1.3600	-0.11
	2	0.6650	0.6678	0.42	0.6678	0.43
	3	0.5465	0.5449	-0.30	0.5448	-0.31
	4	0.3807	0.3819	0.31	0.3820	0.33
10	1	1.3614	1.3600	-0.11	1.3600	-0.11
	2	0.6650	0.6678	0.42	0.6678	0.43
	3	0.5465	0.5449	-0.30	0.5448	-0.31
	4	0.3807	0.3819	0.31	0.3820	0.33

[a]Defined as 100*(calculated-reference)/reference

Table 4-8. Assembly Thermal Flux in Core 2

Order of Perturbation	Assembly Position	Reference	Nodal	Error[a]	Reconstructed	Error[a]
0	1	0.3920	0.4148	5.80	0.3699	-5.65
	2	0.1469	0.1269	-13.60	0.1761	19.88
	3	0.1557	0.1646	5.71	0.1462	-6.08
	4	0.0841	0.0723	-14.06	0.1004	19.42
1	1	0.3920	0.4111	4.85	0.4082	4.13
	2	0.1469	0.1395	-5.00	0.1383	-5.81
	3	0.1557	0.1467	-5.78	0.1463	-6.05
	4	0.0841	0.0759	-9.71	0.0754	-10.33
2	1	0.3920	0.3867	-1.37	0.3874	-1.19
	2	0.1469	0.1485	1.11	0.1481	0.82
	3	0.1557	0.1577	1.33	0.1579	1.43
	4	0.0841	0.0862	2.50	0.0861	2.36
3	1	0.3920	0.3931	0.26	0.3929	0.22
	2	0.1469	0.1471	0.11	0.1469	0.02
	3	0.1557	0.1545	-0.76	0.1546	-0.72
	4	0.0841	0.0837	-0.50	0.0836	-0.57
4	1	0.3920	0.3921	0.00	0.3921	0.01
	2	0.1469	0.1471	0.16	0.1470	0.10
	3	0.1557	0.1552	-0.30	0.1553	-0.25
	4	0.0841	0.0841	0.04	0.0841	-0.02
5	1	0.3920	0.3916	-0.12	0.3916	-0.12
	2	0.1469	0.1471	0.18	0.1471	0.13
	3	0.1557	0.1555	-0.11	0.1556	-0.07
	4	0.0841	0.0843	0.25	0.0843	0.19
6	1	0.3920	0.3917	-0.09	0.3917	-0.09
	2	0.1469	0.1471	0.16	0.1471	0.12
	3	0.1557	0.1554	-0.16	0.1555	-0.11
	4	0.0841	0.0843	0.20	0.0842	0.14
7	1	0.3920	0.3917	-0.08	0.3917	-0.08
	2	0.1469	0.1471	0.17	0.1471	0.12
	3	0.1557	0.1554	-0.17	0.1555	-0.12
	4	0.0841	0.0843	0.19	0.0842	0.13
8	1	0.3920	0.3917	-0.08	0.3917	-0.08
	2	0.1469	0.1471	0.17	0.1471	0.12
	3	0.1557	0.1554	-0.17	0.1555	-0.12
	4	0.0841	0.0843	0.19	0.0842	0.13
9	1	0.3920	0.3917	-0.08	0.3917	-0.08
	2	0.1469	0.1471	0.17	0.1471	0.12
	3	0.1557	0.1554	-0.17	0.1555	-0.12
	4	0.0841	0.0843	0.19	0.0842	0.13
10	1	0.3920	0.3917	-0.08	0.3917	-0.08
	2	0.1469	0.1471	0.17	0.1471	0.12
	3	0.1557	0.1554	-0.17	0.1555	-0.12
	4	0.0841	0.0843	0.19	0.0842	0.13

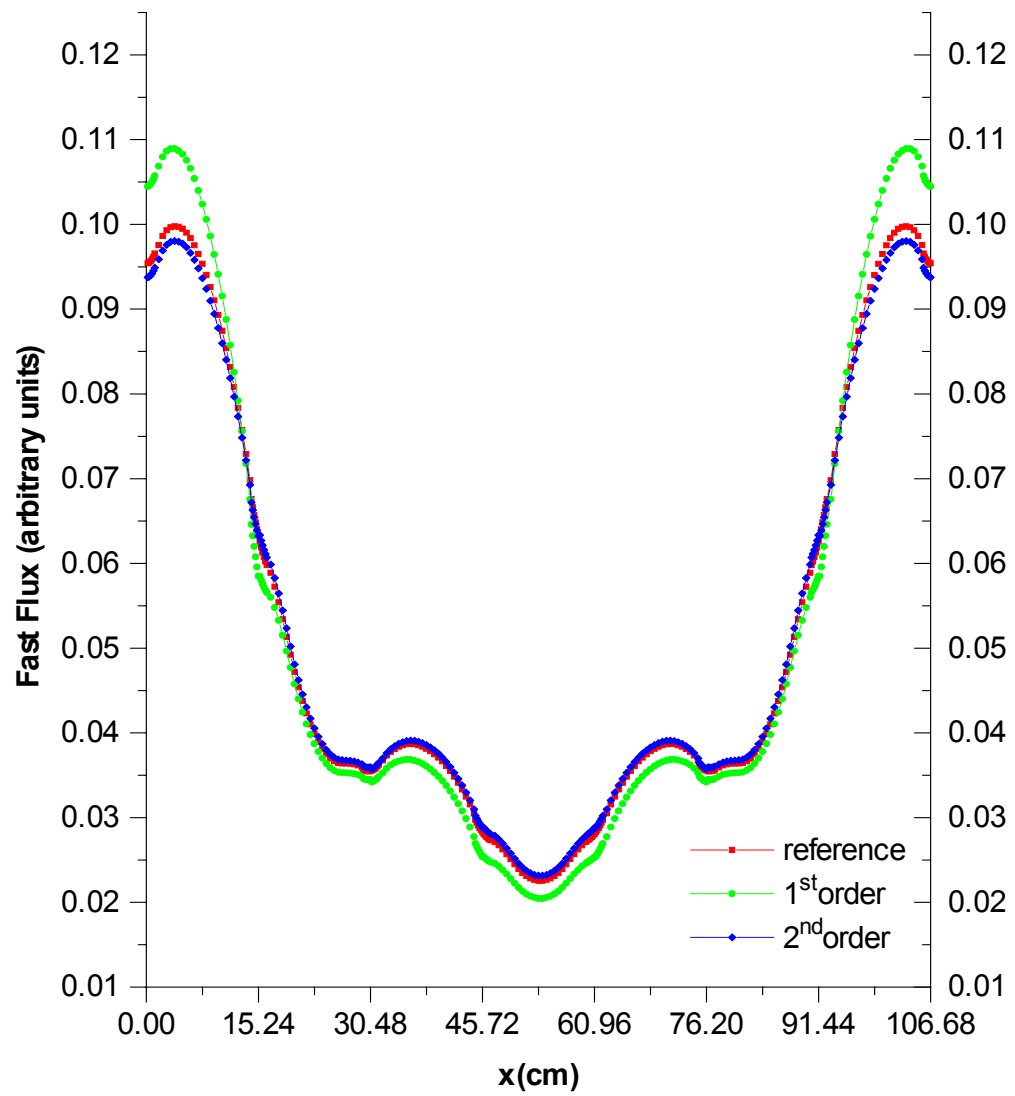[a]Defined as 100*(calculated-reference)/reference

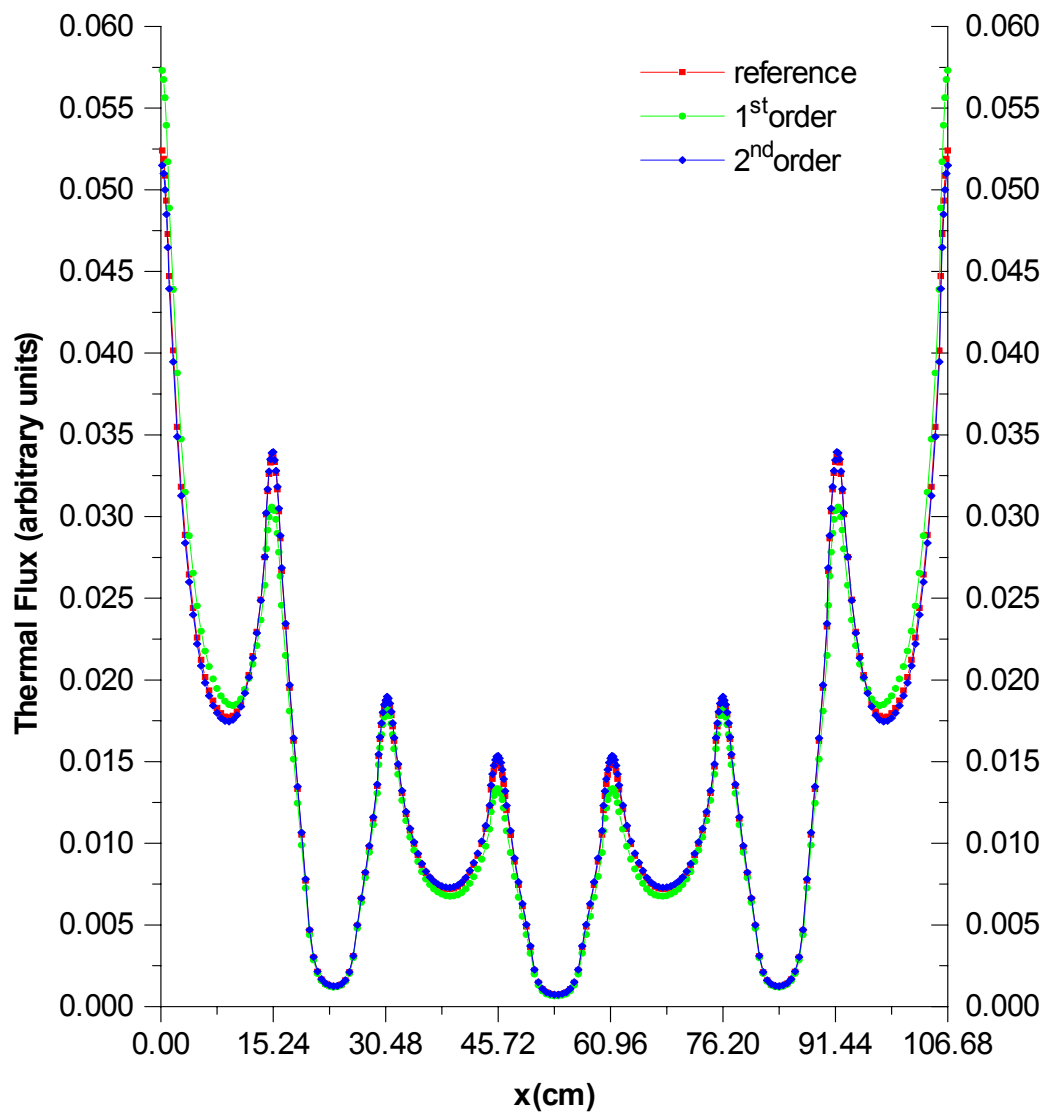**Figure 4-9. High-Order Reconstructed Flux in Group 1 in Core 2**

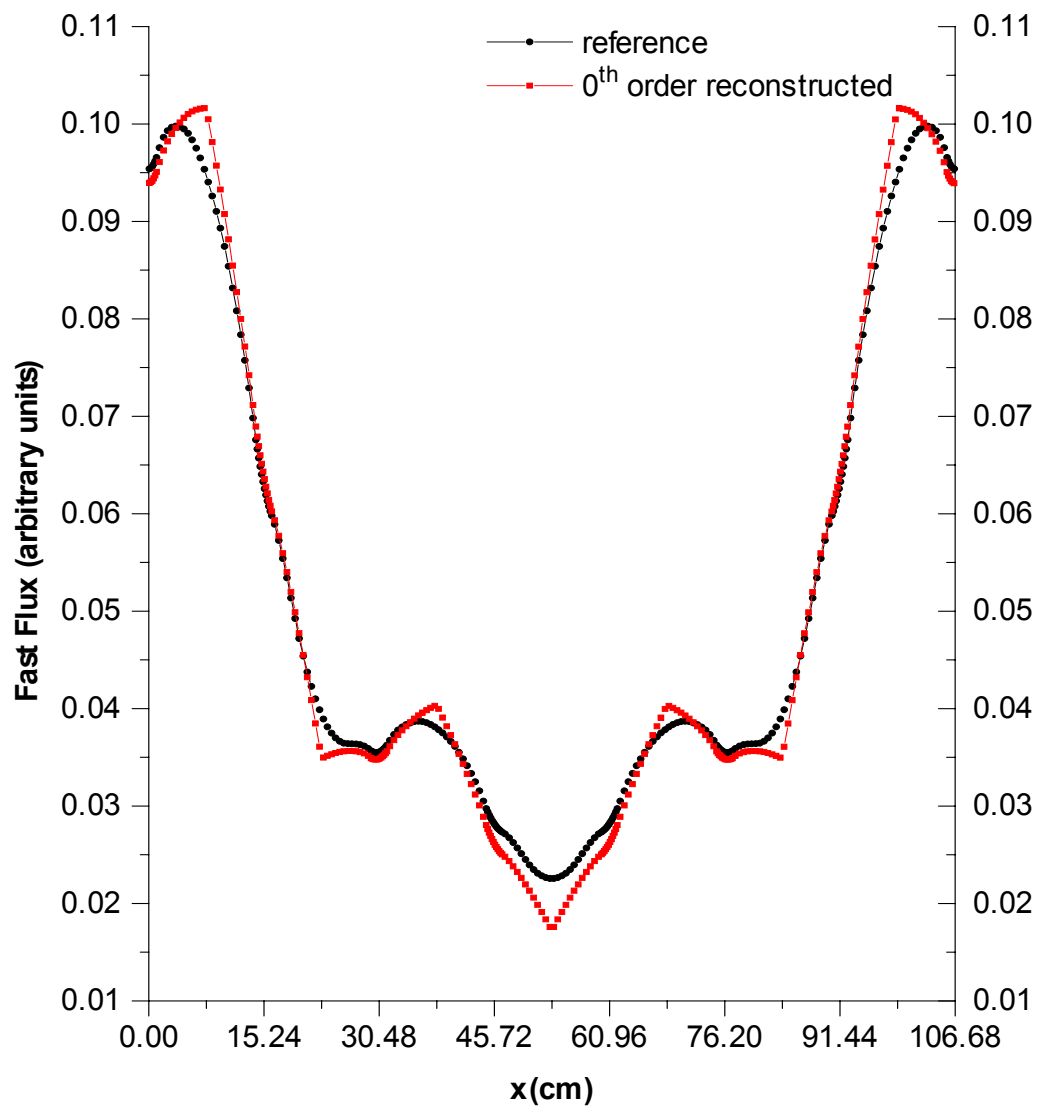**Figure 4-10. High-Order Reconstructed Flux in Group 2 in Core 2**

Figure 4-11. Zeroth Order Reconstructed Flux in Group 1 in Core 2
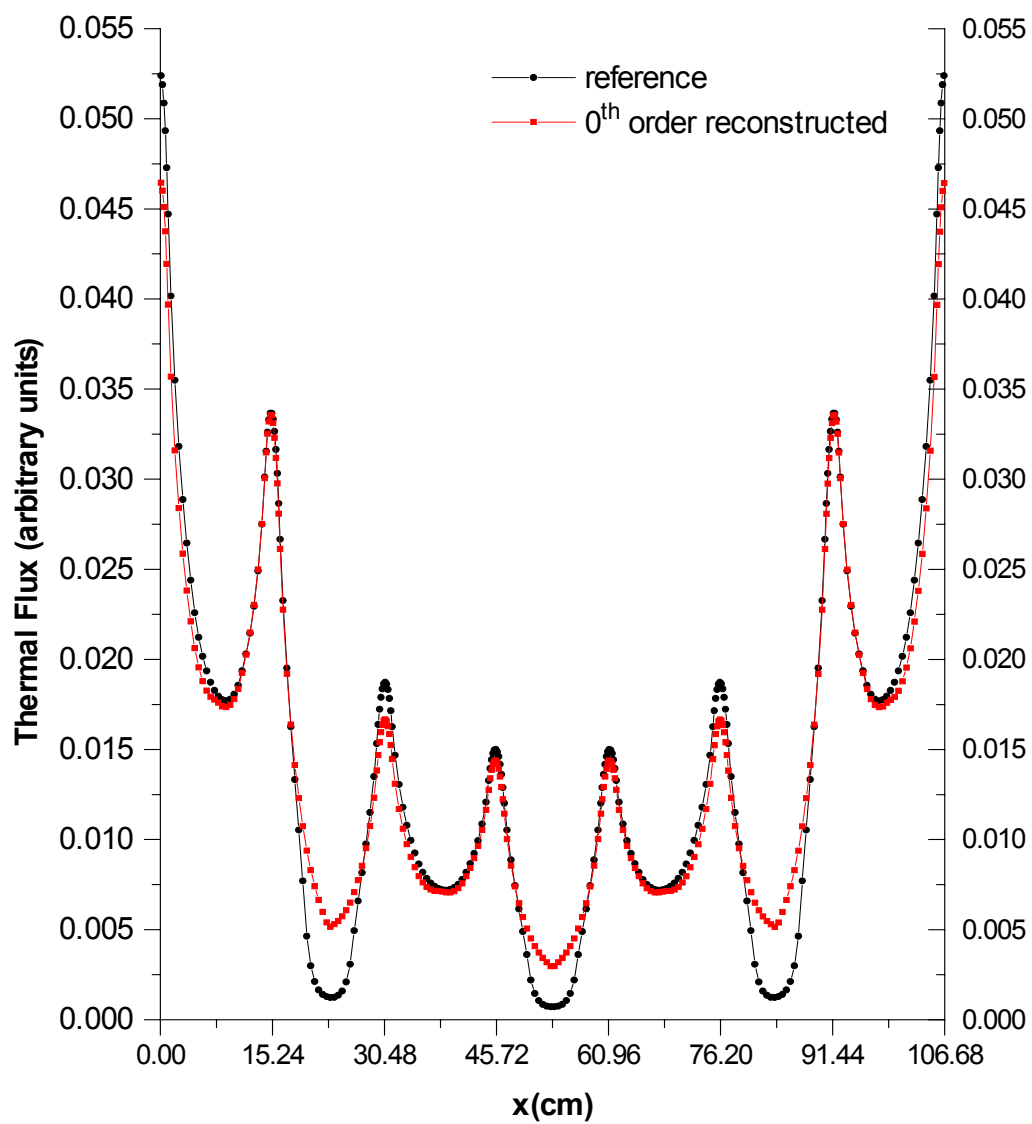
Figure 4-12. Zeroth Order Reconstructed Flux in Group 2 in Core 2

4.2.2. Results for the Newly Developed Benchmark Configurations (A, B and C)

As it was for the two configurations discussed in the previous section, the reference case here is a fine-mesh calculation of the full configuration with a zero current boundary condition. Six meshes are considered for each material region, giving a total of 60 meshes per assembly and 960 meshes per core. Because of the symmetry, only the distribution for the left half of the configuration is shown.

The multiplication constant (k_{eff}) for each core (see Figure 3-5) at different orders of the correction for the nodal cross sections is given in Table 4-9. The distribution of the reconstructed flux, calculated as specified in section 2-3, is shown in Figures 4-13 to 4-18. Only the first order reconstructed flux is shown, the higher-order distributions being almost identical to the reference distribution for each core. It is interesting to note that, even though the zeroth order (standard GET) k_{eff} practically reproduce the reference value for cores A and C (within 10^{-3}), or is very close to it as in case of core B (within 10^{-2}), it does not approximate well the flux distribution. The difference is mostly in the fast group, and it is more pronounced in the case of the more heterogeneous core C. The node-integrated flux from the nodal calculation and the assembly-integrated reconstructed flux for each group are compared to the reference results in Tables 4-10 to 4-15. The difference of up to 5% in the node-integrated flux at the zeroth order is reduced to less than 1% at the third order.

Table 4-9. K_{eff} for Cores A, B and C

Core	K_{ref}*	Order of correction	K_{calc}	K_{calc}- K_{ref} (mk**)
A	1.0130	0	1.0134	0.4
		1	1.0129	-0.1
		2	1.0129	-0.1
		3	1.0128	-0.2
B	1.0034	0	1.0134	10.0
		1	1.0032	-0.2
		2	1.0031	-0.1
		3	1.0032	-0.2
C	0.9969	0	0.9979	1.0
		1	0.9964	-0.5
		2	0.9963	-0.6
		3	0.9963	-0.6

* From full core fine-mesh calculations with 6 meshes per material region

** $1mk=10^{-3}$

Figure 4-13. Reconstructed Fast Flux in Core A

Figure 4-14. Reconstructed Thermal Flux in Core A
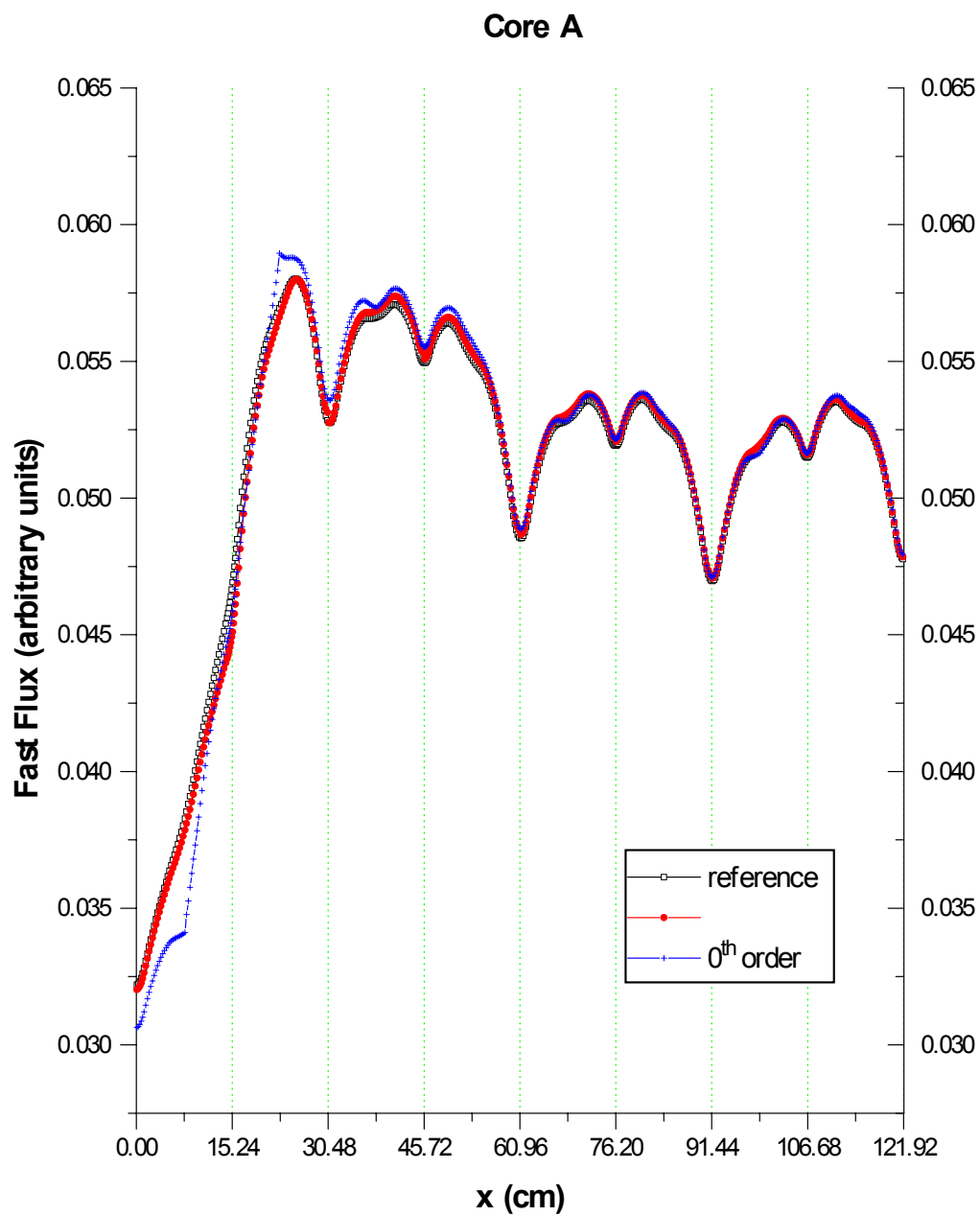
Core B

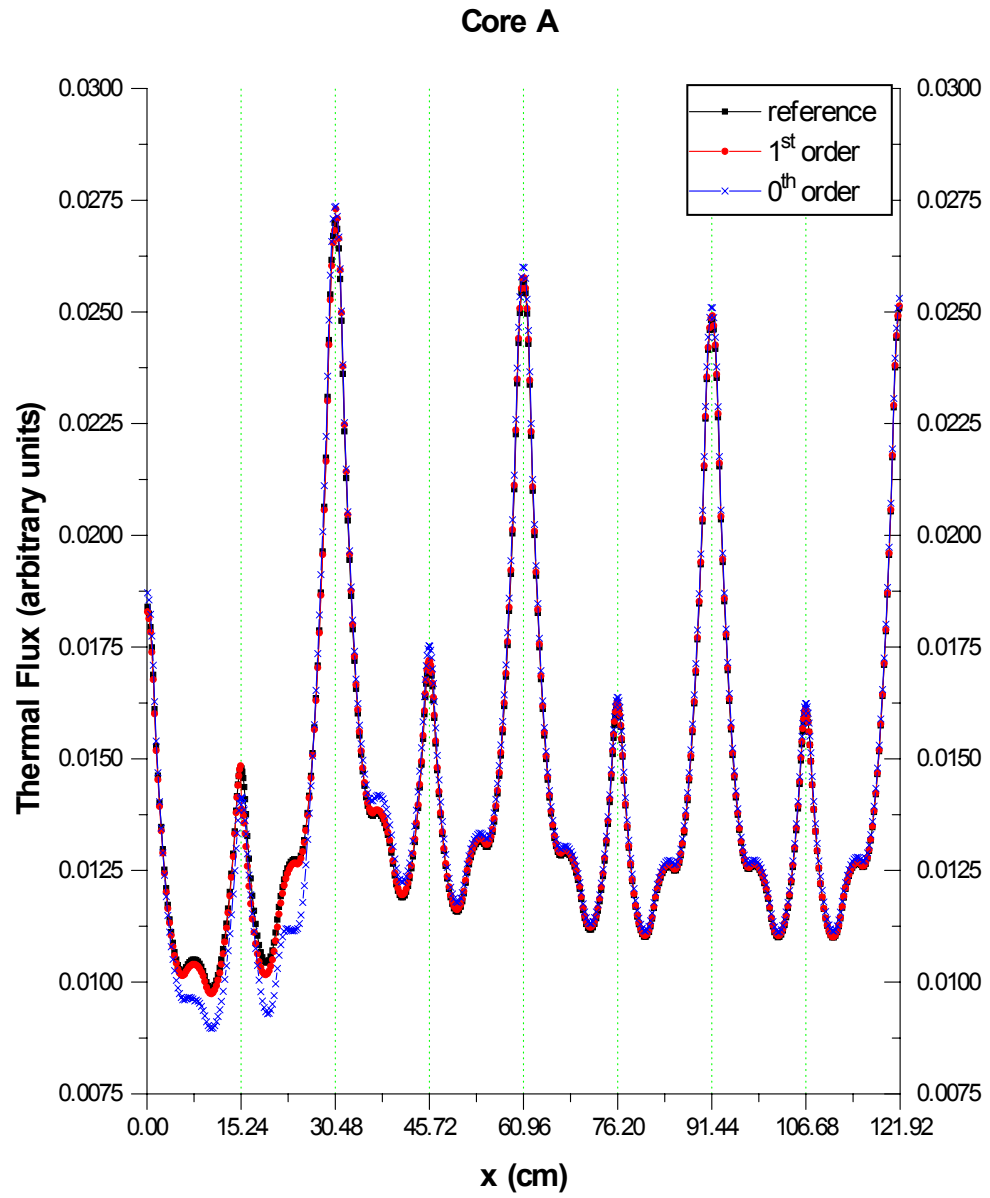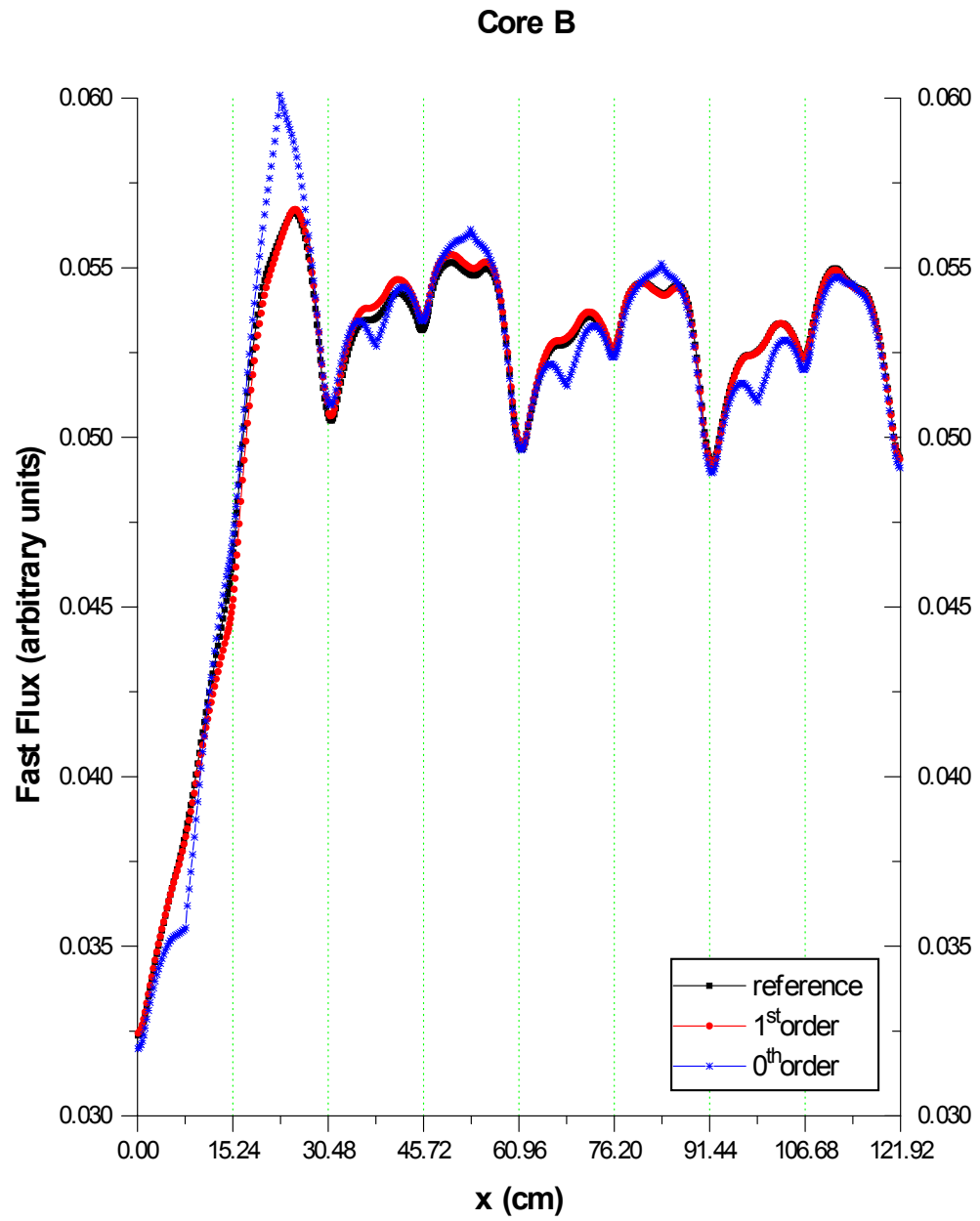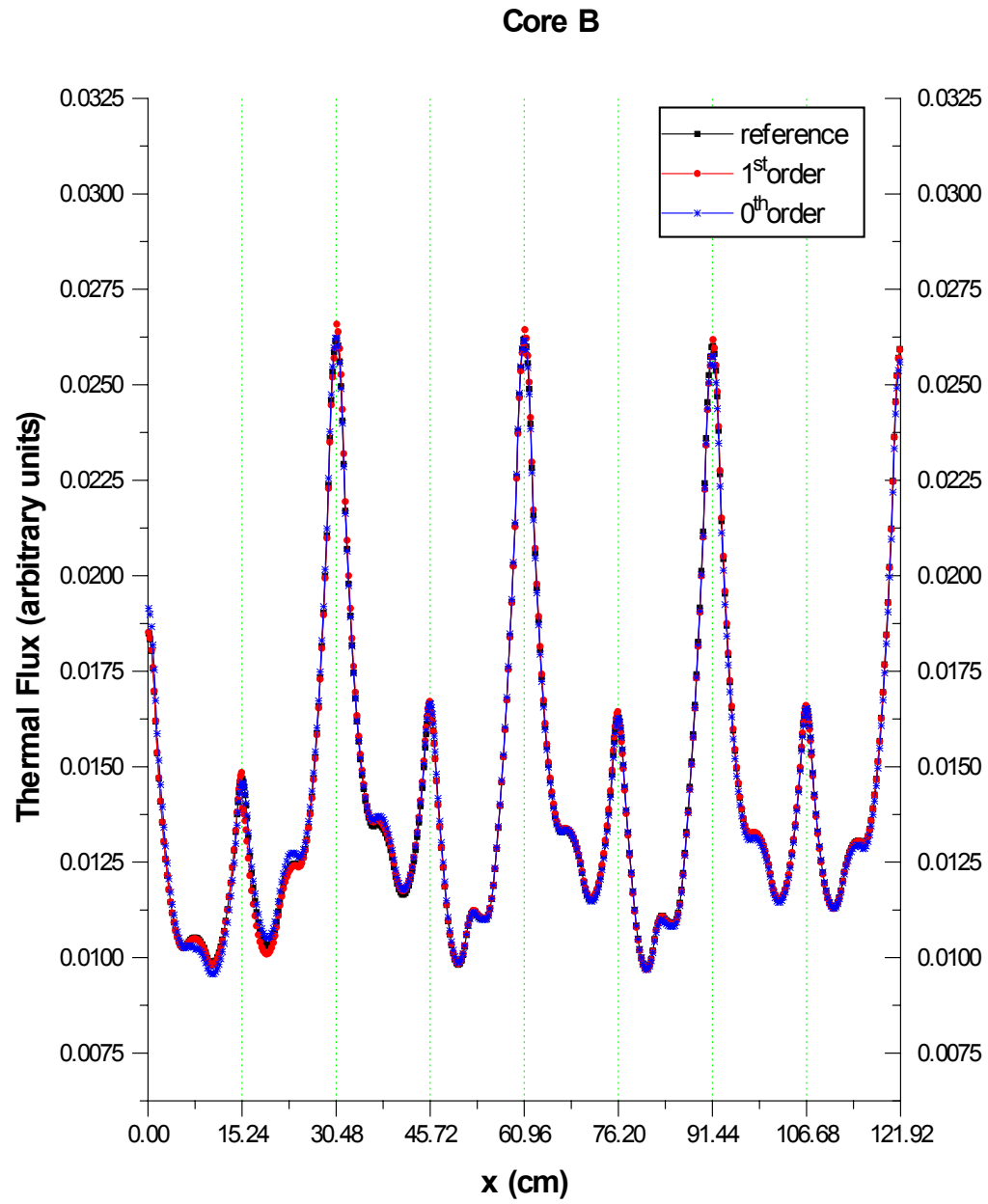**Figure 4-15. Reconstructed Fast Flux in Core B**
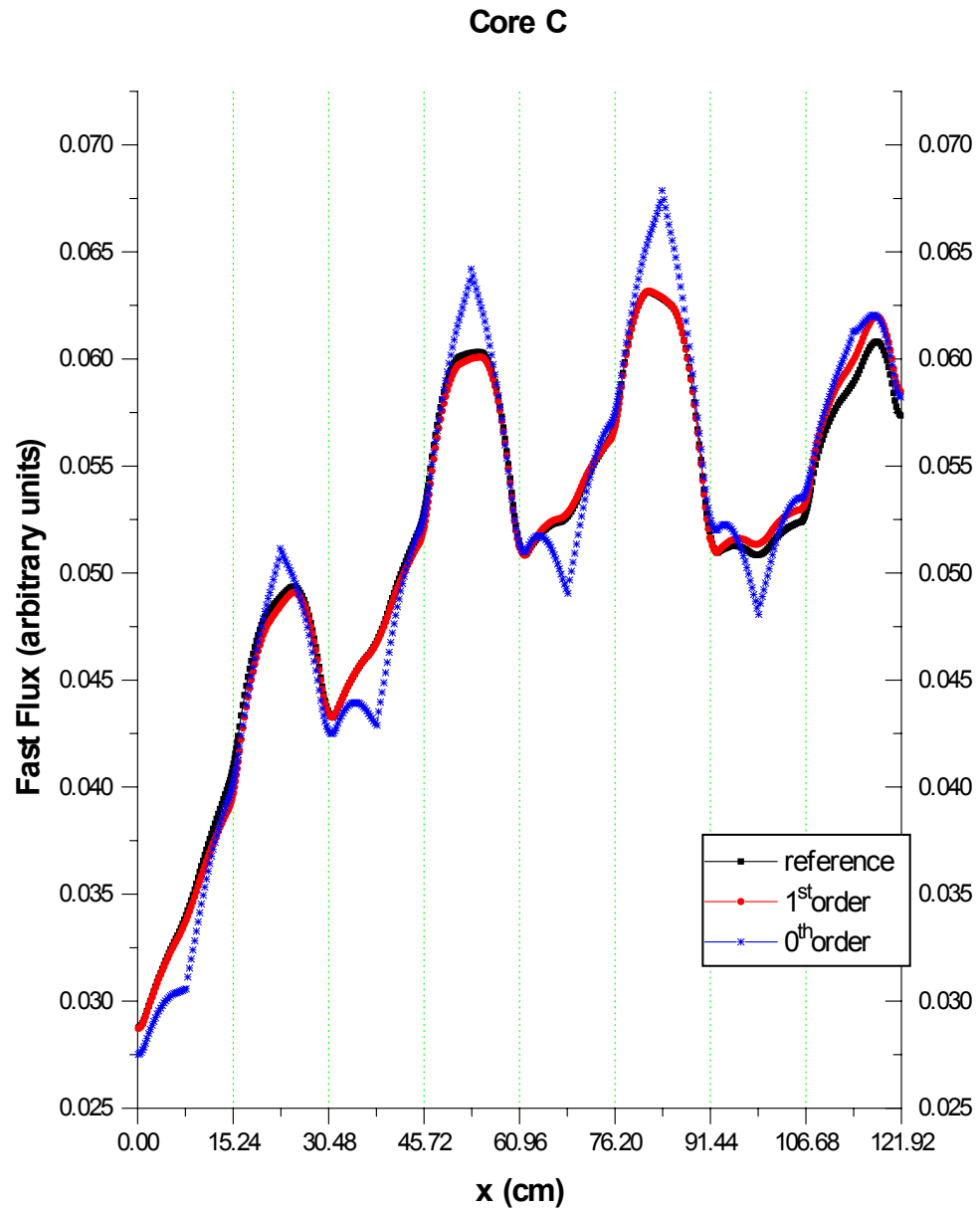
Figure 4-16. Reconstructed Thermal Flux in Core B

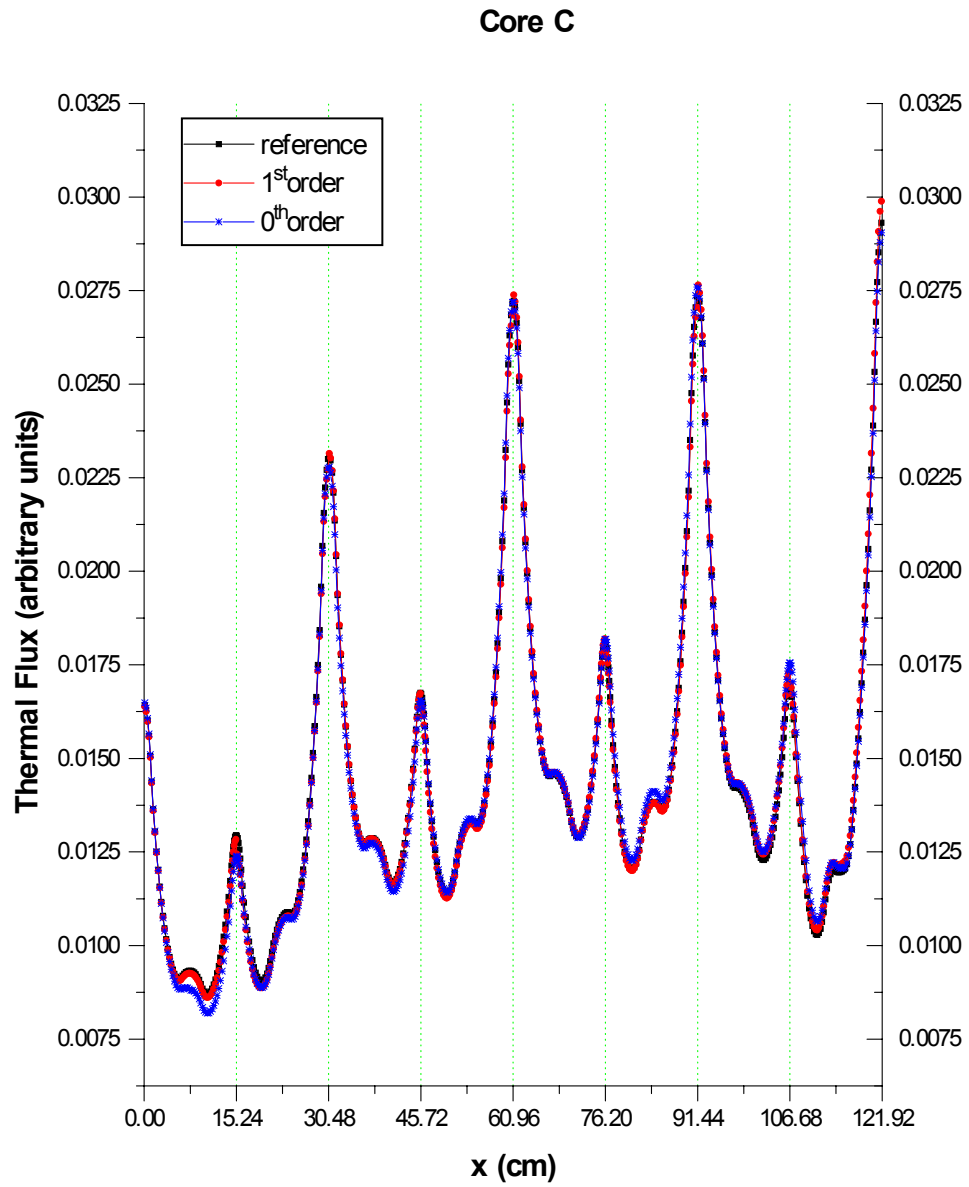**Figure 4-17. Reconstructed Fast Flux in Core C**

Figure 4-18. Reconstructed Thermal Flux in Core C

Table 4-10. Assembly Fast Flux in Core A

Order of Perturbation	Assembly Position	Reference	Nodal	Error[a]	Reconstructed	Error
0	1	0.5903	0.5774	-2.19	0.5586	-5.37
	2	0.8361	0.8579	2.61	0.8393	0.39
	3	0.8516	0.8555	0.46	0.8617	1.19
	4	0.8258	0.8267	0.11	0.8335	0.93
	5	0.7950	0.7924	-0.34	0.7983	0.42
	6	0.7892	0.7863	-0.36	0.7926	0.43
	7	0.7792	0.7743	-0.63	0.7803	0.14
	8	0.7920	0.7892	-0.35	0.7954	0.42
1	1	0.5903	0.5818	-1.44	0.5814	-1.50
	2	0.8361	0.8283	-0.93	0.8290	-0.85
	3	0.8516	0.8552	0.42	0.8550	0.40
	4	0.8258	0.8293	0.41	0.8293	0.42
	5	0.7950	0.7984	0.42	0.7983	0.41
	6	0.7892	0.7916	0.30	0.7916	0.31
	7	0.7792	0.7812	0.25	0.7811	0.24
	8	0.7920	0.7934	0.17	0.7934	0.18
2	1	0.5903	0.5907	0.07	0.5902	-0.02
	2	0.8361	0.8305	-0.67	0.8311	-0.60
	3	0.8516	0.8496	-0.23	0.8494	-0.26
	4	0.8258	0.8256	-0.03	0.8257	-0.02
	5	0.7950	0.7965	0.18	0.7965	0.18
	6	0.7892	0.7909	0.22	0.7910	0.22
	7	0.7792	0.7814	0.28	0.7813	0.27
	8	0.7920	0.7940	0.24	0.7940	0.25
3	1	0.5903	0.5892	-0.18	0.5888	-0.26
	2	0.8361	0.8326	-0.42	0.8331	-0.36
	3	0.8516	0.8513	-0.04	0.8511	-0.06
	4	0.8258	0.8262	0.05	0.8263	0.05
	5	0.7950	0.7963	0.16	0.7963	0.15
	6	0.7892	0.7902	0.13	0.7903	0.14
	7	0.7792	0.7804	0.16	0.7804	0.15
	8	0.7920	0.7929	0.11	0.7929	0.11

[a]Defined as 100*(calculated-reference)/reference

Table 4-11. Assembly Thermal Flux in Core A

Order of Perturbation	Assembly Position	Reference	Nodal	Error[a]	Reconstructed	Error
0	1	0.1809	0.1809	-0.04	0.1719	-5.00
	2	0.2186	0.2201	0.68	0.2087	-4.52
	3	0.2370	0.2385	0.61	0.2419	2.09
	4	0.2274	0.2282	0.34	0.2313	1.71
	5	0.2227	0.2216	-0.47	0.2253	1.20
	6	0.2177	0.2169	-0.36	0.2202	1.13
	7	0.2178	0.2166	-0.56	0.2200	0.98
	8	0.2186	0.2176	-0.46	0.2210	1.09
1	1	0.1809	0.1791	-0.99	0.1795	-0.77
	2	0.2186	0.2159	-1.22	0.2152	-1.53
	3	0.2370	0.2381	0.48	0.2383	0.56
	4	0.2274	0.2284	0.44	0.2284	0.42
	5	0.2227	0.2236	0.43	0.2237	0.45
	6	0.2177	0.2183	0.28	0.2183	0.25
	7	0.2178	0.2184	0.29	0.2185	0.32
	8	0.2186	0.2189	0.16	0.2189	0.14
2	1	0.1809	0.1817	0.45	0.1822	0.71
	2	0.2186	0.2163	-1.04	0.2157	-1.30
	3	0.2370	0.2366	-0.17	0.2368	-0.09
	4	0.2274	0.2274	0.01	0.2274	-0.01
	5	0.2227	0.2231	0.19	0.2231	0.21
	6	0.2177	0.2181	0.19	0.2181	0.17
	7	0.2178	0.2185	0.31	0.2185	0.34
	8	0.2186	0.2191	0.23	0.2191	0.22
3	1	0.1809	0.1813	0.21	0.1818	0.47
	2	0.2186	0.2168	-0.82	0.2162	-1.08
	3	0.2370	0.2371	0.04	0.2373	0.12
	4	0.2274	0.2276	0.08	0.2275	0.06
	5	0.2227	0.2231	0.18	0.2231	0.20
	6	0.2177	0.2180	0.11	0.2179	0.08
	7	0.2178	0.2182	0.19	0.2183	0.22
	8	0.2186	0.2188	0.10	0.2188	0.08

[a]Defined as 100*(calculated-reference)/reference

Table 4-12. Assembly Fast Flux in Core B

Order of Perturbation	Assembly Position	Reference	Nodal	Error[a]	Reconstructed	Error
0	1	0.5909	0.5791	-2.01	0.5800	-1.85
	2	0.8189	0.8414	2.75	0.8414	2.75
	3	0.8099	0.8118	0.24	0.8113	0.18
	4	0.8255	0.8317	0.75	0.8319	0.78
	5	0.7987	0.7934	-0.67	0.7929	-0.72
	6	0.8173	0.8172	-0.01	0.8175	0.02
	7	0.7947	0.7855	-1.15	0.7851	-1.20
	8	0.8151	0.8114	-0.45	0.8113	-0.46
1	1	0.5909	0.5870	-0.67	0.5814	-1.50
	2	0.8189	0.8143	-0.57	0.8290	-0.85
	3	0.8099	0.8153	0.67	0.8550	0.40
	4	0.8255	0.8283	0.34	0.8293	0.42
	5	0.7987	0.8007	0.26	0.7983	0.41
	6	0.8173	0.8165	-0.10	0.7916	0.31
	7	0.7947	0.7944	-0.03	0.7811	0.24
	8	0.8151	0.8144	-0.09	0.7934	0.18
2	1	0.5909	0.5949	0.68	0.5945	0.60
	2	0.8189	0.8178	-0.13	0.8185	-0.06
	3	0.8099	0.8110	0.14	0.8106	0.09
	4	0.8255	0.8252	-0.04	0.8254	-0.01
	5	0.7987	0.7988	0.02	0.7985	-0.02
	6	0.8173	0.8154	-0.23	0.8157	-0.20
	7	0.7947	0.7940	-0.09	0.7937	-0.12
	8	0.8151	0.8136	-0.19	0.8136	-0.18
3	1	0.5909	0.5934	0.43	0.5930	0.35
	2	0.8189	0.8193	0.05	0.8199	0.12
	3	0.8099	0.8124	0.31	0.8120	0.26
	4	0.8255	0.8258	0.03	0.8261	0.07
	5	0.7987	0.7988	0.02	0.7985	-0.02
	6	0.8173	0.8150	-0.28	0.8153	-0.25
	7	0.7947	0.7933	-0.17	0.7931	-0.20
	8	0.8151	0.8127	-0.29	0.8128	-0.28

[a]Defined as 100*(calculated-reference)/reference

Table 4-13. Assembly Thermal Flux in Core B

Order of Perturbation	Assembly Position	Reference	Nodal	Error[a]	Reconstructed	Error
0	1	0.1811	0.1812	0.06	0.1807	-0.24
	2	0.2138	0.2159	0.97	0.2167	1.37
	3	0.2311	0.2327	0.66	0.2327	0.67
	4	0.2112	0.2124	0.61	0.2119	0.37
	5	0.2290	0.2279	-0.49	0.2282	-0.32
	6	0.2092	0.2087	-0.23	0.2082	-0.44
	7	0.2284	0.2260	-1.03	0.2263	-0.94
	8	0.2254	0.2238	-0.72	0.2238	-0.71
1	1	0.1811	0.1806	-0.24	0.1810	-0.03
	2	0.2138	0.2119	-0.91	0.2112	-1.23
	3	0.2311	0.2330	0.82	0.2334	0.98
	4	0.2112	0.2115	0.15	0.2112	0.02
	5	0.2290	0.2299	0.42	0.2302	0.53
	6	0.2092	0.2085	-0.33	0.2082	-0.47
	7	0.2284	0.2287	0.14	0.2289	0.24
	8	0.2254	0.2251	-0.12	0.2250	-0.16
2	1	0.1811	0.1830	1.04	0.1834	1.29
	2	0.2138	0.2126	-0.56	0.2120	-0.84
	3	0.2311	0.2319	0.31	0.2322	0.47
	4	0.2112	0.2107	-0.21	0.2105	-0.33
	5	0.2290	0.2294	0.19	0.2297	0.32
	6	0.2092	0.2082	-0.44	0.2080	-0.57
	7	0.2284	0.2286	0.09	0.2288	0.20
	8	0.2254	0.2249	-0.22	0.2248	-0.26
3	1	0.1811	0.1825	0.79	0.1830	1.04
	2	0.2138	0.2130	-0.39	0.2123	-0.67
	3	0.2311	0.2323	0.49	0.2326	0.65
	4	0.2112	0.2109	-0.14	0.2106	-0.26
	5	0.2290	0.2294	0.20	0.2297	0.32
	6	0.2092	0.2081	-0.50	0.2078	-0.63
	7	0.2284	0.2284	0.01	0.2287	0.11
	8	0.2254	0.2247	-0.31	0.2246	-0.35

[a]Defined as 100*(calculated-reference)/reference

Table 4-14. Assembly Fast Flux in Core C

Order of Perturbation	Assembly Position	Reference	Nodal	Error[a]	Reconstructed	Error
0	1	0.5235	0.5181	-5.01	0.4980	-4.88
	2	0.7150	0.7068	-0.22	0.7135	-0.22
	3	0.7219	0.7196	-2.97	0.7005	-2.97
	4	0.8821	0.8763	1.45	0.8953	1.50
	5	0.8119	0.8135	-1.24	0.8011	-1.32
	6	0.9195	0.9182	2.85	0.9464	2.94
	7	0.7841	0.7910	0.22	0.7846	0.06
	8	0.8862	0.9010	2.30	0.9066	2.30
1	1	0.5235	0.5181	-1.04	0.5179	-1.08
	2	0.7150	0.7068	-1.14	0.7073	-1.09
	3	0.7219	0.7196	-0.32	0.7193	-0.36
	4	0.8821	0.8763	-0.66	0.8766	-0.62
	5	0.8119	0.8135	0.20	0.8131	0.15
	6	0.9195	0.9182	-0.14	0.9186	-0.10
	7	0.7841	0.7910	0.87	0.7906	0.82
	8	0.8862	0.9010	1.66	0.9011	1.68
2	1	0.5235	0.5235	-0.01	0.5231	-0.08
	2	0.7150	0.7099	-0.72	0.7105	-0.63
	3	0.7219	0.7198	-0.30	0.7190	-0.40
	4	0.8821	0.8764	-0.64	0.8772	-0.55
	5	0.8119	0.8120	0.02	0.8112	-0.08
	6	0.9195	0.9182	-0.14	0.9190	-0.05
	7	0.7841	0.7905	0.82	0.7898	0.72
	8	0.8862	0.8936	0.83	0.8939	0.87
3	1	0.5235	0.5216	-0.36	0.5212	-0.44
	2	0.7150	0.7101	-0.70	0.7107	-0.61
	3	0.7219	0.7203	-0.23	0.7195	-0.33
	4	0.8821	0.8778	-0.49	0.8785	-0.40
	5	0.8119	0.8129	0.12	0.8121	0.02
	6	0.9195	0.9188	-0.07	0.9196	0.01
	7	0.7841	0.7899	0.74	0.7891	0.64
	8	0.8862	0.8926	0.72	0.8930	0.76

[a]Defined as 100*(calculated-reference)/reference

Table 4-15. Assembly Thermal Flux in Core C

Order of Perturbation	Assembly Position	Reference	Nodal	Error[a]	Reconstructed	Error
0	1	0.1604	0.1555	-3.09	0.1550	-3.36
	2	0.1873	0.1835	-2.05	0.1846	-1.45
	3	0.2200	0.2172	-1.25	0.2164	-1.62
	4	0.2296	0.2303	0.31	0.2306	0.42
	5	0.2491	0.2486	-0.20	0.2486	-0.21
	6	0.2382	0.2434	2.19	0.2427	1.89
	7	0.2426	0.2442	0.65	0.2449	0.92
	8	0.2285	0.2313	1.21	0.2312	1.19
1	1	0.1604	0.1591	-0.82	0.1593	-0.70
	2	0.1873	0.1850	-1.26	0.1846	-1.48
	3	0.2200	0.2195	-0.20	0.2198	-0.07
	4	0.2296	0.2278	-0.78	0.2274	-0.94
	5	0.2491	0.2498	0.26	0.2501	0.41
	6	0.2382	0.2374	-0.34	0.2370	-0.51
	7	0.2426	0.2449	0.92	0.2452	1.07
	8	0.2285	0.2322	1.62	0.2321	1.56
2	1	0.1604	0.1609	0.31	0.1613	0.55
	2	0.1873	0.1852	-1.16	0.1845	-1.50
	3	0.2200	0.2201	0.07	0.2209	0.40
	4	0.2296	0.2273	-1.02	0.2265	-1.35
	5	0.2491	0.2501	0.38	0.2509	0.70
	6	0.2382	0.2369	-0.53	0.2361	-0.86
	7	0.2426	0.2456	1.22	0.2464	1.54
	8	0.2285	0.2301	0.68	0.2297	0.53
3	1	0.1604	0.1603	-0.05	0.1607	0.19
	2	0.1873	0.1852	-1.15	0.1846	-1.48
	3	0.2200	0.2203	0.15	0.2210	0.47
	4	0.2296	0.2276	-0.88	0.2269	-1.20
	5	0.2491	0.2504	0.49	0.2512	0.81
	6	0.2382	0.2370	-0.47	0.2363	-0.80
	7	0.2426	0.2454	1.16	0.2462	1.47
	8	0.2285	0.2298	0.58	0.2295	0.43

[a]Defined as 100*(calculated-reference)/reference

Chapter V

CONCLUSION

The high-order homogenization method [5] for improving the accuracy of nodal diffusion calculations for a reactive system is implemented into a two-group model. The method is based on the high-order boundary condition perturbation theory, and expands the homogenized cross sections in terms of the current-to-flux ratio at the node interface. This expansion makes possible the correction of the homogenized cross sections for the effect of the core environment in the nodal calculation. The cross section updating process is performed within the nodal calculation by using precomputed data for each unique assembly type, together with the current-to-flux ratio at the node interface. That is, the assembly cross section calculation is decoupled from the nodal calculation. The reconstructed fine-mesh flux is a natural byproduct of the new homogenization method.

It is shown that the expansion series for the flux, eigenvalue and homogenized cross section converge in the multigroup case. Two types of assembly typical of BWR configurations in slab geometry are used to test the convergence in a two-group approach. The high-order corrected values for the flux, eigenvalue, and homogenized cross sections are compared to the reference values obtained from fine-mesh diffusion calculations at the assembly level. It is observed that the number of terms in the expansion series that needs to be considered to obtain a very good agreement with the reference solution depends on the magnitude of the perturbation. For small perturbations in the boundary condition, which is the case when the assembly is placed in a relatively uniform core, a second order correction seems sufficient to compensate for the error. If the assembly is considered as part of a core with large gradients of the flux over the core, more than three terms must be retained in the expansion to obtain an accurate result. In all analyzed cases, the perturbation method achieves an excellent accuracy: the flux RMS error is less than 0.5% in both groups, and the reference homogenized cross sections are almost reproduced. The agreement is also excellent in the case of the discontinuity factors,

which are within 0.15% of the reference values, even for large perturbations (e.g., ~30% difference between the unperturbed and the reference values).

A two-group nodal diffusion code with a bilinear intra-nodal flux shape is developed for the implementation of the high-order homogenization method to two-group in the context of the generalized equivalence theory (GET). The updating of the nodal parameters by using the perturbation method does not require repeated fine-mesh calculations at the assembly level. Only one infinite-medium single-assembly calculation is performed for each unique assembly type, in order to precompute the required quantities (the forward flux, the adjoint flux, and a Green's function) used in estimating the high-order corrections.

The homogenization method is tested by using as a benchmark four different types of cores typical of a BWR in slab geometry. Three of these benchmark problems, are newly developed for this purpose. The nodal calculation is compared to the fine-mesh reference result by means of the node (assembly) integrated flux. The agreement is very good. For all of the analyzed configurations the node-integrated flux is within 1.16% of the assembly-integrated reference flux in all nodes for each group. There is a significant improvement from the zeroth order case (standard GET), in which the node-averaged flux has a large error (e.g., up to 8% in group 1 and up to 14% in group 2 for configuration 2).

It is also shown that the reconstructed fine-mesh flux (or equivalently the power distribution) in the core approximates the reference value very well. The reference flux distribution is almost reproduced by the third order. In contrast, the zeroth order reconstructed flux distribution does not approximate the reference result well. An advantage of the new homogenization method is that not only it provides an excellent estimate of the global power distribution throughout the core, but it also produces the detailed (fine-mesh) distribution of the flux (power) inside each assembly with no almost additional computation effort. Therefore, parameters of importance in reactor operation such as the thermal limits (e.g., the local peaking factor) are predicted very accurately by the new method. Another advantage is that the method produces excellent results even for a simple approximation of the intranodal flux shape such as the bilinear shape used in the present work.

5.1 Future Work

The next step will be to implement the high-order homogenization method into a two-dimensional, and then three-dimensional nodal diffusion model. Also it would be interesting to consider different types of core configurations such as PWR or PBR, or even highly heterogeneous, unrealistic configurations, to assess the method's limitations.

Phase III Work

A main difficulty in going form one to two-group in 1-D was the numerical computation of Green's function which arise because of the energy group coupling. The equations for calculating this function will be similar in the 2-D case; the only difference that might cause impediments might be the treatment of the leakage term when discretizing these equations. Some difficulty might also arise in determining a surface-dependent boundary condition (current-to-flux ratio) from node-averaged quantities. Note that Green's function is not constant at the node interface. As a first approximation, the expansion parameter in the 2-D case could be taken as an average over the node surface, which is consistent with the GET assumption.

A two-group two-dimensional diffusion code needs to be developed to perform all the required precomputations for each assembly type: the solutions of the forward and adjoint flux, and the Green's function. Also, a two-group two-dimensional nodal diffusion code needs to be developed to perform the nodal calculations.

Heterogeneity in the radial direction is of the main concern as far as the homogenization is concerned in LWR configurations. Thus, the 2-D development should take care of most of the homogenization errors. The extension of the method to 3-D would then involve developing the coarse-mesh (nodal) code in 3-D and using the 2-D Green's functions to adjust (correct) the homogenized cross sections for radial neutron leakage (environment) across each fuel assembly surface.

Discretization of the Equations for Green's Function

Let's consider Eqs. (2-14) for the four components of the Green's function $\Psi_{gh}(\vec{x},\vec{x}_0)$. The discretization in slab geometry of the first of these equations is shown here, the procedure is similar for the other three.

$$
\left[-\nabla D_1(\vec{x})\nabla + \sigma_{r1}(\vec{x}) - \lambda_0 v\sigma_{f1}(\vec{x})\chi_1(\vec{x})\right]\Psi_{11}(\vec{x},\vec{x}_0) -
$$
$$
\left[\sigma_{s12}(\vec{x}) + \lambda_0 v\sigma_{f1}(\vec{x})\chi_2(\vec{x})\right]\Psi_{21}(\vec{x},\vec{x}_0) = \delta(\vec{x}-\vec{x}_0) - \overline{\varphi}_{0,1}(\vec{x}_0)
\tag{A-1}
$$

Let the domain (in the x direction) where the equation should be solved be divided into N meshes, such that each mesh has constant material properties over the mesh. Equation (A-1) is integrated over a mesh i (see figure below), from $x_{i-1/2}$ to $x_{i+1/2}$. The functions $\Psi_{11}(\vec{x},\vec{x}_0)$ and $\Psi_{21}(\vec{x},\vec{x}_0)$ are considered constant over the mesh:

$$
\Psi_{11}(\vec{x},\vec{x}_0) \equiv \Psi_{11}(i,j)
$$
$$
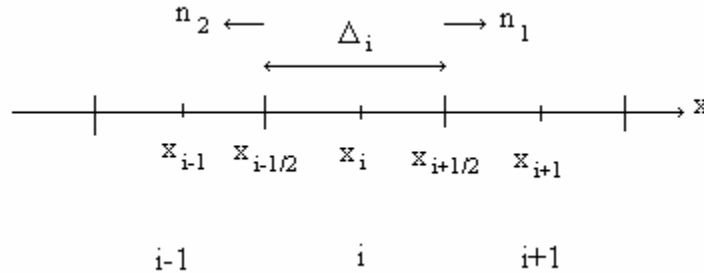\Psi_{21}(\vec{x},\vec{x}_0) \equiv \Psi_{21}(i,j)
\tag{A-2}
$$

Figure A-1. Space Discretization

Let's consider the integration of the "leakage" term first:

$$L = -\int_{x_{i-1/2}}^{x_{i+1/2}} \nabla D_1 \cdot \nabla \Psi_{11} dV = -\sum_{k=1}^{2} \int_{S_k} D_1 \nabla \Psi \cdot_{11} \vec{n}_S dS = -D_i \frac{\varphi_i^+ - \varphi_i}{\Delta_i / 2} + D_i \frac{\varphi_i - \varphi_i^-}{\Delta_i / 2} \quad \text{(A-3)}$$

with $\varphi_i^+ \equiv \Psi_{11}(x_{i+1/2})$, $\varphi_i^- \equiv \Psi_{11}(x_{i-1/2})$, $\varphi_i \equiv \Psi_{11}(x_i)$, and $x_i = x_{i-1/2} + \Delta_i / 2$. The function $\Psi_{11}(\vec{x}, \vec{x}_0)$ has been renamed and the x_0 dependence has been dropped for convenience. The following boundary conditions are considered at the interface of mesh i with the adjacent mesh i-1 and i+1, respectively:

$$x = x_{i-1/2} \qquad \varphi_{i-1}^+ = \varphi_i^-$$

$$-D_1^{i-1} \frac{\varphi_{i-1}^+ - \varphi_{i-1}}{\Delta_{i-1} / 2} = -D_1^i \frac{\varphi_i - \varphi_i^-}{\Delta_i / 2} \quad \text{(A-4)}$$

$$x = x_{i+1/2} \qquad \varphi_{i+1}^- = \varphi_i^+$$

$$-D_1^i \frac{\varphi_i^+ - \varphi_i}{\Delta_i / 2} = -D_1^{i+1} \frac{\varphi_{i+1} - \varphi_{i+1}^-}{\Delta_{i+1} / 2} \quad \text{(A-5)}$$

By solving for φ_i^+ and φ_i^- in (A-3) and (A-4) one gets:

$$\varphi_i^- = \frac{d_{i-1}\varphi_{i-1} + d_i\varphi_i}{d_{i-1} + d_i}$$

$$\varphi_i^+ = \frac{d_i\varphi_i + d_{i+1}\varphi_{i+1}}{d_i + d_{i+1}} \quad \text{(A-6)}$$

If expressions (A-6) for the surface fluxes are used in (A-3) it is obtained:

$$L = -d_{i-1,i}\varphi_{i-1} + (d_{i-1,i} + d_{i,i+1})\varphi_i - d_{i,i+1}\varphi_{i+1} \quad \text{(A-7)}$$

86

where $d_{i,i+1} \equiv 2d_i d_{i+1} / (d_i + d_{i+1})$. The use of (A-7) when integrating (A-1) over the mesh i leads to:

$$-d_{i-1,i}\Psi_{11}(i-1,j) + \left[d_{i-1,i} + d_{i,i+1} + \left(\sigma_{r1}^i - \lambda_0 \nu \sigma_{f1}^i \chi_1^i\right)\Delta_i\right]\Psi_{11}(i,j) - d_{i,i+1}\Psi_{11}(i+1,j) = \\ \left(\sigma_{s12}^i + \lambda_0 \nu \sigma_{f1}^i \chi_2^i\right)\Delta_i \Psi_{21}(i,j) + \delta_{ij} - \overline{\varphi}_{0,1}(j) \tag{A-8}$$

The coupling coefficients $d_{i,i+1}$ and $d_{i-1,i}$ have a particular form for the boundary meshes, depending on the boundary condition. For example, if the boundary condition for the right boundary (i=N) is:

$$aJ(x_{i+1/2}) + b\varphi_i^+ = 0 \tag{A-9}$$

then

$$\varphi_i^+ = -\frac{a}{b}J(x_{i+1/2}) \tag{A-10}$$

Using this expression for φ_i^+ to calculate the current at the boundary as expressed in (A-3), one gets:

$$J(x_{i+1/2}) = -D_i \frac{\varphi_i^+ - \varphi_i}{\Delta_i/2} = -2d_i\left(\varphi_i^+ - \varphi_i\right) = 2d_i \frac{a}{b}J(x_{i+1/2}) + 2d_i\varphi_i \tag{A-11}$$

$$J(x_{i+1/2}) = \frac{2d_i}{1 - 2\frac{a}{b}d_i}\varphi_i \tag{A-12}$$

The leakage term (A-3) becomes:

$$L_{right} = J(x_{i+1/2}) - J(x_{i-1/2}) = \frac{2d_i}{1 - 2\frac{a}{b}d_i}\varphi_i + d_{i-1,i}(\varphi_i - \varphi_{i-1}) =$$

$$-d_{i-1,i}\varphi_{i-1} + \left(\frac{2d_i}{1 - 2\frac{a}{b}d_i} + d_{i-1,i}\right)\varphi_i$$

(A-13)

In this case then (i=N) we have in the leakage term $d_{i,i+1} = 0$ and the coefficient of φ_i in

the leakage term is $\dfrac{2d_i}{1 - 2\dfrac{a}{b}d_i} + d_{i-1,i}$, versus $d_{i-1,i} + d_{i,i+1}$ for an inner mesh.

Appendix B

Nodal Equations

The two-group diffusion equations to be discretized in slab geometry are shown below:

$$\left[-\nabla D_g(x) \cdot \nabla + \sigma_{rg}(x)\right]\varphi_g(x) = \sigma_{g'g}(x)\varphi_{g'}(x) + \lambda\chi_g(x)\left[\nu\sigma_{fg}(x)\varphi_g(x) + \nu\sigma_{fg'}(x)\varphi_{g'}(x)\right]$$

$$g, g' = 1,2 \qquad g \neq g' \qquad \text{(B-1)}$$

where φ is the scalar flux, λ is the eigenvalue, D is the diffusion coefficient, σ_r is the removal cross section, χ is the neutron spectrum, $\sigma_{g'g}$ is the scattering cross section from group g' to group g, and $\nu\sigma_f$ is the product of the number of neutrons per fission and the fission cross section, with g as a group index.

The spatial variable x is discretized according to Figure B-1. Equation (B-1) is integrated over the mesh i from $x_{i-1/2}$ to $x_{i+1/2}$, with x_i the center point. φ_i^- and f_i^- are the flux and discontinuity factor on the left boundary of mesh i, whereas φ_i^+ and f_i^+ have the same meaning, but correspond to the right boundary. The length of mesh i is Δ_i, and φ_i is the flux at the center point. The mesh is chosen such that the material properties are constant within the region.

By integrating (B-1) over mesh i one obtains:

$$\int_{x_{i-1/2}}^{x_{i+1/2}} -\nabla D_{g,i} \cdot \nabla\varphi_g(x)dx + \sigma_{rg,i}\int_{x_{i-1/2}}^{x_{i+1/2}}\varphi_g(x)dx + \sigma_{g'g,i}\int_{x_{i-1/2}}^{x_{i+1/2}}\varphi_{g'}(x)dx =$$

$$\lambda\chi_{g,i}\left[\nu\sigma_{fg,i}\int_{x_{i-1/2}}^{x_{i+1/2}}\varphi_g(x)dx + \nu\sigma_{fg',i}\int_{x_{i-1/2}}^{x_{i+1/2}}\varphi_{g'}(x)dx\right] \qquad g, g' = 1,2 \qquad g \neq g' \qquad \text{(B-2)}$$
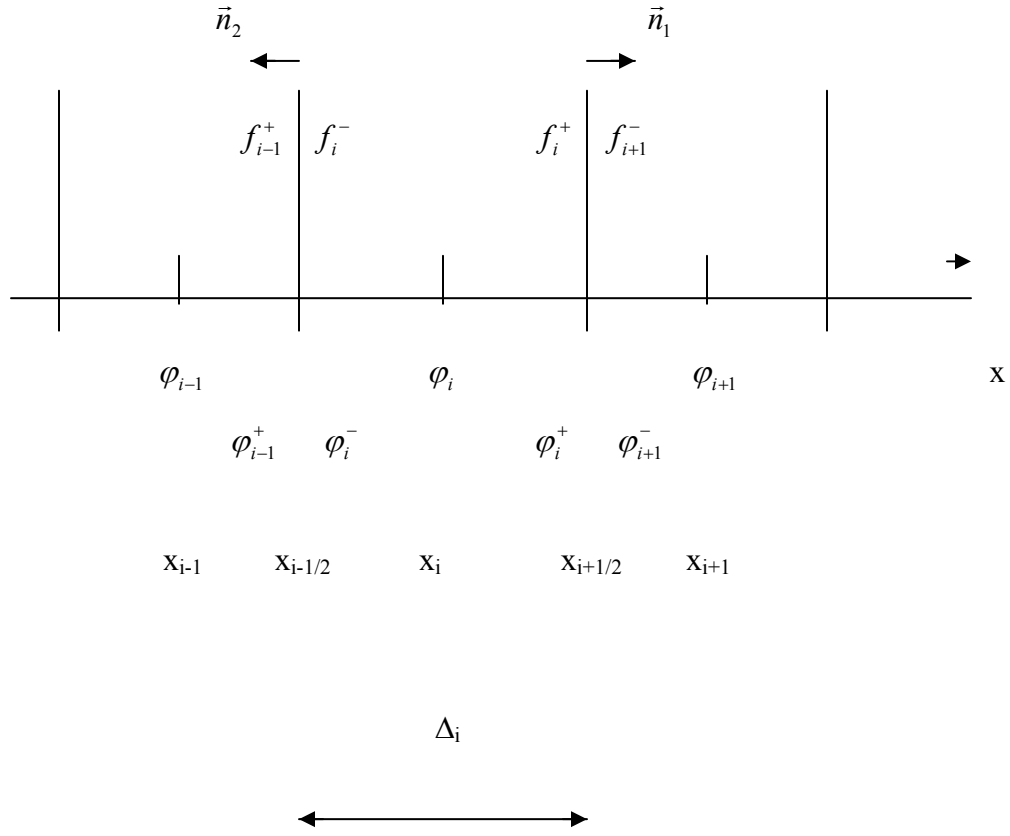
Figure B-1. Discretization of the Spatial Variable

The leakage term in Eq. (B-2) can be written as:

$$L = -\sum_{k=1}^{2} \int_{S_k} D_{g,i} \nabla \varphi_g(x) \cdot \vec{n}_S dS = J_g\left(x_{i+1/2}\right) - J_g\left(x_{i-1/2}\right) = -D_i \frac{\varphi_i^+ - \varphi_i}{\Delta_i/2} + D_i \frac{\varphi_i - \varphi_i^-}{\Delta_i/2} \quad \text{(B-3)}$$

where J stands for current. The boundary condition (current continuity and flux discontinuity) is expressed by (with the group index dropped for convenience):

$$x = x_{i+1/2} \qquad f_i^+ \varphi_i^+ = f_{i+1}^- \varphi_{i+1}^-$$

$$-D_i \frac{\varphi_i^+ - \varphi_i}{\Delta_i/2} = -D_{i+1} \frac{\varphi_{i+1} - \varphi_{i+1}^-}{\Delta_{i+1}/2}$$

(B-4)

$$x = x_{i-1/2} \qquad f_{i-1}^+ \varphi_{i-1}^+ = \varphi_i^- f_i^-$$

(B-5)

$$-D_{i-1} \frac{\varphi_{i-1}^+ - \varphi_{i-1}}{\Delta_{i-1}/2} = -D_i \frac{\varphi_i - \varphi_i^-}{\Delta_i/2}$$

The surface fluxes corresponding to mesh i are determined from Eqs. (B-4) and (B-5) as:

$$\varphi_i^- = \frac{d_{i-1} f_{i-1}^+}{d_{i-1} f_i^- + d_i f_{i-1}^+} \varphi_{i-1} + \frac{d_i f_{i-1}^+}{d_{i-1} f_i^- + d_i f_{i-1}^+} \varphi_i$$

(B-6)

$$\varphi_i^+ = \frac{d_{i+1} f_{i+1}^-}{d_i f_{i+1}^- + d_{i+1} f_i^+} \varphi_{i+1} + \frac{d_i f_{i+1}^-}{d_i f_{i+1}^- + d_{i+1} f_i^+} \varphi_i$$

(B-7)

where $d_i \equiv (D_i / \Delta_i)$. By using Eqs. (B-6) and (B-7) in Eq. (B-3), the leakage term becomes:

$$L = -\frac{2d_i d_{i-1}}{d_i + d_{i-1}(f_i^- / f_{i-1}^+)} \varphi_{i-1} + \left[\frac{2d_i d_{i-1}}{d_i + d_{i-1}(f_i^- / f_{i-1}^+)} \frac{f_i^-}{f_{i-1}^+} + \frac{2d_i d_{i+1}}{d_i + d_{i+1}(f_i^+ / f_{i+1}^-)} \frac{f_i^+}{f_{i+1}^-} \right] \varphi_i$$
$$-\frac{2d_i d_{i+1}}{d_i + d_{i+1}(f_i^+ / f_{i+1}^-)} \varphi_{i+1}$$

(B-8)

A bilinear shape is considered for the flux within the node:

$$\varphi(x) = \begin{cases} a_1 x + b_1, & x_{i-1/2} \le x \le x_i \\ a_2 x + b_2, & x_i \le x \le x_{i+1/2} \end{cases}$$

(B-9)

with a_1, a_2, b_1 and b_2 constants. The integral of the flux over mesh i in Eq. (B-2) can be written as:

$$\int_{x_{i-1/2}}^{x_{i+1/2}} \varphi(x)dx = \int_{x_{i-1/2}}^{x_i} \varphi(x)dx + \int_{x_i}^{x_{i+1/2}} \varphi(x)dx = a_1(\Delta_i/4)(x_{i-1/2} + x_i) + b_1(\Delta_i/2) +$$
$$+ a_2(\Delta_i/4)(x_i + x_{i+1/2}) + b_2(\Delta_i/2)$$

(B-10)

The coefficients a_1, a_2, b_1 and b_2 are determined from:

$$\varphi(x_{i-1/2}) = \varphi_i^-, \quad \varphi(x_i) = \varphi_i, \quad \varphi(x_{i+1/2}) = \varphi_i^+$$

(B-11)

as:

$$a_1 = \frac{\varphi_i - \varphi_i^-}{\Delta_i/2}, \quad a_2 = \frac{\varphi_i^+ - \varphi_i}{\Delta_i/2}, \quad b_1 = \varphi_i - \frac{\varphi_i - \varphi_i^-}{\Delta_i/2}x_i, \quad b_2 = \varphi_i - \frac{\varphi_i^+ - \varphi_i}{\Delta_i/2}x_i$$

(B-12)

By using Eq. (B-12) in Eq. (B-10) one obtains:

$$\int_{x_{i-1/2}}^{x_{i+1/2}} \varphi(x)dx = \frac{\Delta_i}{4}\left(\frac{\varphi_{i-1}}{4} + \frac{\varphi_i}{2} + \frac{\varphi_{i+1}}{4}\right) = \frac{1}{4}\Delta_i\varphi^{avg}$$

(B-13)

where

$$\varphi^{avg} \equiv \frac{\varphi_{i-1}}{4} + \frac{\varphi_i}{2} + \frac{\varphi_{i+1}}{4}$$

(B-14)

is the average flux in mesh i. Use of (B-8) and (B-13) in (B-2) leads to:

$$a_{i-1,i}^g \varphi_{g,i-1} + a_{i,i}^g \varphi_{g,i} + a_{i,i+1}^g \varphi_{g,i+1} = S_{g,i}, \qquad i = 1,...N$$

(B-15)

92

where N is the total number of meshes and g a group index. The expressions for the coefficients in Eq. (B-15) for the interior meshes are shown below; in the boundary meshes their form depends on the boundary condition imposed.

$$a_{i-1,i}^g = -\frac{2d_{g,i}d_{g,i-1}f_{g,i-1}^+}{d_{g,i}f_{g,i-1}^+ + d_{g,i-1}f_{g,i}^-} + \frac{d_{g,i-1}f_{g,i-1}^+}{d_{g,i}f_{g,i-1}^+ + d_{g,i-1}f_{g,i}^-}\frac{\Delta_i}{4}\sigma_{rg,i}$$

(B-16)

$$a_{i,i+1}^g = -\frac{2d_{g,i}d_{g,i+1}f_{g,i+1}^-}{d_{g,i}f_{g,i+1}^- + d_{g,i+1}f_{g,i}^+} + \frac{d_{g,i+1}f_{g,i+1}^-}{d_{g,i}f_{g,i+1}^- + d_{g,i+1}f_{g,i}^+}\frac{\Delta_i}{4}\sigma_{rg,i}$$

(B-17)

$$a_{i,i}^g = \frac{2d_{g,i}d_{g,i-1}f_{g,i}^-}{d_{g,i}f_{g,i-1}^+ + d_{g,i-1}f_{g,i}^-} + \frac{2d_{g,i}d_{g,i+1}f_{g,i}^+}{d_{g,i}f_{g,i+1}^- + d_{g,i+1}f_{g,i}^+} + \frac{\Delta_i}{2}\sigma_{rg,i} +$$

$$\left(\frac{d_{g,i}f_{g,i-1}^+}{d_{g,i}f_{g,i-1}^+ + d_{g,i-1}f_{g,i}^-} + \frac{d_{g,i}f_{g,i+1}^-}{d_{g,i}f_{g,i+1}^- + d_{g,i+1}f_{g,i}^+}\right)\frac{\Delta_i}{4}\sigma_{rg,i}$$

(B-18)

$$S_{g,i} = \chi_{g,i}\left[v\sigma_{fg,i}\varphi_{g,i}^{avg} + v\sigma_{fg',i}\varphi_{g',i}^{avg}\right] + \sigma_{g'g,i}\varphi_{g',i}^{avg}$$

(B-19)

References

1. Smith, K. S., "*Spatial Homogenization Methods for Light Water Reactor Analysis*", Ph.D. Thesis, M. I. T. (1980)

2. Casal, J.J., Stamm'ler, R.J.J., Villarino, E.A, and Ferri, A.A. "*HELIOS: Geometric Capabilities of a New Fuel-Assembly Program*", Intl Topical Meeting on Advances in Mathematics, Computations, and Reactor Physics, Pittsburgh, Pennsylvania, April 28-May 2, 1991,Vol. 2, p. 10.2.1 1-13 (1991)

3. Kelly, D.J., "*Depletion of a BWR Lattice Using the RACER Continuous Energy Monte Carlo Code*", Proc. Int. Conf. Mathematics and Computations, Reactor Physics, and Environmental Analyses, Portland, Oregon, April 30-May 4, Vol. 2, p. 1011, American Nuclear Society (1995)

4. Golub, H.G., Van Loan, C.F., " *Matrix Computations* ", Third Edition, John Hopkins University Press (1996)

5. Rahnema, F., and Nichita, E.M., "*Leakage Corrected Spatial (Assembly) Homogenization Technique*", Annals of Nuclear Energy, **24**, No.6, 477 (1997)

6. Giust, F.D., "*Release Notes for Helios System 1.6*", commercial Studsvik Scandpower Report, SSP-00/205, January 03 (2000).

7. McKinley, M.S., Rahnema, F., " *Higher-Order Boundary Condition Perturbation Theory for the Diffusion Approximation* ", Nuclear Science and Engineering, **135**, 15 (2000)

8. Rahnema, F., McKinley, M.S., "*High-Order Cross Section Homogenization Method* ", Annals of Nuclear Energy*, **29**, 7, 875 (2002)

9. IMSL Fortran 90 MP Library v3.0, Lahey Computer Systems (1999)